INFORMATION TO USERS

This manuscript has been reproduced from the microfilm master. UMI films the text directly from the original or copy submitted. Thus, some thesis and dissertation copies are in typewriter face, while others may be from any type of computer printer.

The quality of this reproduction is dependent upon the quality of the copy submitted. Broken or indistinct print, colored or poor quality illustrations and photographs, print bleedthrough, substandard margins, and improper alignment can adversely affect reproduction.

In the unlikely event that the author did not send UMI a complete manuscript and there are missing pages, these will be noted. Also, if unauthorized copyright material had to be removed, a note will indicate the deletion.

Oversize materials (e.g., maps, drawings, charts) are reproduced by sectioning the original, beginning at the upper left-hand corner and continuing from left to right in equal sections with small overlaps. Each original is also photographed in one exposure and is included in reduced form at the back of the book.

Photographs included in the original manuscript have been reproduced xerographically in this copy. Higher quality 6" x 9" black and white photographic prints are available for any photographs or illustrations appearing in this copy for an additional charge. Contact UMI directly to order.

UMI

A Bell & Howell Information Company
300 North Zeeb Road, Ann Arbor MI 48106-1346 USA
313/761-4700 800/521-0600

Performance Analyses of Frequency-Hopped Spread-Spectrum Multiple Access Systems in Fading Environments

by

Usa Svasti-Xuto

B.Eng., Kasetsart University, Bangkok, Thailand, 1983
M.Sc., Wright State University, Dayton, Ohio, U.S.A., 1985

A Dissertation Submitted in Partial Fulfillment of the
Requirements for the Degree of

DOCTOR OF PHILOSOPHY

in the Department of Electrical and Computer Engineering

We accept this dissertation as conforming
to the required standard

Dr. Qiang Wang, Supervisor (Department of ECE)

Dr. Vijay K. Bhargava, Departmental Member (Department of ECE)

Dr. Kin F. Li, Departmental Member (Department of ECE)

Dr. Gholamali C. Shoja, Outside Member (Department of Computer Science)

Dr. Hiroyuki Yashima, External Examiner (Department of Information and Computer Sciences, Saitama University)

Supervisor: Dr. Qiang Wang

ABSTRACT

The focus of this dissertation is the performance analyses of two classes of frequency-hopped spread-spectrum multiple access (FH-SSMA) systems in various fading environments.

The capacity of Viterbi's FH-SSMA system is evaluated under three types of fading, namely Rician, shadowed Rician, and Nakagami fading. The results of recent experiments have indicated that these fading phenomena occur in various environments where the FH-SSMA system may be implemented. In this dissertation, the deletion probability for each fading scenario is derived. Subsequently, the system capacity is analyzed in terms of maximum number of users versus average bit error rate. The effect of a change in the signal-to-noise ratio level on the system capacity is also demonstrated. For Rician fading, it is found that the capacity of the system with a Rician factor of 2 dB is reduced by 13 percent as compared to the capacity of the non-fading case. For shadowed Rician fading, three shadowing scenarios are considered: light, average, and heavy. It is shown that the light and the average shadowing scenarios provide only a slight decrease in the capacity, while the heavy shadowing scenario renders a capacity identical to that for the Rayleigh fading case. Finally, for Nakagami fading the capacity is found to decrease by 50 percent as the fading parameter is reduced to 0.5.

The performance of a cellular frequency-hopped spread-spectrum multiple access system is studied under an indoor environment. It is demonstrated how the system capacity, given in terms of the number of users per cell, is affected by the number of cells in the system. Also, the influence of the delay spread, which is the result of multipath propagation, is investigated. The analysis focuses on a worst-case scenario where a user

receives both the desired and interfering signals with equal power levels. This scenario applies to both the downlink and the uplink. It is shown that the system capacity is reduced drastically as the number of adjacent interfering cells increases from one to three. Previous work concerning the indoor multipath propagation assumed that the number of paths is fixed, the path delays are uniformly distributed, and the path gains are equal. In this dissertation, a more realistic channel model derived from actual impulse response measurements by Saleh and Valenzuela is employed. The model consists of clusters of rays with constant cluster and ray arrival rates and power-delay time constants. The system performance is shown to be affected strongly by the change in the power-delay time constants, yet only slightly influenced by the variation in the arrival rates of the rays and clusters. In addition, the degradation in the system performance due to the delay spread becomes more severe as the transmission rate increases.

Examiners:

Dr. Qiang Wang, Supervisor (Department of ECE)

Dr. Vijay K. Bhargava, Departmental Member (Department of ECE)

Dr. Kin F. Li, Departmental Member (Department of ECE)

Dr. Gholamali C. Shoja, Outside Member (Department of Computer Science)

Dr. Hiroyuki Yashima, External Examiner (Department of Information and Computer Sciences, Saitama University)

Contents

List of Tables

List of Figures

Acknowledgments

First of all, I would like to express my sincere gratitude to Dr. Qiang Wang for his supervision, guidance, and encouragement throughout the course of my study. I am very grateful to Dr. Vijay K. Bhargava for his advice, support, and generosity.

I also would like to thank Dr. Kin F. Li and Dr. Gholamali C. Shoja for serving on my supervisory committee, and Dr. Hiroyuki Yashima of the Department of Information and Computer Sciences, Saitama University, for serving as the external examiner.

I am greatly indebted to the Canadian International Development Agency (CIDA) for its financial support throughout my stay in Canada. My deep appreciation is extended to Ms Claire Beaudreault of the S.M. Group Inc./Cogesult Inc. Consortium, for her assistance and encouragement.

I owe many thanks to Ms Karia Kaukinen for proof-reading this dissertation and helping me with my written English. I also appreciate the help and friendship given by the Thai students at the University of Victoria.

I thank my family very much for their support during my doctoral study.

Last and by no means least, I want to thank Miss Piyasiri Sujpluem for her encouragement and understanding.

To my mother, my father,

and

the memory of my grandmother

Chapter 1

Introduction

In wireless mobile and personal communications, the spread-spectrum technique seems to be one of the most promising techniques that can fulfill the service requirements. When this technique is used as a multiple access scheme, it can support more potential users than other conventional systems, such as the frequency division multiple access system [1]-[4]. Since it is inherently a form of digital communication, the spread-spectrum technique is more reliable and flexible than its analog counterpart [5]. Furthermore, it can allow various types of traffic, such as voice, data, video, etc., to be fully integrated into one network.

In general, there are two classes of the spread-spectrum techniques: frequency hopping and direct sequence. The frequency hopping technique was developed more than half a century ago [6], and has been primarily utilized for defense communications, due to its anti-jamming capability and low interception probability. It was not until the late 1970s that researchers began to examine this technique for possible use as a multiple access scheme in mobile radio communications [1], [2]. Since then, the so called *frequency-hopped spread-spectrum multiple access* (FH-SSMA) system has been investigated intensively for several multi-user applications.

In most cases of mobile radio communications, transmission channels are found to be far from ideal due to radio propagation. One of the most important characteristics of radio propagation is multipath fading. Multipath fading can vary widely from channel to channel depending upon the physical features of the environment within which the communication system is implemented. For example, in a factory or an urban microcellular environment, the channel may be corrupted by Rician fading. On the other hand, in a land mobile satellite channel, the multipath fading is represented by a shadowed Rician model. In some cases, the mobile channels can be characterized by the Rayleigh and the Nakagami distributions. Whichever fading characteristic the channel may possess, the performance of the system is affected to a certain degree.

Hence, prior to the implementation of the FH-SSMA system, it is necessary to investigate precisely how the system performance is influenced by each fading characteristic. The knowledge gained from the study then can be used as a design guideline. This dissertation is therefore focused on the performance analysis of the FH-SSMA system under various fading environments.

1.1 Contributions of the Dissertation

The first part of this dissertation will involve the performance analysis of an FH-SSMA system proposed by Viterbi [1]. Previously, this system was studied under the Rayleigh [7] and shadowed Rayleigh [8] fading environments. This dissertation will consider three other fading scenarios, namely Rician, shadowed Rician, and Nakagami fading. The expressions for the deletion probability of a transmitted signal due to both the additive white Gaussian noise (AWGN) and the fading phenomena are derived for each fading case. The performance of the system is illustrated in terms of system capacity and is also

compared with the performance in the presence of Rayleigh fading.

In the second part of this dissertation, special attention is paid to the performance of an FH-SSMA system in an indoor environment. Unlike earlier work [51]-[62], the analysis in this dissertation deals with a cellular network. The effect of the delay spread on the system performance due to the multipath propagation is considered. The channel model developed by Saleh and Valenzuela [33] will be utilized. This model is more realistic than the one employed in the previous work, since it is derived from actual experiments. Although the Saleh-Valenzuela model was thought to be more suitable for simulation, it will be demonstrated that the analysis is indeed tractable. The influence of each channel parameter on the system performance, which is given in terms of system capacity, will be investigated.

1.2 Outline of the Dissertation

In Chapter 2, the principle of the frequency-hopped spread-spectrum technique is provided. Also, the fading models considered in this dissertation will be described. These include the Rayleigh, the Rician, the shadowed Rician, and the Nakagami fading models.

Chapter 3 presents the performance analysis of Viterbi's FH-SSMA system in three fading scenarios mentioned in Section 1.1. It includes an explanation of the system operation, as well as the derivation of the formulas needed for evaluating the bit error probability. The system performance is illustrated in terms of the number of users for various values of channel parameters. Also, the impact of the variation in the signal-to-noise ratio is demonstrated.

Chapter 4 is concerned with the performance analysis of the cellular FH-SSMA system in an indoor environment. First, the channel model, the system operation, and the

signal model are described. Then, the derivation of the expression for the bit error probability is presented. Finally, the numerical results show how the system performance is affected by the multipath delay spread.

Conclusions and suggestions for future research are given in Chapter 5.

Chapter 2

Fundamental Principles

In this chapter, the principle of the frequency-hopped spread-spectrum (FH-SS) technique is presented. The mathematical representation of the Rayleigh, the Rician, the shadowed Rician, and the Nakagami fading scenarios is also described.

2.1 Frequency-Hopped Spread-Spectrum Technique

In general, the FH-SS technique can be categorized into two distinct classes: the conventional and the Viterbi technique. The former is essentially the original scheme developed more than five decades ago, and has been primarily utilized for anti-jamming communications. The latter technique was proposed by Viterbi [1] in 1978. It is the direct result of his work towards a new multiple access method that can accommodate more potential users. The conventional technique was also examined by Cooper and Nettleton [2] around the same time as the Viterbi technique for possible use as a multiple access scheme.

2.1.1 Conventional Technique

The conventional FH-SS technique is basically a digital communication system in which

the carrier frequency of a modulated signal is dehopped across an allocated bandwidth under the control of a hopping pattern. The allocated bandwidth is usually much larger than the bandwidth of the modulated signal itself, and is commonly known as the spread-spectrum bandwidth. The modulation of the signal is often carried out by means of frequency shift keying (FSK), either binary or non-binary, for which noncoherent detection is feasible at the receiver. This feature of the FSK scheme is very important for the FH-SS system, since the phase of a dehopped signal is usually unknown and coherent detection is impractical.

The basic diagrams of a transmitter and a receiver for the conventional FH-SS system are depicted in Fig. 2.1(a) and 2.1(b), respectively. The hopping of a symbol is accomplished by multiplying the modulated signal with the output of the frequency synthesizer. The rate at which the frequency synthesizer produces a hop frequency is called the hop rate. With respect to the hop rate, the FH-SS system can be divided into two classes: slow frequency hopping and fast frequency hopping. In a slow FH-SS system, each hop contains two or more symbols. In other words, the symbol rate is faster than the hop rate. On the other hand, in a fast FH-SS system, the hop rate is either equal to or faster than the symbol rate. For the latter case, a symbol is transmitted via several hop frequencies in different time intervals, resulting in a condition called frequency-time diversity. A symbol in each hop is sometimes called a chip.

At the receiver, a received signal is dehopped via multiplication of the received signal and a dehopping signal generated by the frequency synthesizer locally at the receiver. Usually, the dehopping signal is identical to that used by the transmitter. For fast frequency hopping, where one signal symbol is hopped more than once, a diversity combiner is employed at the receiver. This device makes use of the received chips to determine which symbol has been sent.

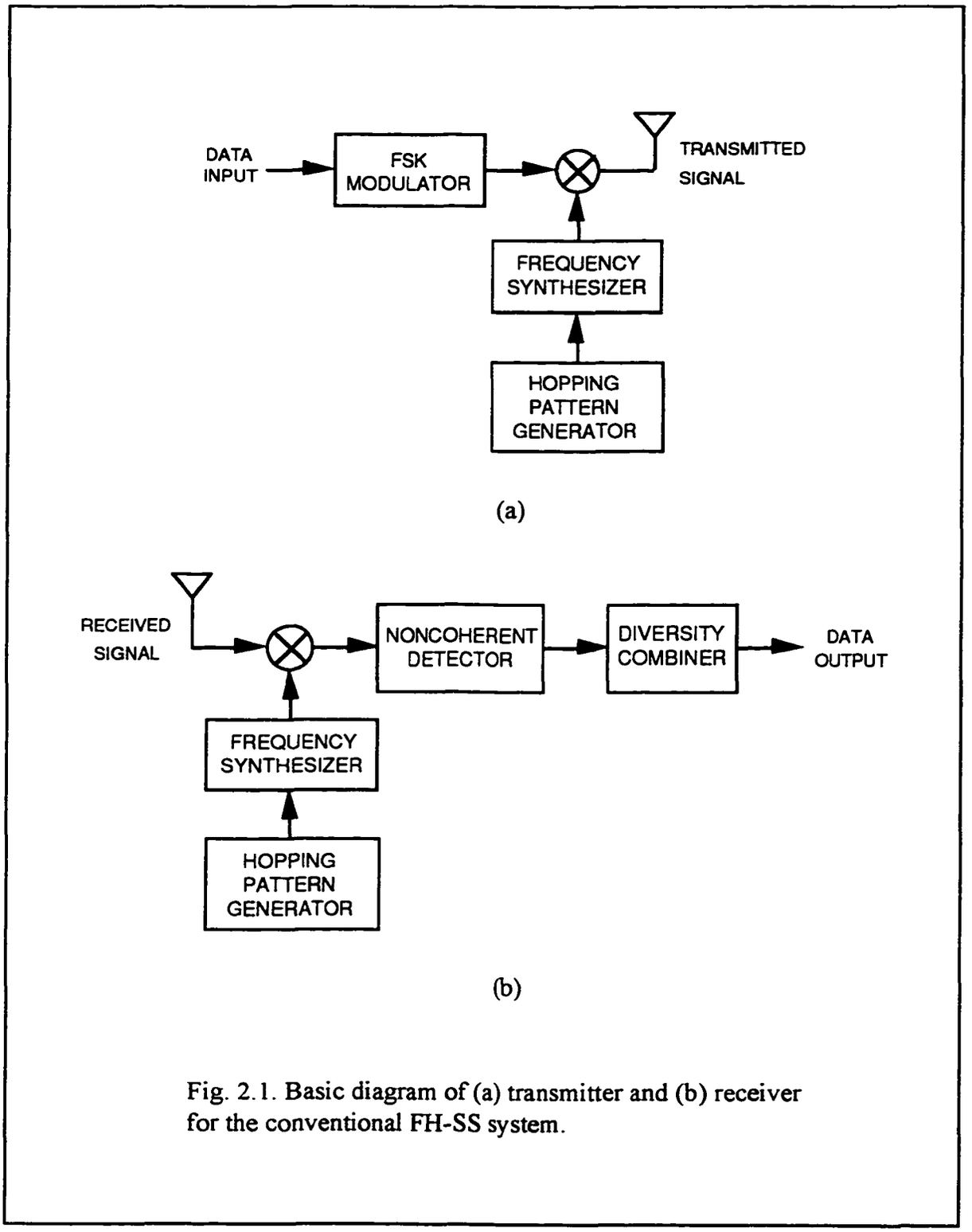

Fig. 2.1. Basic diagram of (a) transmitter and (b) receiver for the conventional FH-SS system.

In an FH-SSMA system, there will be multiple transmitter-receiver pairs, communicating with each other simultaneously over the same spread-spectrum bandwidth. Each user will be assigned a unique hopping pattern. However, collisions between the users' signals may occur and become more frequent as the number of users increases.

2.1.2 Viterbi's Technique

Viterbi's technique can be classified as a fast FH-SS technique with multilevel FSK modulation. In this technique, the spread-spectrum bandwidth is divided into subbands. The number of subbands is equal to the number of FSK bands of a signal symbol. If, for example, a symbol has K bits, the number of subbands is 2^K. The hopping of a symbol is carried out by means of modulo-2^K addition of the symbol and a series of K-bit code words (also called addresses). As a result, the symbol is hopped several times over the 2^K subbands. The number of hops per symbol depends on the number of code words contained in the series. Also, the addresses to which the symbol is hopped depend on the value of each code word.

The dehopping of a received symbol is simply done via a reverse process, i.e. the code word is modulo-2^K subtracted from the symbol. Since Viterbi's technique is used as a multiple access scheme, some of the subbands will be occupied by signals from other users who share the same bandwidth. Thus, from a user's point of view, the detected signals will comprise not only those intended for the user, but also those intended for other users. To cope with this problem, Viterbi uses a symbol decision technique called the majority logic decision method. A detailed description of this method will be provided in Chapter 3.

2.2 Fading in Communication Channels

Several channel measurements have revealed that the fading phenomena may be characterized by a wide variety of mathematical models. These models can range from the well-known Rayleigh distribution to the recently-discovered shadowed Rician distribution. In this section, the mathematical representations of the fading phenomena of interest in this dissertation are presented.

2.2.1 Rayleigh Fading

Rayleigh fading has been found to exist in most radio environments, and is frequently assumed in the literature. It is characterized by the distribution:

$$p(\Re) = \frac{\Re}{\sigma^2} \exp\left[-\frac{\Re^2}{2\sigma^2}\right], \qquad \Re \geq 0 \tag{2.1}$$

where $\Re$ is the fading variable and σ^2 is its variance. This distribution is commonly known as the Rayleigh distribution.

In a Rayleigh fading channel, the transmitted signal propagates and arrives at the receiver via several paths. Each path is due to the reflection of the signal from an object or objects located between the transmitter and the receiver. Generally, the received signal can be represented by two quadrature components [9]:

$$X = \Re\cos\Theta = \sum_k A_k \cos\theta_k \tag{2.2}$$

and

$$Y = \Re\sin\Theta = \sum_k A_k \sin\theta_k, \tag{2.3}$$

where X is referred to as the real component, and Y is the imaginary component. Each term in the summations represents the signal which arrives from a different path, having a random amplitude A and a phase θ. In general, $\{A_k\}$ are identically distributed. $\{\theta_k\}$ are uniform over $[0, 2\pi)$. If the number of paths is large, both X and Y can be approximated by a normal distribution with zero mean and variance σ^2. Moreover, X and Y are independent of each other. Thus, their joint distribution can be written as

$$p_{XY}(x, y) = \frac{1}{2\pi\sigma^2}\exp\left[-\frac{x^2+y^2}{2\sigma^2}\right]. \tag{2.4}$$

The above expression may be transformed to polar coordinates by using the relationship:

$$p(\Re, \Theta) = \Re p_{XY}(x = \Re\cos\Theta, y = \Re\sin\Theta). \tag{2.5}$$

Hence,

$$p(\Re, \Theta) = \frac{\Re}{2\pi\sigma^2}\exp\left[-\frac{\Re^2}{2\sigma^2}\right]. \tag{2.6}$$

By integrating (2.6) over the variable Θ, the expression for the Rayleigh distribution as given by (2.1) is obtained.

2.2.2 Rician Fading

When a line-of-sight (LOS) path between the transmitter and the receiver exists in conjunction with the reflected paths, the channel can be characterized by a Rician fading model. In this model, the quadrature components X and Y may be expressed as

$$X = \Re\cos\Theta = A_0\cos\theta_0 + \sum_k A_k\cos\theta_k \tag{2.7}$$

$$Y = \Re \sin\Theta = A_0 \sin\theta_0 + \sum_k A_k \sin\theta_k , \tag{2.8}$$

where A_0 and θ_0 are respectively the constant amplitude and phase of the LOS signal. Usually, this signal is called the specular component. The means of X and Y in the Rician fading case are $A_0\cos\theta_0$ and $A_0\sin\theta_0$, respectively. The variances of both components, however, are the same as those in the Rayleigh fading case. Therefore, the joint distribution of X and Y is given by

$$p_{XY}(x, y) = \frac{1}{2\pi\sigma^2}\exp\left[-\frac{(x - A_0\cos\theta_0)^2}{2\sigma^2} - \frac{(y - A_0\sin\theta_0)^2}{2\sigma^2}\right]. \tag{2.9}$$

Consequently,

$$p(\Re, \Theta) = \frac{\Re}{2\pi\sigma^2}\exp\left[-\frac{\Re^2 + A_0^2 - 2\Re A_0\cos(\theta_0 - \Theta)}{2\sigma^2}\right]. \tag{2.10}$$

Integrating (2.10) over Θ, it turns out that [10]:

$$p(\Re) = \frac{\Re}{\sigma^2}\exp\left[-\frac{\Re^2 + A_0^2}{2\sigma^2}\right] I_0\left(\frac{\Re A_0}{\sigma^2}\right), \qquad \Re \geq 0 \tag{2.11}$$

where $I_0(z)$ is the modified Bessel function of the first kind and zeroth order defined by

$$I_0(z) = \frac{1}{2\pi}\int_0^{2\pi} e^{z\cos\phi} d\phi . \tag{2.12}$$

The expression in (2.11) is referred to as the Rician density. It is sometimes called the generalized Rayleigh density [10] or the Nakagami-Rice density [11].

2.2.3 Shadowed Rician Fading

In a shadowed Rician fading channel, the specular amplitude A_0 of the Rician faded signal

is distributed lognormally due to shadowing between the transmitter and the receiver. The distribution of A_0 in this case is given by [12]

$$p(A_0) = \frac{1}{\sqrt{2\pi d_0} A_0} \exp\left[-\frac{(\ln A_0 - \mu)^2}{2d_0} \right], \tag{2.13}$$

where μ and d_0 are the mean and the variance of A_0, respectively.

By averaging (2.11) over the lognormal variate A_0, we obtain

$$\begin{aligned} p(\Re) &= \int_0^\infty p(\Re | A_0) p(A_0) dA_0 \\ &= \frac{\Re}{\sqrt{2\pi d_0}\sigma^2} \int_0^\infty \frac{1}{A_0} \exp\left[-\frac{(\ln A_0 - \mu)^2}{2d_0} - \frac{(\Re^2 + A_0^2)}{2\sigma^2} \right] I_0\left(\frac{\Re A_0}{\sigma^2} \right) dA_0, \end{aligned}$$

$$\Re \geq 0 \tag{2.14}$$

which is the probability density function of a shadowed Rician faded signal.

2.2.4 Nakagami Fading

Developed by Nakagami in the early 1940s, the Nakagami distribution is considered the most versatile distribution. It represents the entire range of fading distributions from one-sided Gaussian to non-fading [11], [13]. Also, the Nakagami distribution can well be used to fit the experiment data, such as those obtained from the HF skywave [13], the urban mobile channel [14], and the satellite channel [15] measurements. The Nakagami density function may be expressed as

$$p(\Re) = \frac{2m^m \Re^{2m-1}}{\Gamma(m)\Omega^m} \exp\left[-\frac{m\Re^2}{\Omega} \right], \qquad \Re \geq 0 \tag{2.15}$$

where $\Omega = \langle \Re^2 \rangle$ is the mean-square value of $\Re$, and

$$m = \frac{\Omega^2}{V\{\Re^2\}} \geq \frac{1}{2} \tag{2.16}$$

is the fading parameter which determines the shape of the distribution. $V\{\cdot\}$ in (2.16) denotes variance.

The expression in (2.15) is sometimes called the Nakagami-m distribution, which has the following properties:

1. If $m = 1/2$, the distribution becomes one-sided Gaussian.

2. If $m = 1$, the distribution becomes Rayleigh.

3. If $m \to \infty$, the distribution tends to an impulse function. That is, there is no fading.

Chapter 3

Performance of Viterbi's FH-SSMA System in Different Fading Environments

3.1 Introduction

Since it was first proposed, the Viterbi's FH-SSMA system has received much attention from researchers as it proves to outperform other conventional multiple access systems [1]. Primarily, this FH-SSMA system was proposed for use over a low-data-rate satellite link. However, Goodman *et al.* [7] have examined it for possible use in digital mobile radiotelephony. They found that a maximum of 209 users can be accommodated by this system under perfect transmission conditions, using a data rate of 32 kbit/s and a one-way bandwidth of 20 MHz. Moreover, Einarsson [16] and Timor [17] demonstrated that by using a properly designed hopping pattern in conjunction with an improved decoding scheme, a 50 to 60 percent increase in the system capacity can be achieved.

As mentioned earlier, the transmission channel is usually corrupted by impairments such as AWGN and multipath fading, resulting in signal detection errors and a consequent reduction in the system capacity. The analysis by Goodman *et al.* has shown that for the same data rate and bandwidth, both AWGN and Rayleigh multipath fading can reduce the capacity to 170 users at a signal-to-noise ratio (SNR) of 25 dB.

Another investigation by Muammar [8] has demonstrated that shadowing between the base station and the mobile users can further reduce the capacity drastically.

In this chapter, other types of fading are considered. Of particular interest are the Rician, shadowed Rician, and Nakagami fading, as there have been reports indicating that these fading phenomena do exist in certain mobile applications [12], [14], [18], [19], [36]. The analysis will be based on the system described in [7], using the same set of system parameters for comparison.

In the next section, the principle of the system operation is described. Section 3.3 demonstrates the derivation of the bit error probability. The expression for the false alarm probability is given in Section 3.4, whereas the derivations of the deletion probability for each fading case are conducted in Section 3.5. Section 3.6 includes numerical results as well as discussions. Then, a summary is provided in Section 3.7.

3.2 System Operation

The simplified block diagram of a transmitter is illustrated in Fig. 3.1(a). In this system, each user is assigned a unique hopping pattern which is a sequence of L K-bit code words, denoted here as

$$Y = \{Y_1, Y_2, \cdots, Y_L\}.$$

During a signaling period T, each code word is added modulo-2^K to the buffered K-bit message X of a user to produce a new (modulated) sequence Z of length L:

$$Z = X \oplus Y = \{Z_1, Z_2, \cdots, Z_L\}.$$

As a result, each modulated code word Z_l ($l = 1, 2, \cdots, L$) occupies a time slot of duration $\tau = T/L$ and takes on a value between 0 and $2^K - 1$ (see Fig. 3.1(b)). The

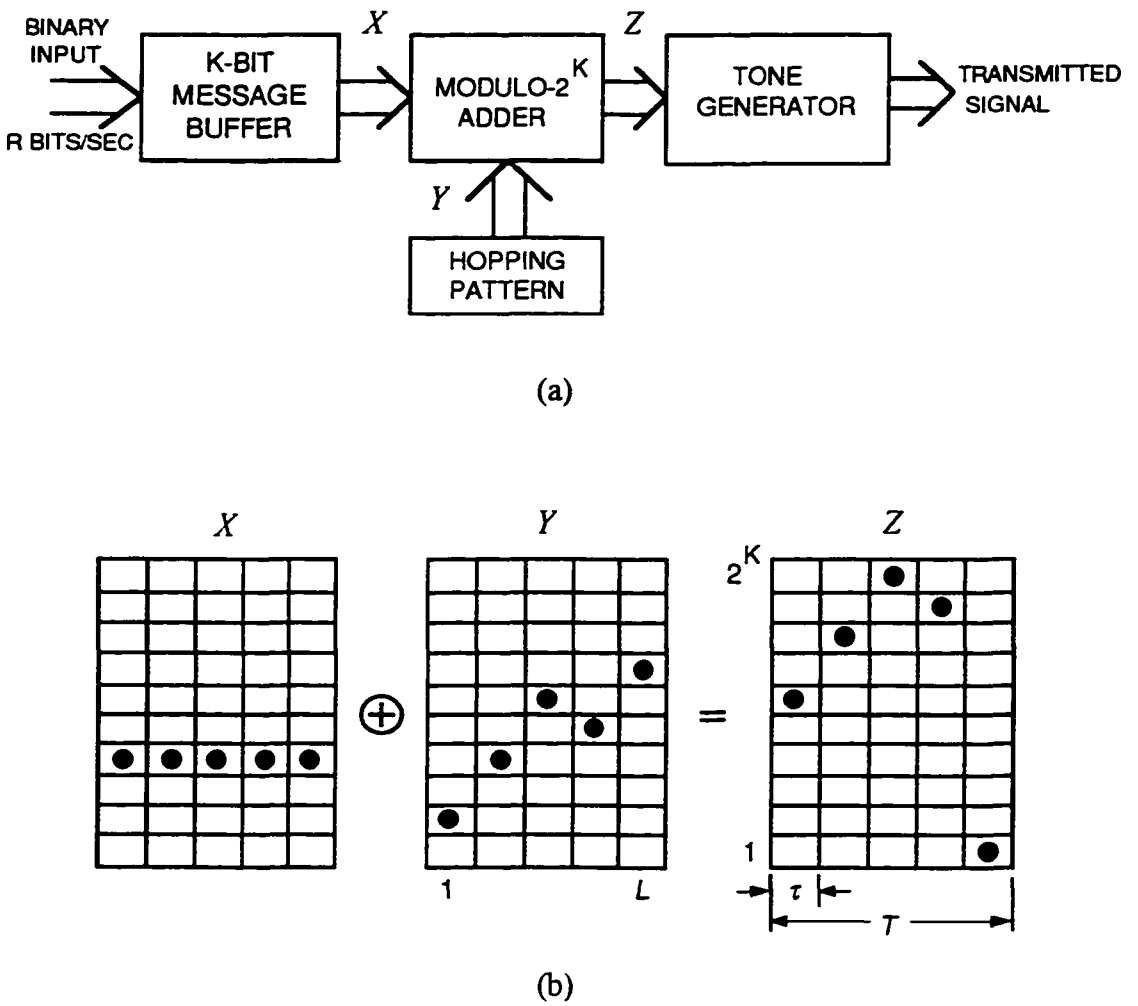

Fig. 3.1. (a) Simplified block diagram of a transmitter for Viterbi's FH-SSMA system. (b) Every T seconds, K-bit message X is modulo-2^K added to hopping pattern Y to produce modulated sequence Z with L code words. Each code word occupies a time slot of duration $\tau = T/L$.

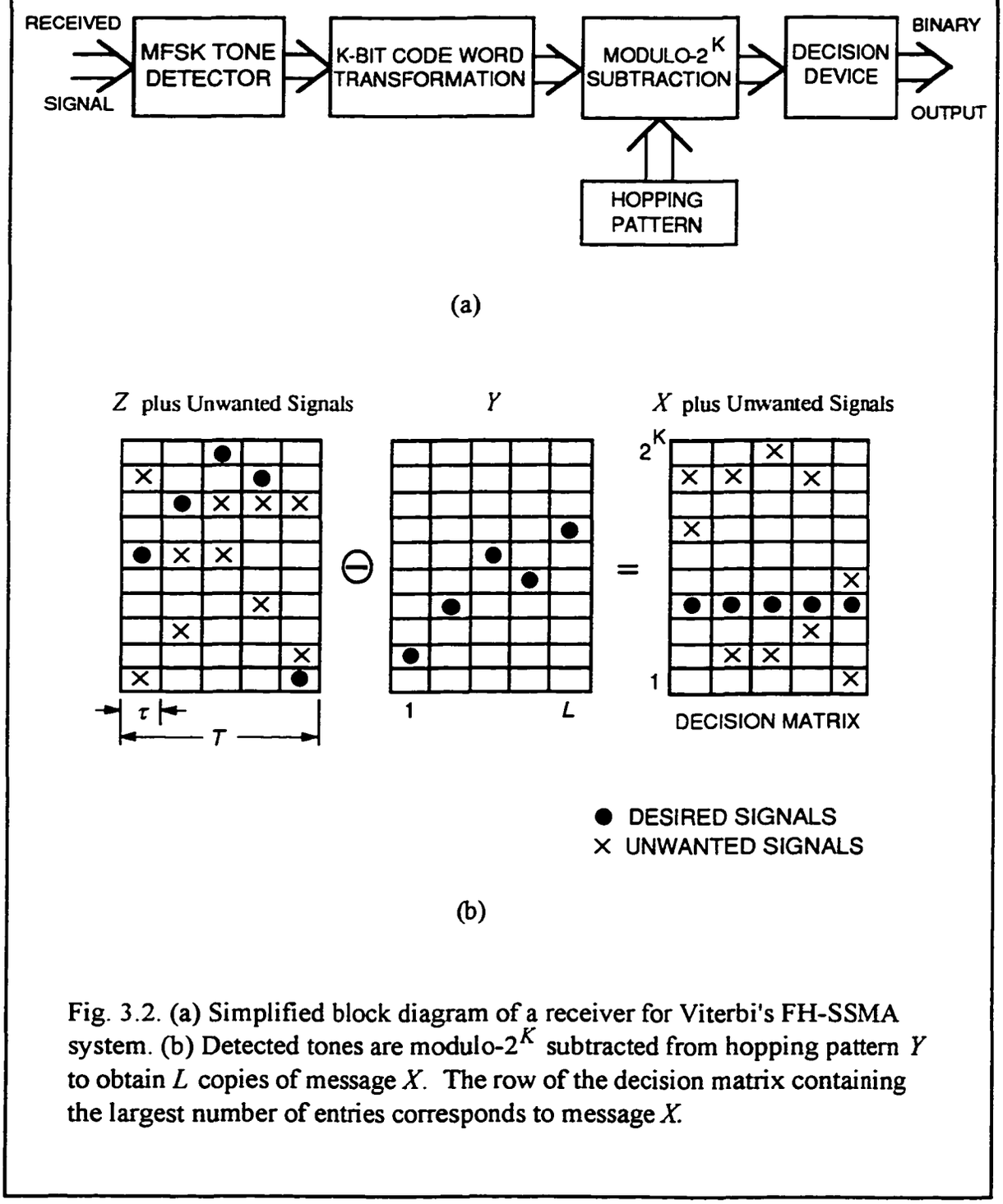

Fig. 3.2. (a) Simplified block diagram of a receiver for Viterbi's FH-SSMA system. (b) Detected tones are modulo-2^K subtracted from hopping pattern Y to obtain L copies of message X. The row of the decision matrix containing the largest number of entries corresponds to message X.

modulated sequence is then used by the tone generator to select the corresponding signal tones from the available 2^K orthogonal frequencies, which occupy the entire one-way spread-spectrum bandwidth.

At the receiver (Fig. 3.2(a)), each one of the 2^K frequency bins is determined every τ seconds whether or not a tone is present, by comparing the energy level in the frequency bin against a threshold level b. After the tones are detected, they are transformed back into the corresponding code words Z_l, and then subtracted modulo-2^K from the hopping pattern Y. By the end of the signaling period T, L copies of the original K-bit message X will be obtained.

In practice, however, the detected tones will not only come from the desired user itself, but also from other users in the system. Moreover, AWGN and multipath fading can cause a transmitted tone to be omitted (deletion), or a false tone to be incorrectly detected (false alarm). Thus, to make a decision under these circumstances, all detected tones (wanted and unwanted) are entered into a $2^K \times L$ decision matrix (Fig. 3.2 (b)). At this point the majority logic decision is made such that the row of the matrix having the largest number of entries is chosen as the correct one.

3.3 Probability of Bit Error

Let M be the number of active users in the system. It is assumed that all M hopping patterns are selected independently of each other. Each code word of the patterns is chosen equally likely over the 2^K possibilities. It is also assumed that all M modulated signal tones are generated independently with equal probability over the 2^K frequencies. The spacing between signal tones is assumed to be greater than the channel coherence bandwidth to ensure that the transmitted signals fade independently of each other. Also,

it is assumed that each hop is perfectly synchronized.

Based on the above assumptions, the bit error probability P_B may be derived as follows [7].

The probability that none of the $M-1$ interfering users sends a tone to a position in the decision matrix is

$$\left(1-2^{-K}\right)^{M-1}.$$

Thus, the probability of a tone being present in a position in the decision matrix is

$$1-\left(1-2^{-K}\right)^{M-1}.$$

Taking into account the probability P_D that a transmitted tone is deleted due to the AWGN and the multipath fading, and the probability P_F that a false tone is detected due to the AWGN, the overall probability of a tone being inserted in a position in the decision matrix is

$$p_I = p + P_F - pP_F, \tag{3.1}$$

where

$$p = \left[1-\left(1-2^{-K}\right)^{M-1}\right]\left(1-P_D\right). \tag{3.2}$$

It then follows that the probability of j entries in a row of the decision matrix is

$$P_s(j) = \binom{L}{j} p_I^j \left(1-p_I\right)^{L-j}. \tag{3.3}$$

Consider the 2^K-1 incorrect rows, the probability that n is the maximum number of entries and exactly k rows contain n entries is

$$P(n,\ k)=\binom{2^K-1}{k}\left[P_s(n)\right]^k\left[\sum_{m=0}^{n-1}P_s(m)\right]^{2^K-1-k}. \tag{3.4}$$

Now consider the correct row, which contains the desired signals. The probability of an entry being present in a position in this row is $1-P_D$. Therefore, the probability that there are i entries in this row is

$$P_c(i)=\binom{L}{i}\left(1-P_D\right)^i P_D^{L-i}. \tag{3.5}$$

To obtain the expression for the bit error probability, let us observe that if $n>i$, an error will occur with certainty. If $n=i$, a correct decision will be made with probability $1/(k+1)$. As a result, the word error probability is given by

$$P_W=1-\sum_{i=0}^{L}P_c(i)\sum_{k=0}^{2^K-1}\frac{1}{k+1}P(i,\ k). \tag{3.6}$$

Consequently, the bit error probability can be expressed as

$$P_B=\frac{2^{K-1}}{2^K-1}P_W. \tag{3.7}$$

It is worth noting here that the derivation above assumes statistical independence between the rows of the decision matrix. The validity of this assumption has been justified by Yan and Wang [20] who developed a more complicated dependence model and compared it with the independence model. The researchers have shown that both models produce nearly identical results. Furthermore, these results have also been substantiated by Belezinis and Turner [21] by means of a computer simulation.

3.4 False Alarm Probability

As mentioned earlier, AWGN and multipath fading may produce false alarms or deletions. Since these channel impairments possess random characteristics, both false alarms and deletions can be expressed in terms of probability. By considering the transmission of each tone as an example of noncoherent on-off keying, we can define the probability of false alarm, P_F, as the probability that the threshold will be exceeded by an energy level in a frequency bin containing no signal. This energy basically comes from the background noise. The expression for the false alarm probability is readily available in the textbook by Schwartz *et al.* [22] and is repeated here as follows:

$$P_F = \exp\left[-\frac{b_0^2}{2}\right], \tag{3.8}$$

where $b_0 = b/\sqrt{N}$ denotes the actual threshold level b normalized by the average noise power N.

3.5 Deletion Probability

Unlike false alarms, deletions are largely due to both multipath fading and AWGN. Therefore, different types of fading will lead to different deletion probabilities. The probability of deletion may be defined as the probability that the envelope of a tone is smaller in magnitude than a threshold. The expressions for this probability are derived in the following subsections.

Throughout the analysis, it is assumed that the detector is perfectly synchronized with the signal. Also, neither the intersymbol interference nor the Doppler effect plays any significant role in the detection process.

3.5.1 Rician Fading

According to recent experiments, Rician fading has been found to occur in indoor [18], [36] and urban microcellular environments [19]. As discussed in Section 2.2, a signal passing through a Rician channel will emerge as a composite of a specular component and a multipath portion. The multipath portion is characterized by Gaussian quadrature random variables (Rayleigh amplitude). When the signal is also subject to the AWGN, the noise itself will supply additional quadrature components to the multipath portion of the signal, thereby producing a new pair of Gaussian quadrature random variables [23]. As a result, the envelope, v, of the received signal can be expressed as

$$p(v) = \frac{v}{N+\alpha}\exp\left[-\frac{v^2+u^2}{2(N+\alpha)}\right]I_0\left(\frac{vu}{N+\alpha}\right), \qquad v \geq 0 \tag{3.9}$$

where N is the average noise power, u is the amplitude of the specular component, and α is the average power of the multipath portion.

The probability of deletion is then given as

$$\begin{aligned} P_D &= \text{Prob}(v < b) \\ &= \int_0^b p(v)dv = 1 - \int_b^\infty p(v)dv \\ &= 1 - \int_b^\infty \frac{v}{N+\alpha}\exp\left[-\frac{v^2+u^2}{2(N+\alpha)}\right]I_0\left(\frac{vu}{N+\alpha}\right)dv, \end{aligned} \tag{3.10}$$

where b is the threshold level. Letting $v = x\sqrt{N+\alpha}$ and carrying out the transformation yield

$$P_D = 1 - \int_{b/\sqrt{N+\alpha}}^\infty x\exp\left[-\frac{x^2}{2} - \frac{u^2}{2(N+\alpha)}\right]I_0\left(\frac{xu}{\sqrt{N+\alpha}}\right)dx. \tag{3.11}$$

For Rician fading, we define a parameter, called *Rician factor*, as:

$$\rho = \frac{\text{power in specular component}}{\text{power in multipath component}} = \frac{u^2}{2\alpha}.$$

This parameter has been found in [18], [19], and [36] to vary between 6 and 12 dB in value, depending on the characteristics of the surroundings along the propagation path. If we define the average SNR as

$$\gamma_0 = \frac{1}{N}\left(\frac{u^2}{2} + \alpha\right), \tag{3.12}$$

the relationship between the Rician factor and the SNR can be given by

$$\frac{u^2}{2N} = \frac{\rho\gamma_0}{1+\rho}, \tag{3.13}$$

$$\frac{\alpha}{N} = \frac{\gamma_0}{1+\rho}. \tag{3.14}$$

Substituting (3.13) and (3.14) into (3.11), the deletion probability becomes

$$\begin{aligned} P_D &= 1 - \int_{b_1}^{\infty} x \exp\left[-\frac{x^2}{2} - \frac{\rho\gamma_0}{1+\rho+\gamma_0}\right] I_0\left(x\sqrt{\frac{2\rho\gamma_0}{1+\rho+\gamma_0}}\right) dx \\ &= 1 - Q\left(\sqrt{\frac{2\rho\gamma_0}{1+\rho+\gamma_0}},\ b_1\right), \end{aligned} \tag{3.15}$$

where

$$b_1 = \frac{b}{\sqrt{N}\sqrt{1+\left(\gamma_0/(1+\rho)\right)}} = \frac{b_0}{\sqrt{1+\left(\gamma_0/(1+\rho)\right)}}$$

and $Q(a, b)$ is Marcum's Q function given by

$$Q(a, b) = \int_b^{\infty} x \exp\left[-\frac{a^2+x^2}{2}\right] I_0(ax)dx. \tag{3.16}$$

Note that as ρ approaches infinity (i.e. $\alpha \to 0$ or, equivalently, no multipath component), (3.15) reduces to the P_D expression for the non-fading case shown in [22, Eqn. (7-4-7)]:

$$P_D = 1 - Q\left(\sqrt{2\gamma}, b_0\right), \tag{3.17}$$

where $\gamma = u^2/2N$. On the other hand, as $\rho = 0$ (no specular component), (3.15) becomes

$$P_D = 1 - \exp\left[-\frac{b_0^2}{2(1+\gamma_0)}\right], \tag{3.18}$$

which is the deletion probability for the Rayleigh fading case considered in [7].

3.5.2 Shadowed Rician Fading

The result of an experiment conducted by Loo [12] has indicated that a land mobile satellite channel can be characterized by a shadowed Rician fading model. In this model the specular component of the signal is lognormally distributed due to foliage shadowing. The probability density function for the envelope, v, of a signal that propagates through the land mobile satellite channel can be expressed as [24]

$$p(v) = \frac{v}{(N+\alpha)\sqrt{2\pi d_0}} \int_0^\infty \frac{1}{u} \exp\left[-\frac{(\ln u - \mu)^2}{2d_0} - \frac{\left(u^2+v^2\right)}{2(N+\alpha)}\right] I_0\left(\frac{uv}{N+\alpha}\right) du,$$

$$v \geq 0 \tag{3.19}$$

where N and α are the noise and multipath power respectively. μ is the mean value due to shadowing, and d_0 is the variance due to shadowing as well. Consequently, the probability of deletion may be given by

$$P_D = 1 - \int_b^\infty p(v)dv$$

$$= 1 - \int_b^\infty \frac{v}{(N+\alpha)\sqrt{2\pi d_0}} \int_0^\infty \frac{1}{u} \exp\left[-\frac{(\ln u - \mu)^2}{2d_0} - \frac{(u^2+v^2)}{2(N+\alpha)} \right] I_0\left(\frac{uv}{N+\alpha} \right) du dv. \tag{3.20}$$

Interchanging the order of integrations and rearranging the integrands result in:

$$P_D = 1 - \int_0^\infty \frac{1}{u\sqrt{2\pi d_0}} \exp\left[-\frac{(\ln u - \mu)^2}{2d_0} \right] \int_b^\infty \frac{v}{(N+\alpha)} \exp\left[-\frac{(u^2+v^2)}{2(N+\alpha)} \right] I_0\left(\frac{uv}{N+\alpha} \right) dv du. \tag{3.21}$$

By letting $v = x\sqrt{N+\alpha}$ and carrying out the transformation, the integral with respect to v becomes

$$F = \int_{b_0/\sqrt{1+(\alpha/N)}}^\infty x \exp\left[-\frac{x^2}{2} - \frac{u^2}{2(N+\alpha)} \right] I_0\left(\frac{xu}{\sqrt{N+\alpha}} \right) dx$$

$$= Q\left(\frac{u}{\sqrt{N+\alpha}}, \frac{b_0}{\sqrt{1+(\alpha/N)}} \right). \tag{3.22}$$

Substituting (3.22) into (3.21) yields

$$P_D = 1 - \int_0^\infty \frac{1}{u\sqrt{2\pi d_0}} \exp\left[-\frac{(\ln u - \mu)^2}{2d_0} \right] Q\left(\frac{u}{\sqrt{N+\alpha}}, \frac{b_0}{\sqrt{1+(\alpha/N)}} \right) du. \tag{3.23}$$

The above expression can be simplified further by a change of variable $y = (\ln u - \mu)/\sqrt{d_0}$ which gives

$$P_D = 1 - \frac{1}{\sqrt{2\pi}} \int_{-\infty}^\infty \exp\left[-\frac{y^2}{2} \right] Q\left(\frac{e^{y\sqrt{d_0}+\mu}}{\sqrt{N+\alpha}}, \frac{b_0}{\sqrt{1+(\alpha/N)}} \right) dy. \tag{3.24}$$

3.5.3 Nakagami Fading

In [14], Suzuki has discovered that for certain urban mobile environments the channel is best described by the Nakagami-*m* distribution. In this case, the amplitude u of a received signal is expressed as

$$p(u) = \frac{2m^m u^{2m-1}}{\Gamma(m)\Omega^m} \exp\left[-\frac{mu^2}{\Omega}\right], \qquad u \geq 0 \tag{3.25}$$

where $\Omega = \langle u^2 \rangle$ is the mean-square value of u, and

$$m = \frac{\Omega^2}{V\{u^2\}}.$$

Now let us define the SNR as

$$\gamma = \frac{u^2}{2N} \tag{3.26}$$

which is a one-to-one random variable transformation. Therefore, γ can be characterized by the following distribution:

$$\begin{aligned} p(\gamma) &= p\left(u = \sqrt{2N\gamma}\right)\left|\frac{du}{d\gamma}\right| \\ &= \frac{m^m \gamma^{m-1}}{\Gamma(m)\gamma_0^m} \exp\left[-\frac{m\gamma}{\gamma_0}\right], \qquad \gamma \geq 0 \end{aligned} \tag{3.27}$$

where $\gamma_0 = \Omega/2N$ is the average SNR (over fading).

Consider for the moment a signal that passes through a fading-free but noisy channel. The probability density function of the signal envelope, v, can be written as [22]

$$p(v) = \frac{v}{N} \exp\left[-\frac{u^2 + v^2}{2N}\right] I_0\left(\frac{uv}{N}\right), \tag{3.28}$$

where u is the signal amplitude. The probability of deletion is then given by

$$P_D = \int_0^b p(v)dv$$

$$= \int_0^b \frac{v}{N}\exp\left[-\frac{u^2+v^2}{2N}\right]I_0\left(\frac{uv}{N}\right)dv. \tag{3.29}$$

Using the definition of the SNR in (3.26), and carrying out a simple change of variable $x = v/\sqrt{N}$, we can express the deletion probability in terms of γ as

$$P_D = \int_0^{b_0} x\exp\left[-\frac{x^2+2\gamma}{2}\right]I_0\left(x\sqrt{2\gamma}\right)dx, \tag{3.30}$$

where $b_0 = b/\sqrt{N}$ is the normalized threshold level.

For the channel that is corrupted by both the AWGN and Nakagami fading, (3.30) becomes conditioned on the random variable γ, whose density function is given by (3.27). Hence, the overall probability may be obtained by averaging (3.30) over (3.27) to yield

$$P_D = \int_0^{\infty}\int_0^{b_0} \frac{m^m\gamma^{m-1}x}{\Gamma(m)\gamma_0^m}\exp\left[-\frac{m\gamma}{\gamma_0}\right]\exp\left[-\frac{x^2+2\gamma}{2}\right]I_0\left(x\sqrt{2\gamma}\right)dxd\gamma. \tag{3.31}$$

Equation (3.31) can be simplified further (see Appendix A) to give:

$$P_D = \left(\frac{m}{\gamma_0}\right)^m \frac{b_0^2}{2}\exp\left[-\frac{b_0^2}{2}\right]\sum_{k=0}^{\infty}\frac{(m)_k\left(-m/\gamma_0\right)^k}{k!}{}_1F_1\left(m+k+1;\ 2;\ \frac{b_0^2}{2}\right) \tag{3.32}$$

where ${}_1F_1(a;\ b;\ z)$ is the confluent hypergeometric function defined as

$${}_1F_1(a;\ b;\ z) = \sum_{n=0}^{\infty}\frac{(a)_n z^n}{(b)_n n!}, \tag{3.33}$$

where

$$(a)_n = a(a+1)\cdots(a+n-1),\ (a)_0 = 1.$$

For the special case of $m = 1$, it is shown in Appendix B that (3.32) reduces to (3.18)—the expression for the Rayleigh fading case.

3.6 Numerical Results and Discussions

In this section, the capacity of the FH-SSMA system is evaluated. To obtain the maximum capacity at a specific value of data rate R, bandwidth W, and bit error rate P_B, a search method is employed, where optimal values of K and L that maximize the number of simultaneous users are determined. It is found that for $R = 32$ kbit/s, $W = 20$ MHz, and $P_B \leq 10^{-3}$, the optimum values of K and L are 8 and 19, respectively [7].

3.6.1 Rician Fading Case

To evaluate P_D in (3.15), an algorithm developed by Parl [25] for calculating the Q function is employed.

Fig. 3.3 illustrates the performance curves of the FH-SSMA system operating at SNR = 25 dB with ρ ranging from 2 to 10 dB. The curves for the Rayleigh fading case ($\rho = 0$) and non-fading case ($\rho \to \infty$) are also provided in the figure for comparison. For each value of ρ, the detection threshold b_0 is optimized at $P_B = 10^{-3}$ in order to maximize the number of users. From the figure, it can be observed that as ρ increases to 10 dB or greater, the performance curve is identical to that for the non-fading case. This phenomenon is simply due to the fact that at a high value of ρ, the multipath portion of the signal is very small and has a negligible effect on the system performance. On the other hand, as ρ decreases, the signal contains more of the multipath component, causing

the curves to lie closer to that of the Rayleigh fading case. Also, it can be seen that the number of users at $P_B = 10^{-3}$ is reduced from 209 in the non-fading case to 182 in the $\rho = 2$ dB case. This is equivalent to a 13 percent reduction in the capacity. However, at this value of ρ, the Rician fading capacity is 7 percent (12 users) higher than that for the Rayleigh fading case (which is 170 users).

To show how the system capacity depends on the SNR level, the maximum number of users that can be accommodated by the system at $P_B \leq 10^{-3}$ is plotted against the SNR in Fig. 3.4 with ρ as a parameter. In this figure, the detection threshold is optimized at each value of SNR. The figure reveals that at high values of ρ, there is only a slight variation in the system capacity as the SNR becomes greater than 20 dB. For example, the difference between the maximum capacity and the capacity at SNR = 20 dB is eight users for $\rho = 8$ dB and two users for $\rho = 10$ dB. However, as the SNR drops below 20 dB, the variation becomes stronger no matter what the value of ρ is. These observations may be justified by the fact that at large ρ, the signal contains a small amount of multipath portion. Hence its chance of being deleted due to the deep fade is rare, if the SNR is high enough. On the contrary, when the SNR is low, the signal will be affected more by both the fading and the noise, thereby causing a more substantial variation in the number of users. It is also noted that the rate of change will increase as ρ decreases. In the worst case where $\rho = 0$ dB (Rayleigh fading), the capacity is reduced from 206 users to 95 users, equivalent to 54 percent, as the SNR decreases from 40 dB to 15 dB. In the least severe case where $\rho = 12$ dB, the number of users begins to drop when the SNR is less than 18.6 dB from 209 to 200 at SNR = 15 dB.

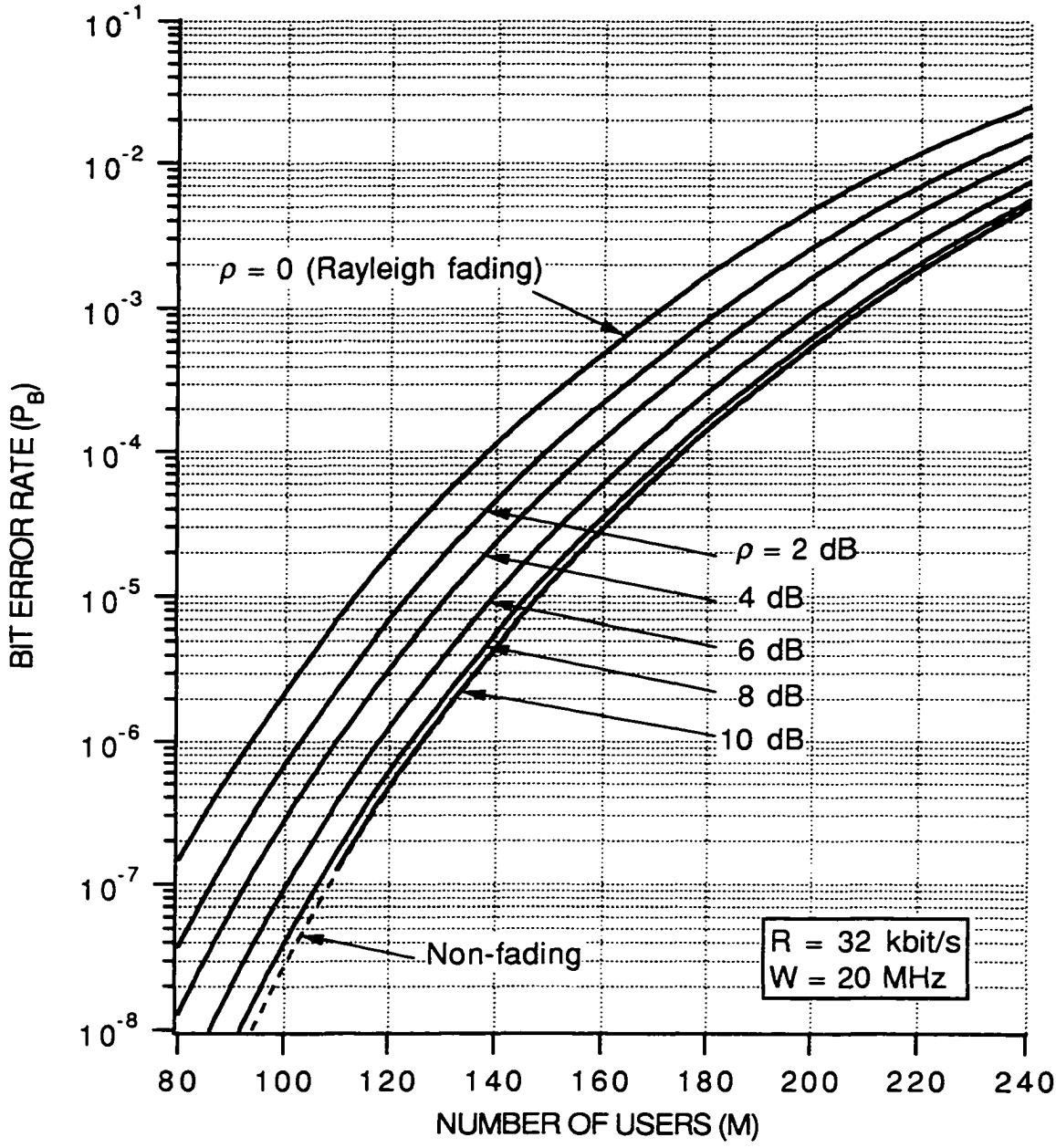

Fig. 3.3. Performance curves of Viterbi's FH-SSMA system operating at SNR = 25 dB, under the influence of Rician fading.

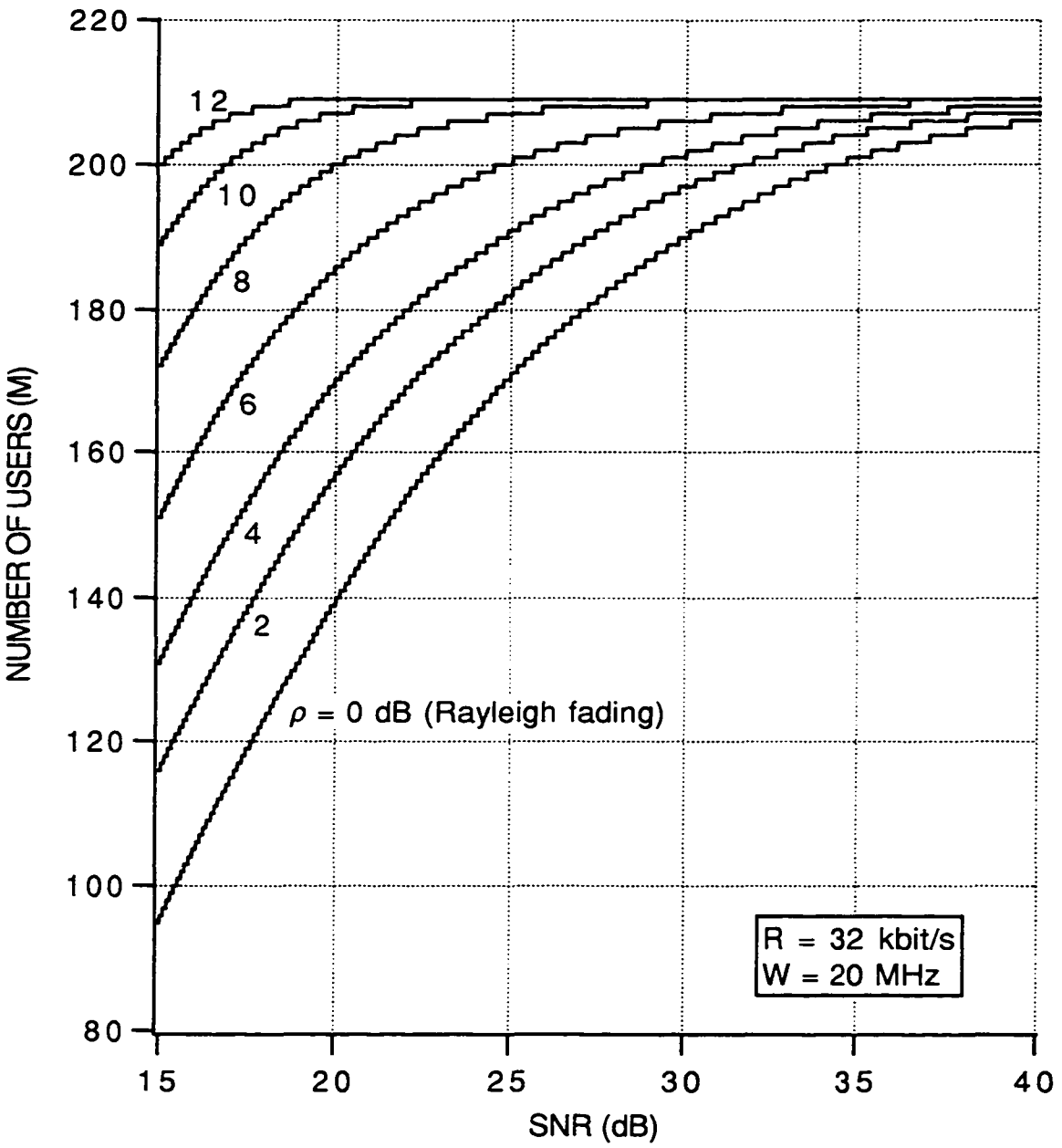

Fig. 3.4. Maximum capacity of Viterbi's FH-SSMA system in Rician fading channel at $P_B \leq 10^{-3}$ versus the signal-to-noise ratio with ρ (the Rician factor) as a parameter.

3.6.2 Shadowed Rician Fading Case

In Loo's experiment [12], three shadowing scenarios, namely light, average, and heavy, were considered. The values of the channel parameters corresponding to each scenario, available in [24] and also used in [26] and [27], are re-tabulated here in Table 3.1.

TABLE 3.1

Channel Model (Shadowing) Parameters

	Light	Average	Heavy
Multipath power α	0.158	0.126	0.0631
Mean μ	0.115	-0.115	-3.91
Standard deviation $\sqrt{d_0}$	0.115	0.161	0.806

In all signal-to-noise ratio calculations, we need to offset the noise power $N=(2\gamma_0)^{-1}$ by multiplying it with the channel gain $G_c=\exp(2\mu+2d_0)+2\alpha$, simply because G_c is not equal to unity [26], [27]. Furthermore, since shadowing is slow in comparison to the hopping rate, it is necessary to assume that interleaving be applied to the address sequence. This assumption will ensure that any two consecutive hops are independent of each other. Thus, the set of formulas given in Section 3.3 can be used in this case.

The bit error performance as a function of the number of users is illustrated in Fig. 3.5. Again, in this figure, SNR = 25 dB is assumed. The detection threshold is optimized at $P_B=10^{-3}$. The Rayleigh fading and non-fading curves are also provided in the figure for comparison. It is observed from the figure that for the light shadowing scenario, the

capacity of the system at $P_B = 10^{-3}$ is 199 users, which is approximately 5 percent lower than that for the non-fading case. For the average shadowing scenario, the capacity is found to be 192 users. In the worst case—heavy shadowing—the capacity is reduced to 170 users, as it is in the Rayleigh fading case. The reason is that in the heavy shadowing scenario, the power of the specular component is diminished so significantly that the signal is composed mainly of the multipath component. Therefore, the signal appears to be Rayleigh distributed.

Fig. 3.6 demonstrates how the system capacity varies with the SNR. For the light and average shadowing scenarios, as the SNR is decreased from 40 dB to 15 dB, the number of users drops from 209 and 208 down to 146 and 134, respectively. For the heavy shadowing scenario, the decrease is identical to that for the Rayleigh fading case shown earlier in Fig. 3.4 (from 206 to 95 users).

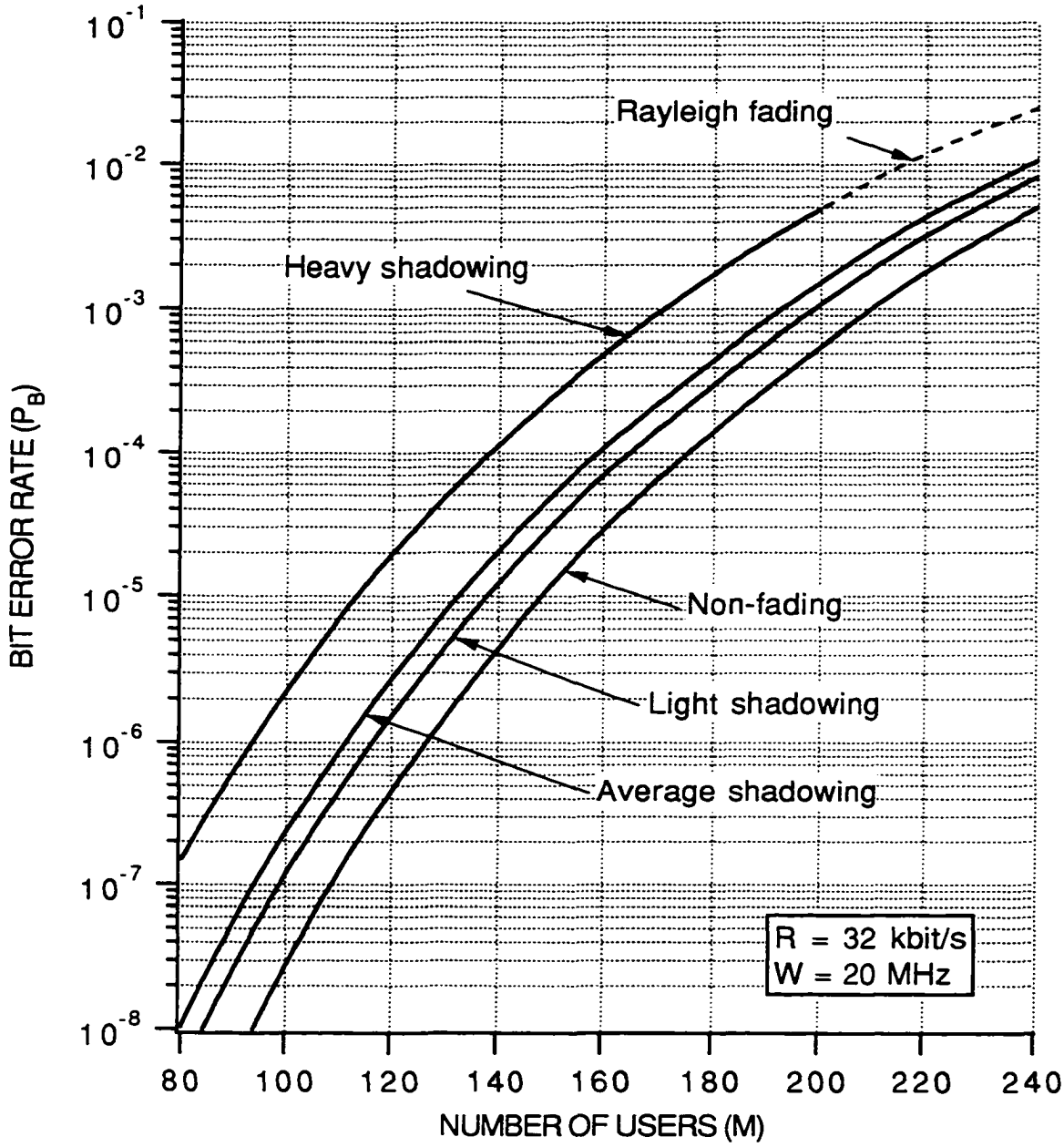

Fig. 3.5. Performance curves of Viterbi's FH-SSMA system operating at SNR = 25 dB, under the influence of shadowed Rician fading.

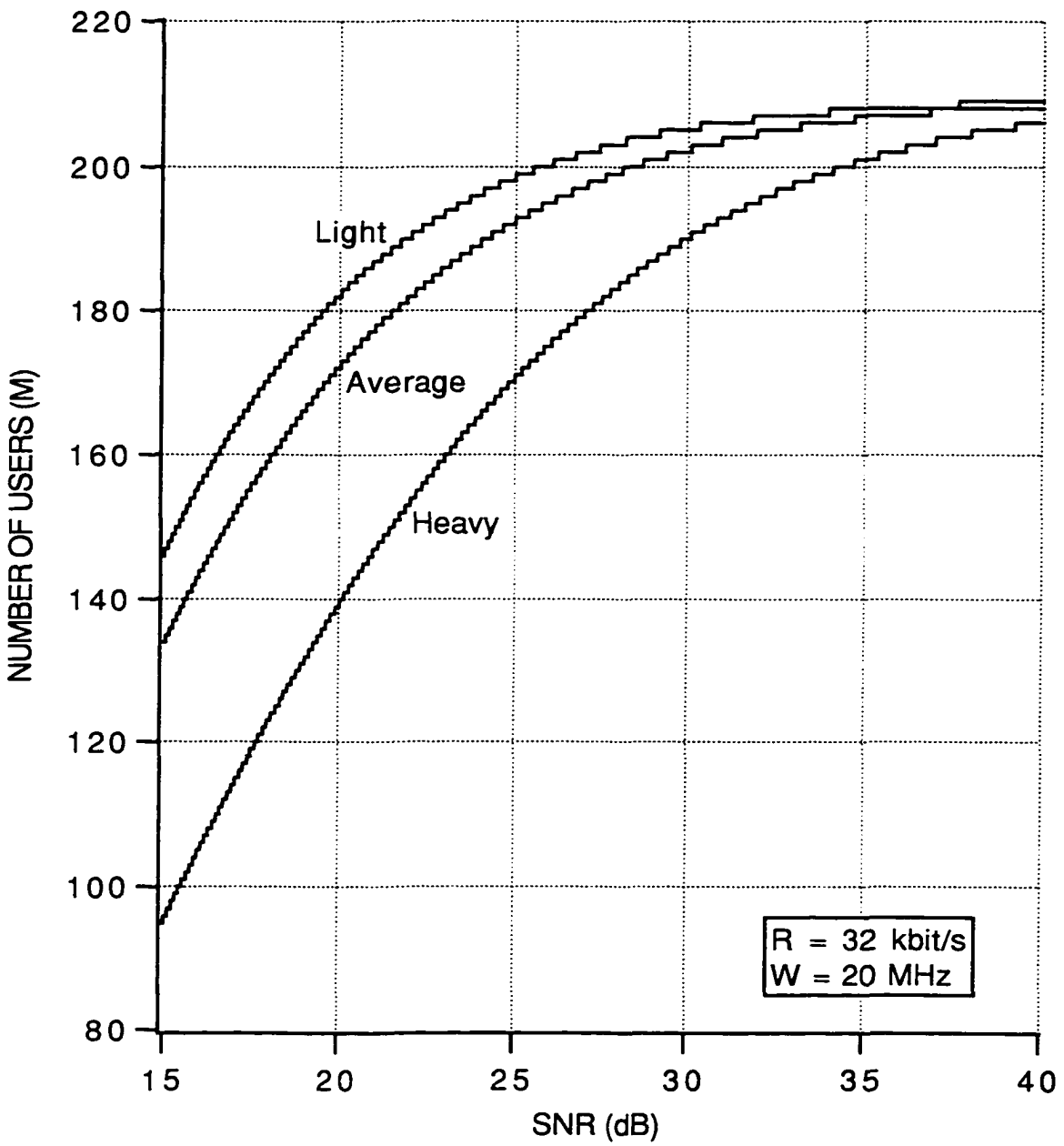

Fig. 3.6. Maximum capacity of Viterbi's FH-SSMA system in shadowed Rician fading channel at $P_B \leq 10^{-3}$ versus the signal-to-noise ratio.

3.6.3 Nakagami Fading Case

With the SNR set to 25 dB and the detection threshold optimized at $P_B = 10^{-3}$, the capacity curves for the Nakagami fading case are plotted in Fig. 3.7. Each curve in the figure represents the capacity of the system for different values of the fading parameter m, ranging from 0.5 up to 2.5. Where m is greater than 2.5, the curve is identical to the non-fading curve. At the other extreme where $m = 0.5$, the figure shows that the system can accommodate only 107 users. This number is 37 and nearly 50 percent lower than that for the Rayleigh fading case and the non-fading case, respectively.

Fig. 3.8 illustrates a plot between the maximum number of users at $P_B \leq 10^{-3}$ versus the SNR with m as a parameter. Similarly, the detection threshold is optimized at each SNR value. For $m = 2.5$, the system capacity is reduced from 209 to 160 users (equivalent to 23 percent) as the SNR decreases from 40 to 15 dB. However, the rate of the reduction is higher for smaller values of m. For example, in the worst case of $m = 0.5$, the number of users is reduced by 72 percent for the same range of SNR.

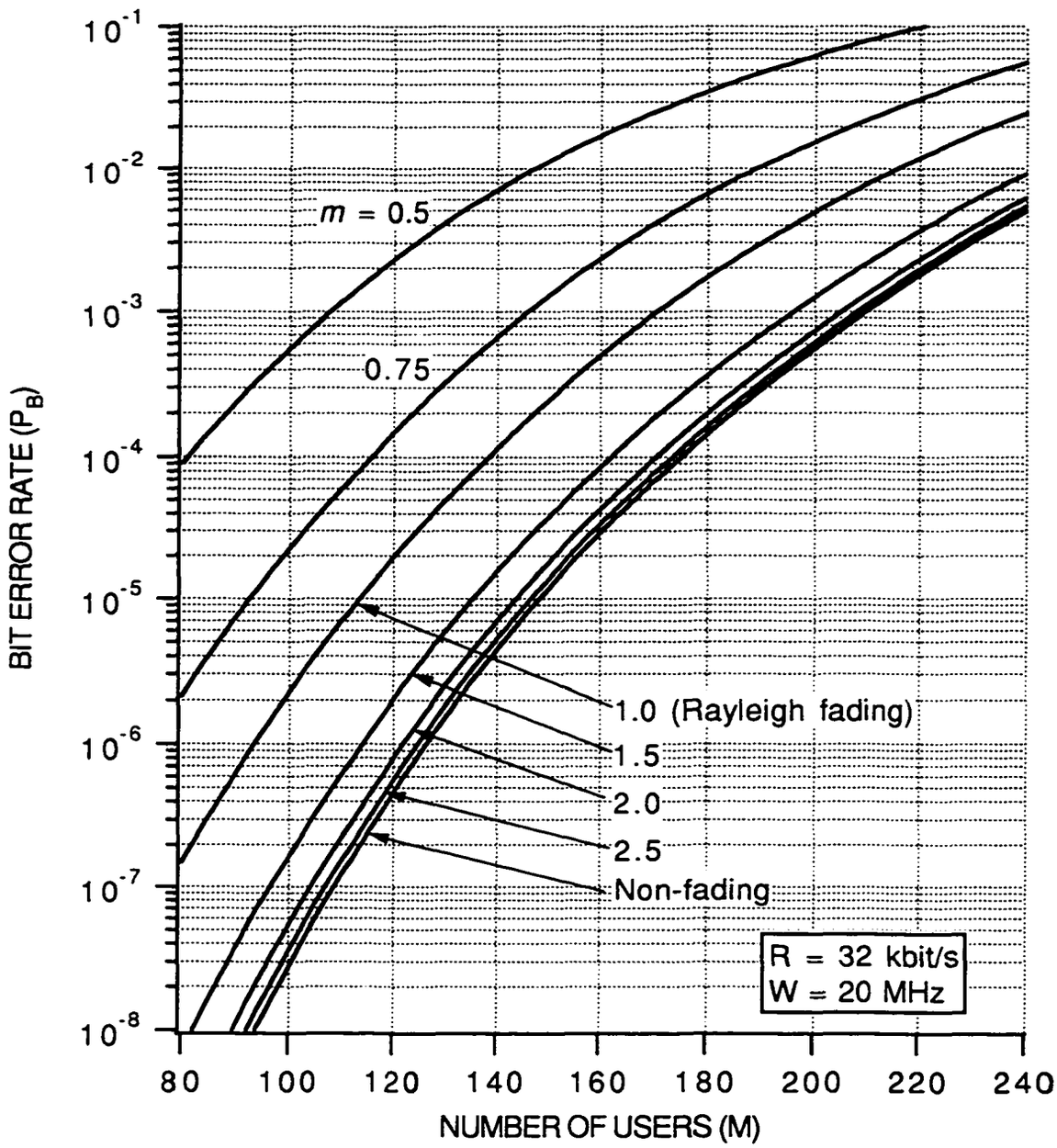

Fig. 3.7. Performance curves of Viterbi's FH-SSMA system operating at SNR = 25 dB, under the influence of Nakagami fading.

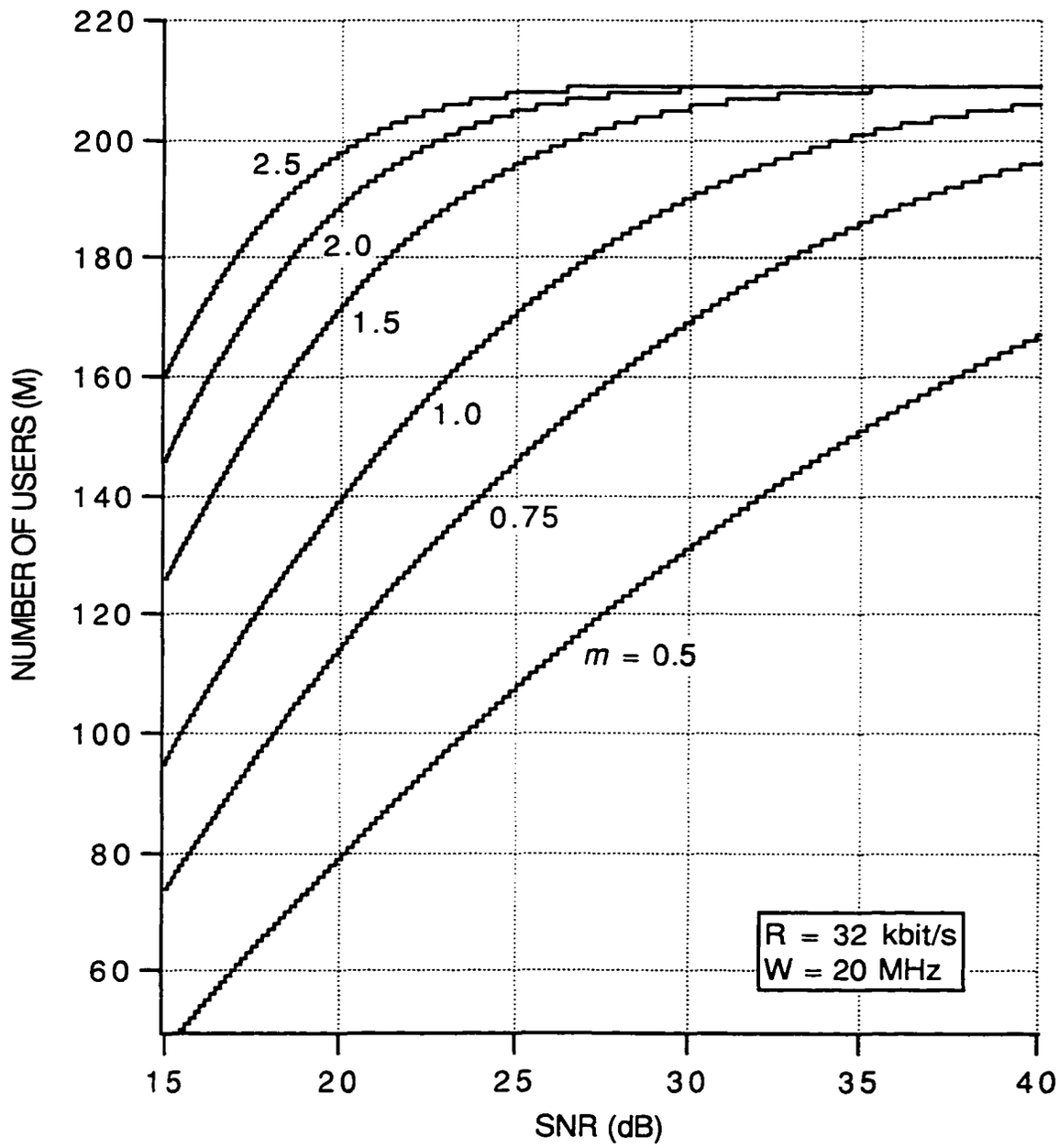

Fig. 3.8. Maximum capacity of Viterbi's FH-SSMA system in Nakagami fading channel at $P_B \leq 10^{-3}$ versus the signal-to-noise ratio with m as a parameter.

3.7 Summary

In this chapter, the performance of Viterbi's FH-SSMA system in Rician, shadowed Rician, and Nakagami fading channels was investigated. The expressions for the deletion probability were derived. The system capacity for each fading case was evaluated. Also, the influence of the variation in the SNR level on the system capacity was examined.

For Rician fading, it was found that when ρ is as low as 2 dB, the capacity is reduced by 13 percent in comparison to the non-fading case. Furthermore, it was demonstrated that higher values of ρ give rise to a smaller reduction in the capacity as the SNR decreases.

For shadowed Rician fading, three shadowing scenarios were considered according to previous experiments. It was shown that the heavy shadowing scenario yields exactly the same performance as that for the Rayleigh fading case. Whereas, the capacity for the light and average shadowing scenarios is slightly lower than the non-fading capacity.

Finally, for Nakagami fading, a range of fading parameters m (from 0.5 to 2.5) was used in the numerical analysis. At $m = 0.5$, the system capacity was found to decrease drastically by nearly 50 percent in comparison to the non-fading capacity. It was further revealed that as the SNR is reduced, the number of users at a lower value of m decreases faster than it would at a higher value of m.

Chapter 4

Performance of a Cellular FH-SSMA System in an Indoor Environment

4.1 Introduction

Recently, there has been an increased interest in utilizing radio for data and voice communications in the workplace. This type of communication, for example, will allow workers to move freely without being connected to one place by cords, or permit mobile robots to roam freely in a factory. A radio system will also reduce or perhaps eliminate wiring in a new building, and allow an extension of communication services in an old building to be done easily without rewiring.

Unfortunately, the structural features of the building usually provide a hostile environment to radio propagation. Numerous channel measurements [31]-[50] have revealed that one of the most important characteristics of the indoor channel is multipath propagation. In such a channel, a transmitted signal reflects back and forth between various objects, e.g. walls, doors, floor, ceiling, partitions, etc., giving rise to a received signal that is a composite of several paths. In general, each path arrives at the receiver at a slightly different time from one another, resulting in a spread of the signal in time commonly known as *multipath delay spread.* The spread of a signal can vary widely from

building to building, depending upon the shape, size, floor plan, and interior design of the building [34], [37], [40]-[42]. It may also vary with the radio frequency [38], [42] and the type of receiving antenna [50] being used.

In a communication system where the channel is corrupted by the multipath delay spread, a transmitted signal does not only arrive at the receiver within one symbol period, but its delayed components will also arrive during the subsequent intervals. Clearly, the delayed components will interfere with the succeeding symbols, and may cause a detection error. This type of interference is usually called *intersymbol interference* (ISI). The number of succeeding symbols which might be interfered by the ISI depends on the length of the delay spread and the duration of the symbols themselves. The longer the delay is and/or the shorter the symbol period becomes, the larger the number of interfered symbols are.

Since the mid 1980s, a series of performance analyses for indoor wireless communication systems have been conducted. The analyses focused on both the spread spectrum techniques [51]-[58] and standard modulation schemes [59]-[62]. The direct-sequence and the hybrid direct-sequence/frequency-hopped systems were considered in [51]-[55] and [56] respectively, whereas the frequency-hopping technique was studied in [57] and [58]. In [51]-[57], the indoor channel model suggested by Kavehrad [51] was exploited. This model is assumed to have a fixed number of propagation paths with equal gains, and path delays that are uniformly distributed over a symbol period. Although this model seems to be physically unrealistic, Kavehrad and the others used it for its tractability. In [58], only a single-path propagation model was considered, i.e. the effect of the multipath delay spread was neglected.

The analysis in [59], which examined phase shift keying as a modulation scheme, employed continuous delay spread models which were not obtained from any indoor

measurements. In [60], the differential-phase-shift-keying modulation was studied for indoor Rician fading channels. As in [58], the multipath delay spread was ignored.

In [61] and [62], Valenzuela investigated the performance of quadrature amplitude modulation for indoor communication, using a discrete channel model proposed by Saleh and Valenzuela [33]. This model, which is completely different from that of Kavehrad, is based on actual impulse response measurements taken in an office building. Kavehrad and Ramamurthi [53] also considered this model in their work, but both they and Valenzuela conducted their studies by means of simulation only.

In this chapter, an indoor cellular communication system employing frequency hopping as the multiple access scheme is considered. Saleh and Valenzuela's channel model will be used to evaluate the system performance analytically. It will be seen that the mathematical development is indeed tractable, although the two researchers believe that their channel model is more convenient for use in simulation than in analyses. Moreover, since the model is derived from actual channel measurements, it seems to be more realistic than the one proposed by Kavehrad. Using such a model for the performance prediction would therefore lead to a more accurate result.

In the next section, an explanation of Saleh and Valenzuela's channel model is provided. Then the system operation and the signal model are respectively described in Section 4.3 and 4.4. The performance analysis will be conducted in Section 4.5, followed by the numerical results in Section 4.6 and the summary in Section 4.7.

4.2 Saleh-Valenzuela Channel Model

During the mid 1980s, Saleh and Valenzuela [33] conducted channel measurements in an office building of the AT&T Bell Laboratories. Based on the measurement results, the

researchers developed a statistical model for the indoor multipath channel. Their model appears to fit the measured data very well and more importantly is extendable to other buildings. Saleh and Valenzuela employed the discrete representation of the channel impulse response given by

$$h(t) = \sum_k \beta_k e^{j\theta_k} \delta(t - \tau_k), \tag{4.1}$$

where $\delta(\cdot)$ is the Dirac delta function. β_k is the positive gain of the kth path or ray, τ_k is the propagation delay, and θ_k represents the phase shift. In general, β_k, τ_k, and θ_k are random and vary with time. It is assumed, however, that the rate of their variation is slow in comparison to the signaling rate. Therefore, the parameters are treated as time-invariant random variables.

In [33], it is found that rays generally arrive in clusters. A cluster is formed by a number of rays reflecting back and forth in the vicinity of the receiver and/or the transmitter. The first arriving cluster is usually due to a signal that propagates over an open space, such as a hallway, and passes through only a few walls. The path of such signal is not necessarily a straight line. Subsequent clusters, on the other hand, are normally formed by signals that reflect off the interior structures of the building, such as metal doors and walls.

Saleh and Valenzuela modeled the cluster arrival times (or the arrival times of the first rays of clusters) as a Poisson process having a fixed arrival rate Λ. Also, they modeled the arrival times of subsequent rays within each cluster as a Poisson arrival process with a fixed rate λ. Typically, $\lambda >> \Lambda$ as a cluster consists of several rays.

If we let T_j $(j = 0, 1, 2, \cdots)$ denote the arrival time of the jth cluster, and τ_{kj} $(k = 0, 1, 2, \cdots)$ denote the arrival time of the kth ray of the jth cluster, both T_j and τ_{kj} can be described by independent interarrival exponential probability density functions:

$$p\left(T_j \middle| T_{j-1}\right) = \Lambda \exp\left[-\Lambda\left(T_j - T_{j-1}\right)\right], \quad j > 0, \tag{4.2}$$

$$p\left(\tau_{kj} \middle| \tau_{(k-1)j}\right) = \lambda \exp\left[-\lambda\left(\tau_{kj} - \tau_{(k-1)j}\right)\right], \quad k > 0. \tag{4.3}$$

Note that for the first cluster, $T_0 = 0$, and for the first ray of the jth cluster, $\tau_{0j} = 0$.

The gain of the kth ray of the jth cluster and its phase angle are denoted by β_{kj} and θ_{kj}, respectively. The phase angles $\{\theta_{kj}\}$ are assumed to be statistically independent and uniformly distributed over $[0, 2\pi)$. Whereas, the path gains $\{\beta_{kj}\}$ are found to be Rayleigh distributed with a probability density function (PDF):

$$p\left(\beta_{kj}\right) = \frac{2\beta_{kj}}{\overline{\beta_{kj}^2}} \exp\left[-\frac{\beta_{kj}^2}{\overline{\beta_{kj}^2}}\right], \tag{4.4}$$

where $\overline{\beta_{kj}^2} = E\left[\beta_{kj}^2\right]$ is the mean square of the path gain, or equivalently the average path power gain. It is assumed that all the path gains are identically distributed, but statistically independent of each other and of the phase angles. Moreover, it was found that $\overline{\beta_{kj}^2}$ is a monotonically decreasing function of T_j and τ_{kj}, which is expressed as

$$\overline{\beta_{kj}^2} = \overline{\beta_{00}^2} e^{-T_j/\Gamma} e^{-\tau_{kj}/\eta}, \tag{4.5}$$

where $\overline{\beta_{00}^2}$ is the average power gain of the first ray of the first cluster. Γ and η are power-delay time constants for the clusters and the rays, respectively.

4.3 System Operation

Consider a cellular FH-SSMA system operating on a floor of a building. The system comprises a number of base stations, each communicating with M simultaneous users. The radio spectrum is reused in every cell on the floor. The data modulation scheme is

binary frequency shift keying (BFSK). This scheme is selected for the sake of simplicity, as the analysis focuses on the effect of the delay spread. Furthermore, BFSK tends to outperform non-binary FSK as far as the multiple access interference is concerned [23]. This is due to the fact that, when there is a hit, the probability of correct detection for the BFSK scheme is greater than that for a non-binary FSK scheme.

4.3.1 Transmitter Model

Depicted in Fig. 4.1 is the simplified block diagram of a transmitter employed in the FH-SSMA system under consideration. The forward-error-correction (FEC) encoder receives the data bits at a rate of R_b bit/s and produces the coded bits at a rate of $R_c = R_b/r$ bit/s, where r is the code rate. Each coded bit is then transformed into a BFSK symbol by the modulator. Exiting from the modulator at a rate of R_s ($= R_c$ in this case) symbol/s, each modulated symbol is hopped across the spread-spectrum bandwidth W, with a rate L times faster than the symbol rate itself. As a result, L copies of a symbol (called chips) are transmitted via L hopping frequencies during a symbol period T_s.

As in [63], the hopping patterns are chosen such that no two users in the same cell hop to the same channel at the same time. It is further assumed that the hopping patterns of any two users in different cells are independent of each other.

4.3.2 Receiver Model

The simplified block diagram of a receiver is illustrated in Fig. 4.2. First, the received signals are dehopped with a hopping pattern identical to that used in the transmitter. The demodulator then performs noncoherent detection on L dehopped signals every T_s seconds, and transform them into the corresponding chips. Due to the channel

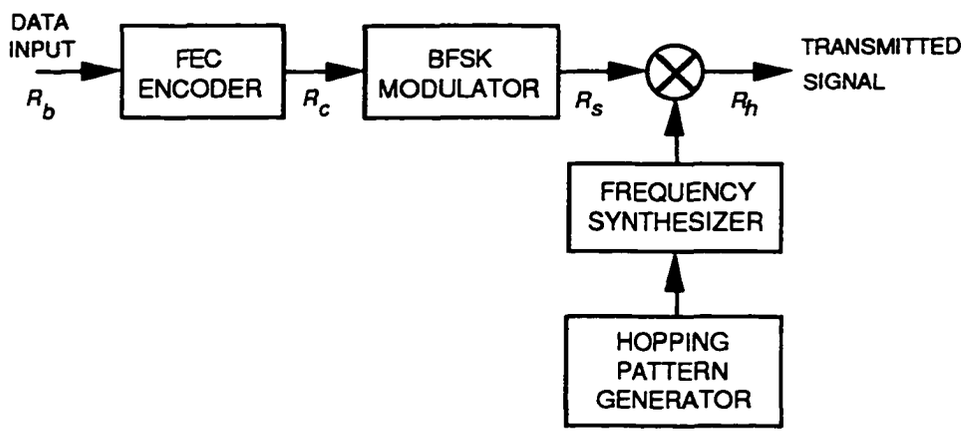

Fig. 4.1. Simplified block diagram of a transmitter for the cellular FH-SSMA system.

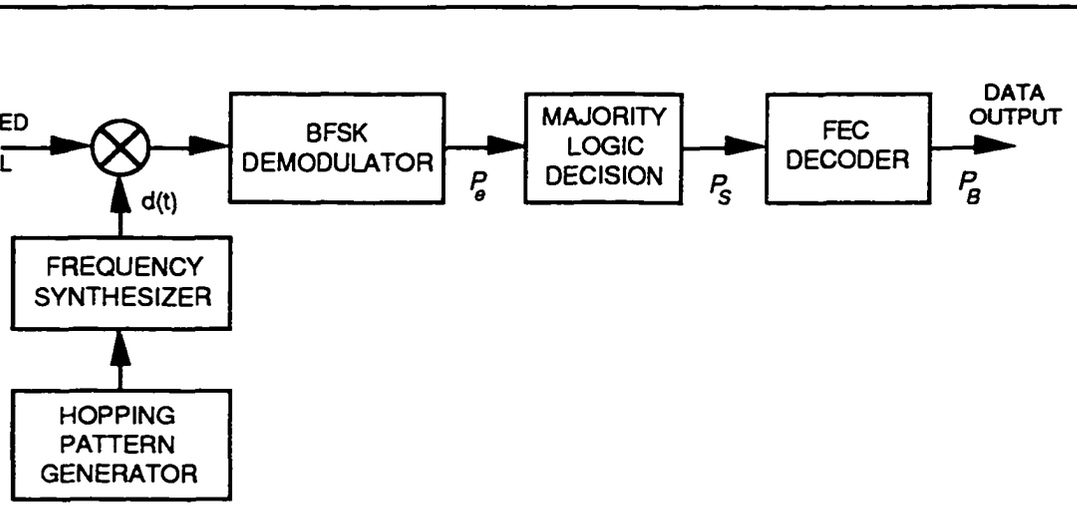

Fig. 4.2. Simplified block diagram of a receiver for the cellular FH-SSMA system.

impairments and multiple access interference, the decision on some of the chips may be in error. Therefore, to determine which symbol was actually transmitted, all L chips are shifted into a majority logic decision device, wherein the symbol corresponding to the majority of the chips is chosen as the correct one. Should a tie occur, an arbitrary decision is made between the tied chips. The FEC decoder then converts the demodulated symbols into message bits.

4.4 Signal Model

Fig. 4.3 illustrates the arrival of a chip that has traversed through an indoor multipath channel. As it leaves the transmitter, a chip has a total duration of T_h seconds. Due to the delays in the propagation paths, the received waveform has an overall duration longer than T_h seconds as shown in the figure.

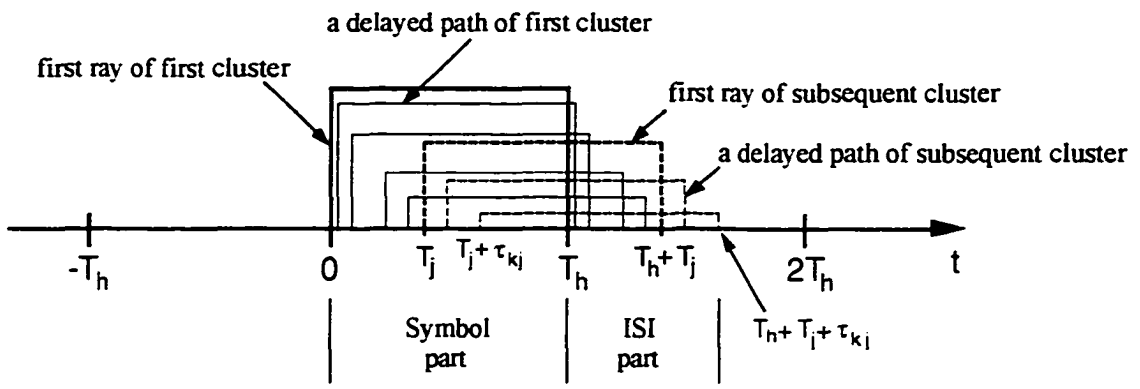

Fig. 4.3. Received signal model

In general, the waveform can be divided into two parts, namely symbol part and ISI part. The symbol part, which covers the interval $[0, T_h]$, comprises of the first ray of the first cluster and the leading portions of subsequent rays and clusters. It is this part of the waveform that the receiver will be synchronized with. The ISI part, on the other hand, consists of the rear portions of the subsequent rays and clusters, and lies beyond T_h. In Figure 4.3, only two clusters are shown for convenience. In reality, the waveform consists of several rays and clusters.

For simplicity, the value of each channel parameter is assumed to be within a certain range where the ISI is caused only by an immediately preceding chip, although the analysis can be extended to include more severe ISI. Based on the channel model introduced in Section 4.2, the received waveform of a chip can be expressed as

$$r(t) = \sum_{j=0}^{\infty} \sum_{k=0}^{\infty} \beta_{kj} \cos\left[2\pi(f_{ni} + f_{si})t + \theta_{kj}\right] p_{T_h}\left(t - iT_h - T_j - \tau_{kj}\right) + N(t), \qquad (4.6)$$

where f_{ni} is the frequency of the nth hopping address, f_{si} ($s = 1$ or 0) represents the BFSK carrier frequency, the subscript i denotes the ith hop interval, $N(t)$ is the AWGN, and $p_{T_h}(t)$ is a rectangular pulse defined as

$$p_{T_h}(t) = \begin{cases} 1 & \text{if } 0 \le t \le T_h \\ 0 & \text{otherwise.} \end{cases} \qquad (4.7)$$

4.5 Performance Analysis

The cell configuration of the FH-SSMA system is depicted in Fig. 4.4. As in [64], each cell is assumed to have an ideal rectangular shape. This configuration seems reasonable for the indoor environments since the superstructures of most buildings are square.

However, the analysis in this chapter is not necessarily restricted to this configuration. It may also be applicable to other cell shapes such as the commonly used hexagonal one.

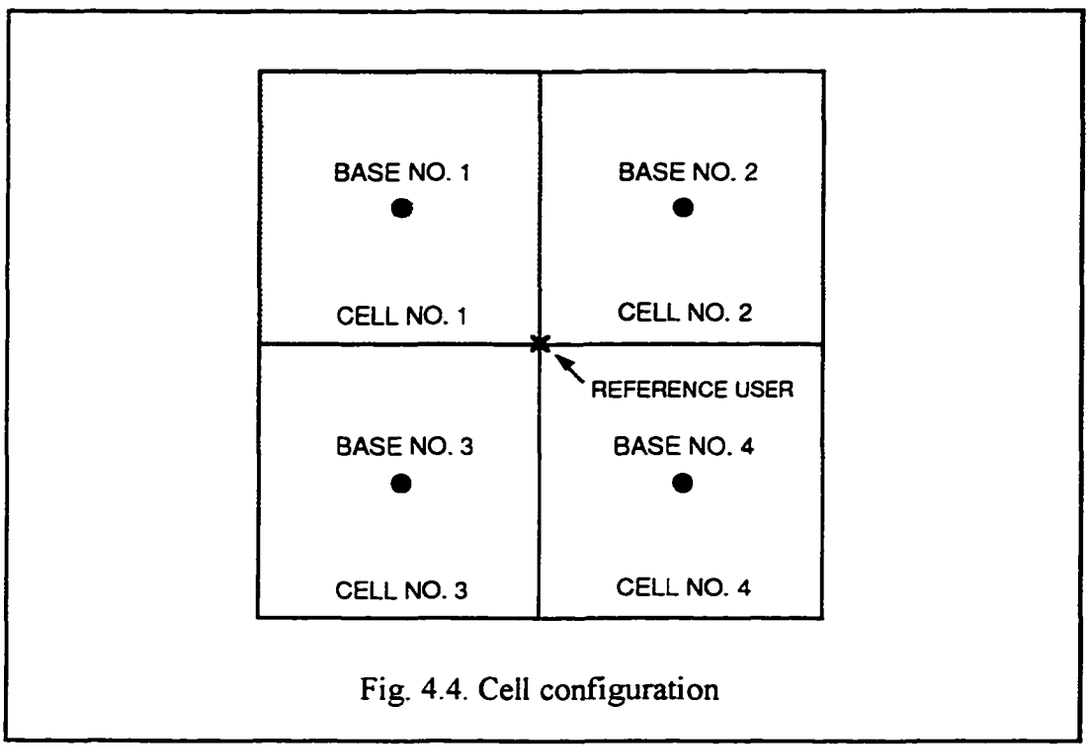

Fig. 4.4. Cell configuration

4.5.1 Probability of Bit Error

In this subsection, the error performance of a user (called reference user) communicating with base station no. 1 (called reference base station) from the intersection of the cells is determined. Clearly, at this location the reference user is far away from each base station at the same distance. It is assumed that the reference user is using an omnidirectional antenna on its transceiver. Also, the propagation path loss between the reference user and the four surrounding base stations is assumed to be equal. Under these circumstances, the reference user will receive signals from all the base stations at an equal power level. This situation is referred to as the worst-case scenario for the downlink.

For the uplink, such scenario would occur in the same manner. If power control is employed and the interfering users are located halfway between the reference base station and their own base stations, the reference base station will receive all the signals (desired and interfering) with equal power. Therefore, in this case, the analysis here will also apply.

To analyze the problem, let us consider an ith hop interval where the nth channel is being occupied by the reference user. It is assumed that the system synchronism is perfectly maintained. According to the hopping strategy mentioned above, the possible hits that the reference user may experience are:

1. A partial hit caused by the ISI part of an intra-cell user who occupied the nth channel during the $(i-1)$th hop interval.

2. Partial hits caused by the ISI parts of inter-cell users who occupied the nth channel during the $(i-1)$th hop interval.

3. Full hits caused by the symbol parts of inter-cell users who currently occupy the nth channel.

When each cell has M users, the probability that the reference user will be hit by at least one of these users (either intra-cell or inter-cell) is

$$\frac{M}{N_h}, \tag{4.8}$$

and the probability that the reference user does not get hit is

$$\frac{N_h - M}{N_h}, \tag{4.9}$$

where $N_h = W/2LR_s$ is the number of hopping channels.

When there is a hit, a detection error can occur at the receiver. Also, the AWGN can cause an error whether or not a hit is present. Therefore, the error probability of the

reference user may be described by a combination of two separate events: the probability of error without any hit and the probability of error with hits. If we assume that a previous hop and a present hop are independent of each other, we may further divide the event of the hits into two disjoint cases: the ISI hits from the $(i-1)$th hop interval and the symbol hits from the ith interval.

Let $\overline{H}$ denotes the event that the reference user does not get hit, xH_I be the event that x ISI hits are present, and yH_S be the event that y symbol hits occur. Then the error probability of the reference user may be expressed as

$$\begin{aligned} P_e = {} & P(e|\overline{H})P(\overline{H}) \\ & + P(e|0H_I, 1H_S)P(0H_I)P(1H_S) + \cdots + P(e|0H_I, yH_S)P(0H_I)P(yH_S) \\ & + P(e|1H_I, 1H_S)P(1H_I)P(1H_S) + \cdots + P(e|1H_I, yH_S)P(1H_I)P(yH_S) \\ & + P(e|2H_I, 1H_S)P(2H_I)P(1H_S) + \cdots + P(e|2H_I, yH_S)P(2H_I)P(yH_S) \\ & \vdots \\ & + P(e|xH_I, 1H_S)P(xH_I)P(1H_S) + \cdots + P(e|xH_I, yH_S)P(xH_I)P(yH_S), \end{aligned} \quad (4.10)$$

where $P(e|\overline{H})$ is the probability of error given there is no hit. $P(\overline{H})$ is the probability of no hit. $P(e|xH_I, yH_S)$ is the probability of error given there are x ISI hits and y symbol hits. $P(xH_I)$ and $P(yH_S)$ are the probability of x ISI hits and y symbol hits, respectively. Note that $P(e|\overline{H})$ is equivalent to $P(e|0H_I, 0H_S)$, and $P(\overline{H})$ is equivalent to $P(0H_I)P(0H_S)$.

To determine $P(xH_I)$ and $P(yH_S)$, let C denote the total number of cells in the system. Since a hopping channel of a cell can be occupied by only one intra-cell user at a time, then the total possible number of ISI hits is equal to C, and the total possible number of symbol hits is $C-1$. Moreover, since the hopping patterns of any two users

in different cells are assumed to be independent, the probability that x out of C ISI hits are present is

$$\left(\frac{M}{N_h}\right)^x\left(\frac{N_h-M}{N_h}\right)^{C-x}, \tag{4.11}$$

and the probability that there are y out of $C-1$ symbol hits is

$$\left(\frac{M}{N_h}\right)^y\left(\frac{N_h-M}{N_h}\right)^{C-1-y}. \tag{4.12}$$

For each particular set of x and y, there are respectively $\binom{C}{x}$ and $\binom{C-1}{y}$ ways in which x and y can be selected from a total of C and $C-1$ hits. Therefore, the probability of x ISI hits, $P(xH_I)$, and y symbol hits, $P(yH_S)$, can be written as

$$P(xH_I)=\left(\frac{M}{N_h}\right)^x\left(\frac{N_h-M}{N_h}\right)^{C-x}\binom{C}{x} \tag{4.13}$$

and

$$P(yH_S)=\left(\frac{M}{N_h}\right)^y\left(\frac{N_h-M}{N_h}\right)^{C-1-y}\binom{C-1}{y}. \tag{4.14}$$

Substituting (4.13) and (4.14) into (4.10), we obtain

$$P_e=\sum_{x=0}^{C}\sum_{y=0}^{C-1}\left(\frac{M}{N_h}\right)^{x+y}\left(\frac{N_h-M}{N_h}\right)^{2C-1-x-y}\binom{C}{x}\binom{C-1}{y}P(e|xH_I,yH_S). \tag{4.15}$$

It should be noted that the presence of $\binom{C}{x}$ and $\binom{C-1}{y}$ in (4.15) implies that $P(e|xH_I,yH_S)$ would remain the same regardless of which cells the x and y hits are from. This is due to the assumptions made earlier.

When the reference user is hit by another user, the hit does not always mean

damage to the reference user. In fact, if the signals from the interfering user and the reference user bear the same symbol, their energy will combine, resulting in a possibly stronger signal. However, if the interfering user is transmitting the opposite symbol, both BFSK bands of the reference user will be filled with energy. This condition may lead to a detection error. To take these two possibilities into account, let w (out of x) and z (out of y) be the number of hits that fall into the same band as the reference user. Then it follows that the number of ways in which w hits can be selected from x ISI hits is $\binom{x}{w}$, and z hits selected from y symbol hits is $\binom{y}{z}$. If we assume that each BFSK symbol is equally likely, the probability of w hits can be written as

$$\left(\frac{1}{2}\right)^{w}\left(\frac{1}{2}\right)^{x-w}\binom{x}{w}, \tag{4.16}$$

and the probability of z hits can be given by

$$\left(\frac{1}{2}\right)^{z}\left(\frac{1}{2}\right)^{y-z}\binom{y}{z}. \tag{4.17}$$

Summing over all possible number of w and z hits, we may express $P\left(e\middle|xH_I, yH_S\right)$ as

$$P\left(e\middle|xH_I, yH_S\right)=\sum_{w=0}^{x}\sum_{z=0}^{y}\left(\frac{1}{2}\right)^{x+y}\binom{x}{w}\binom{y}{z}P\left(e\middle|x, w, y, z\right), \tag{4.18}$$

where $P\left(e\middle|x, w, y, z\right)$ is the conditional probability of error given x ISI hits and y symbol hits with w and z hits occupying the same band as the reference user.

Substituting (4.18) into (4.15), the error probability P_e becomes:

$$P_e=\sum_{x=0}^{C}\sum_{y=0}^{C-1}\sum_{w=0}^{x}\sum_{z=0}^{y}\left(\frac{M}{2N_h}\right)^{x+y}\left(\frac{N_h-M}{N_h}\right)^{2C-1-x-y}\binom{C}{x}\binom{C-1}{y}\binom{x}{w}\binom{y}{z}P\left(e\middle|x, w, y, z\right). \tag{4.19}$$

The expression above is the error probability of a chip at the output of the demodulator (see Fig. 4.2), averaged over all possible combinations of the hits. The symbol error probability, P_S, at the output of the majority logic decision device can be found as follows.

Consider L demodulated chips corresponding to a transmitted symbol. The probability that q out of L chips are detected in error can be described by a binomial distribution:

$$P(q) = \binom{L}{q} P_e^q (1-P_e)^{L-q}. \tag{4.20}$$

If L is odd and $q \geq \lceil L/2 \rceil$, where $\lceil a \rceil$ denotes the smallest integer no less than a, the decision device will choose a wrong symbol with certainty. If L is even, the same is true for $q > L/2$. For $q = L/2$, an incorrect symbol is chosen with probability 1/2. Therefore, P_S may be expressed as

$$P_S = \begin{cases} \displaystyle\sum_{q=\left\lceil \frac{L}{2} \right\rceil}^{L} \binom{L}{q} P_e^q (1-P_e)^{L-q} & \text{for } L \text{ odd} \\ \displaystyle\frac{1}{2}\binom{L}{L/2} P_e^{L/2}(1-P_e)^{L/2} + \sum_{q=\frac{L}{2}+1}^{L} \binom{L}{q} P_e^q (1-P_e)^{L-q} & \text{for } L \text{ even.} \end{cases} \tag{4.21}$$

Finally, to determine the probability of bit error P_B, it is assumed that an (n, k) block code, capable of correcting all combinations of errors up to and including e errors, is employed. Thus, P_B can be approximated by [5, Eqn. 5.46]:

$$P_B \equiv \frac{1}{n} \sum_{i=e+1}^{n} i \binom{n}{i} P_S^i (1-P_S)^{n-i}. \tag{4.22}$$

4.5.2 Evaluation of $P(e|x, w, y, z)$

Within the BFSK demodulator, there are two sets of envelope detectors. One is used to detect symbol "1", while the other is for symbol "0". The outputs of the detectors are sampled every T_h seconds, and then transferred into a decision device, where a hard decision is made.

Let $q_1(i)$ and $q_0(i)$ denote the outputs of the envelope detectors evaluated at the ith hop interval for symbol "1" and symbol "0", respectively. Then, $q_1(i)$ and $q_0(i)$ may be written as [10, Ch. 7]

$$q_1(i) = \sqrt{\left[\int_0^{T_h} r_d(\tau)\cos 2\pi f_1 \tau d\tau\right]^2 + \left[\int_0^{T_h} r_d(\tau)\sin 2\pi f_1 \tau d\tau\right]^2}$$

$$= \sqrt{q_{1c}^2(i) + q_{1s}^2(i)}, \tag{4.23}$$

$$q_0(i) = \sqrt{\left[\int_0^{T_h} r_d(\tau)\cos 2\pi f_0 \tau d\tau\right]^2 + \left[\int_0^{T_h} r_d(\tau)\sin 2\pi f_0 \tau d\tau\right]^2}$$

$$= \sqrt{q_{0c}^2(i) + q_{0s}^2(i)}, \tag{4.24}$$

where $r_d(t) = r(t)d(t)$ is the dehopped signal at the input to the demodulator. $d(t)$ is the dehopping signal generated by the frequency synthesizer:

$$d(t) = 2\cos\left(2\pi f_{ni} t + \varphi\right) p_{T_h}\left(t - iT_h\right), \tag{4.25}$$

where φ is the phase angle introduced by the synthesizer.

Substituting (4.6) and (4.25) into (4.23), the general expression for $q_{1c}(i)$ can be written as [65]

$$q_{1c}(i) = I_s(i) + O_d(i-1) + N_b(i), \tag{4.26}$$

where $I_s(i)$ represents the contributions from symbol parts, $O_d(i-1)$ is the term due to

ISI parts from the $(i-1)$th interval, and $N_b(i)$ is the narrowband noise term.

In order to prevent the loss of orthogonality due to the delayed arrival of clusters and rays from degrading the system performance, a band-pass filter is employed at the front-end of the demodulator. As a result, only the intended dehopped signal will be allowed to pass through.

If we assume that symbol "1" is sent to the reference user, then $I_s(i)$ and $O_d(i-1)$ can be expressed as

$$I_s(i) = \sum_{1+z} \sum_{j=0}^{\infty} \sum_{k=0}^{\infty} \frac{1}{2}\left(T_h - T_j - \tau_{kj}\right)\beta_{kj} \cos\phi_{kj}, \tag{4.27}$$

$$O_d(i-1) = \sum_{w} \sum_{j=0}^{\infty} \sum_{k=0}^{\infty} \frac{1}{2}\left(T_j + \tau_{kj}\right)\beta_{kj} \cos\phi_{kj}, \tag{4.28}$$

where $\phi_{kj} = \theta_{kj} - \varphi$. The summation over $1+z$ represents the reference user's signal plus z symbol hits, while the summation over w denotes the sum of w ISI hits. The expression for $q_{1s}(i)$ may be written in the same format as $q_{1c}(i)$ by replacing $\cos\phi_{kj}$ with $-\sin\phi_{kj}$.

Similarly, $q_{0c}(i)$ in (4.24) can be given by

$$q_{0c}(i) = \sum_{y-z} \sum_{j=0}^{\infty} \sum_{k=0}^{\infty} \frac{1}{2}\left(T_h - T_j - \tau_{kj}\right)\beta_{kj} \cos\phi_{kj} + \sum_{x-w} \sum_{j=0}^{\infty} \sum_{k=0}^{\infty} \frac{1}{2}\left(T_j + \tau_{kj}\right)\beta_{kj} \cos\phi_{kj} + N_b(i), \tag{4.29}$$

where $y-z$ and $x-w$ represent the number of symbol hits and ISI hits carrying symbol "0", respectively.

Recall that the path gains $\{\beta_{kj}\}$ are found to be Rayleigh distributed, with a PDF given by (4.4). If we assume that the phase angles $\{\phi_{kj}\}$ are uniformly distributed over [0, 2π), it can be shown that $\{\beta_{kj}\cos\phi_{kj}\}$ and $\{\beta_{kj}\sin\phi_{kj}\}$ are independent zero-mean

Gaussian random variables (see Appendix C). Therefore, for any given T_j and τ_{kj}, each of the terms in (4.27), (4.28) and (4.29) can be characterized by a zero-mean Gaussian variable. Since all the terms in each of the equations are independent and the narrowband noise term is also Gaussian distributed with zero mean, it can be concluded that $q_{1c}(i)$ and $q_{0c}(i)$ (as well as $q_{1s}(i)$ and $q_{0s}(i)$) are zero-mean Gaussian random variables.

The above discussion in conjunction with (4.23) and (4.24) may be viewed as a classical problem of the narrowband Gaussian process [9], [10]. Thus, $q_1(i)$ and $q_0(i)$ are characterized by the Rayleigh density functions:

$$p(q_1) = \frac{q_1}{\sigma_1^2} \exp\left[-\frac{q_1^2}{2\sigma_1^2}\right], \qquad q_1 \geq 0 \tag{4.30}$$

and

$$p(q_0) = \frac{q_0}{\sigma_0^2} \exp\left[-\frac{q_0^2}{2\sigma_0^2}\right], \qquad q_0 \geq 0 \tag{4.31}$$

where σ_1^2 and σ_0^2 are the variances of $q_1(i)$ and $q_0(i)$, respectively.

Since the random variables in both (4.27) and (4.28) are independent of each other and of $N_b(i)$, σ_1^2 can be expressed as

$$\begin{aligned}
\sigma_1^2 &= E\left\{\left(q_{1c}(i) - E\left\{q_{1c}(i)\right\}\right)^2\right\} \\
&= E\left\{\sum_{l+z} \sum_{j=0}^{\infty} \sum_{k=0}^{\infty} \frac{1}{4}\left(T_h - T_j - \tau_{kj}\right)^2 \beta_{kj}^2 \cos^2 \phi_{kj}\right\} \\
&\quad + E\left\{\sum_{w} \sum_{j=0}^{\infty} \sum_{k=0}^{\infty} \frac{1}{4}\left(T_j + \tau_{kj}\right)^2 \beta_{kj}^2 \cos^2 \phi_{kj}\right\} + E\left\{N_b^2(i)\right\},
\end{aligned} \tag{4.32}$$

where $E\{\cdot\}$ denotes expectation or mean. The last term in (4.32) is the variance of the narrowband noise, which is found to be $N_0 T_h/4$, where N_0 is the one-sided spectral

density of the AWGN [10, Ch. 7].

As it is assumed earlier, all the received signals are identically distributed and the channel parameters are constant throughout the service area. The first expectation in (4.32) will yield $1+z$ identical results, while the second expectation produces w identical results. Therefore, (4.32) can be rewritten as

$$\sigma_1^2 = \frac{1+z}{4} E\left\{ \sum_{j=0}^{\infty} \sum_{k=0}^{\infty} \left(T_h - T_j - \tau_{kj}\right)^2 \beta_{kj}^2 \cos^2 \phi_{kj} \right\}$$

$$+ \frac{w}{4} E\left\{ \sum_{j=0}^{\infty} \sum_{k=0}^{\infty} \left(T_j + \tau_{kj}\right)^2 \beta_{kj}^2 \cos^2 \phi_{kj} \right\} + \frac{N_0 T_h}{4}. \tag{4.33}$$

It is shown in Appendix D that the first expectation in (4.33), which is the variance due to the symbol parts, is given by

$$E\left\{ \sum_{j=0}^{\infty} \sum_{k=0}^{\infty} \left(T_h - T_j - \tau_{kj}\right)^2 \beta_{kj}^2 \cos^2 \phi_{kj} \right\} = \frac{1}{2} \overline{\beta_{00}^2} \left\{ T_h^2 (1+\eta\lambda)(1+\Gamma\Lambda) \right.$$

$$\left. - 2T_h \left[(1+\eta\lambda)\Gamma^2\Lambda + (1+\Gamma\Lambda)\eta^2\lambda \right] + 2\left[(1+\eta\lambda)\Gamma^3\Lambda + (1+\Gamma\Lambda)\eta^3\lambda + \eta^2\lambda\Gamma^2\Lambda \right] \right\}. \tag{4.34}$$

The second expectation, which is due to the ISI parts, is derived in Appendix E to give

$$E\left\{ \sum_{j=0}^{\infty} \sum_{k=0}^{\infty} \left(T_j + \tau_{kj}\right)^2 \beta_{kj}^2 \cos^2 \phi_{kj} \right\} = \frac{1}{2} \overline{\beta_{00}^2} \left\{ (1+\eta\lambda)2\Gamma^3\Lambda + (1+\Gamma\Lambda)2\eta^3\lambda + 2\eta^2\lambda\Gamma^2\Lambda \right\}. \tag{4.35}$$

If we let S denote the total variance of a received signal, it is shown in Appendix F that

$$\overline{\beta_{00}^2} = S\left[\frac{1}{8} T_h^2 (1+\eta\lambda)(1+\Gamma\Lambda) \right]^{-1}. \tag{4.36}$$

Substituting (4.34)-(4.36) into (4.33), we obtain

$$\sigma_1^2 = S\{(1+z)F + wG\} + \frac{N_0 T_h}{4}, \tag{4.37}$$

where

$$F = \left[T_h^2(1+\eta\lambda)(1+\Gamma\Lambda)\right]^{-1}\left\{T_h^2(1+\eta\lambda)(1+\Gamma\Lambda) - 2T_h\left[(1+\eta\lambda)\Gamma^2\Lambda + (1+\Gamma\Lambda)\eta^2\lambda\right]\right.$$
$$\left. +2\left[(1+\eta\lambda)\Gamma^3\Lambda + (1+\Gamma\Lambda)\eta^3\lambda + \eta^2\lambda\Gamma^2\Lambda\right]\right\}, \tag{4.38}$$

and

$$G = \left[T_h^2(1+\eta\lambda)(1+\Gamma\Lambda)\right]^{-1}\left\{(1+\eta\lambda)2\Gamma^3\Lambda + (1+\Gamma\Lambda)2\eta^3\lambda + 2\eta^2\lambda\Gamma^2\Lambda\right\}. \tag{4.39}$$

On the other hand, σ_0^2 in (4.31) may be written as

$$\sigma_0^2 = \frac{y-z}{4}E\left\{\sum_{j=0}^{\infty}\sum_{k=0}^{\infty}\left(T_h - T_j - \tau_{kj}\right)^2\beta_{kj}^2\cos^2\phi_{kj}\right\}$$
$$+\frac{x-w}{4}E\left\{\sum_{j=0}^{\infty}\sum_{k=0}^{\infty}\left(T_j + \tau_{kj}\right)^2\beta_{kj}^2\cos^2\phi_{kj}\right\} + \frac{N_0 T_h}{4}. \tag{4.40}$$

Utilizing the results from Appendix D, E, and F, we have

$$\sigma_0^2 = S\{(y-z)F + (x-w)G\} + \frac{N_0 T_h}{4}. \tag{4.41}$$

Since symbol "1" is sent to the reference user, a decision error will occur if $q_0(i)$ is greater than $q_1(i)$. Thus, the error probability $P(e|x, w, y, z)$ can be given by

$$P(e|x, w, y, z) = \Pr[q_0 > q_1]$$
$$= \int_0^{\infty} p(q_1)\int_{q_1}^{\infty} p(q_0)dq_0 dq_1. \tag{4.42}$$

Substituting (4.30) and (4.31) into (4.42), we obtain

$$P(e|x,w,y,z)=\frac{\sigma_0^2}{\sigma_1^2+\sigma_0^2}$$

$$=\frac{\gamma_0\{(y-z)F+(x-w)G\}+1}{\gamma_0\{(1+y)F+xG\}+2}, \tag{4.43}$$

where γ_0 is the average signal-to-noise ratio defined by

$$\gamma_0=\frac{S}{N_0T_h/4}. \tag{4.44}$$

Note that with the absence of the delay spread (i.e. $\Lambda=\lambda=0$ or $\Gamma=\eta=0$) and the multiple access interference ($y=z=0$), (4.43) reduces to the well-known BER expression for the Rayleigh fading case without delay spread [22, Eqn. 9-5-22]:

$$P(e)=\frac{1}{\gamma_0+2}. \tag{4.45}$$

4.6 Numerical Results and Discussions

Table 4.1 illustrates the maximum number of users which can be supported by each cell for different values of L and selected values of the channel parameters. The number of users is determined at $P_B \le 10^{-3}$ with $C=2$, $\gamma_0=25$ dB, $W=20$ MHz, and $R_s=32$ kbit/s. The FEC is provided by the (23, 12) Golay code, for which $e=3$. It can be observed from the table that the optimum L at which the number of users is maximized is 3. Hence, this value will be used throughout the rest of numerical calculations.

In Fig. 4.5, the number of users M is plotted against the bit error probability P_B with $C=2$, 3, and 4. The SNR γ_0 is chosen to be 25 dB. The allocated bandwidth W is 20 MHz, and the symbol rate R_s is 32 kbit/s. In order to focus on how the system performance is affected by the number of cells in the system, the ISI is ignored in this

TABLE 4.1

Maximum number of users for different values of L
and selected values of the channel parameters.

L	Maximum Number of Users		
	Rayleigh Fading without Delay Spread	$1/\Lambda = 500$ ns $1/\lambda = 50$ ns $\Gamma = 700$ ns $\eta = 300$ ns	$1/\Lambda = 300$ ns $1/\lambda = 5$ ns $\Gamma = 1000$ ns $\eta = 700$ ns
1	36	35	35
3	**41**	**40**	**36**
4	30	28	23
5	37	34	27
6	31	28	19
7	33	29	19
8	29	24	14

figure. From the figure, it can be seen that, with $C = 2$ (one interfering cell), 41 users can be simultaneously supported in each cell at $P_B = 10^{-3}$. Whereas with $C = 3$, M drops to 22 users, and with $C = 4$, $M = 15$. It is obvious that the reduction in the system capacity is somewhat significant, especially for the latter case of $C = 4$. However, had the hexagonal cell pattern been used, there would have been only three cells that intersect at one point. In such a case, only two interfering cells exist. Moreover, if a power control strategy such as that considered in [66] and/or a cell sectorization technique are exploited, the system performance may improve.

Fig. 4.6 illustrates the bit error probability P_B as a function of the number of users M, at various values of cluster power-delay time constant Γ. As in Fig. 4.5, $\gamma_0 = 25$ dB, $W = 20$ MHz, and $R_s = 32$ kbit/s. The number of cells C is chosen to be 2. All the channel parameters other than Γ are fixed and selected to be: $1/\Lambda = 300$ ns, $1/\lambda = 5$ ns, and $\eta = 20$ ns. The curve for the Rayleigh fading case without delay spread (no ISI) is also provided for comparison. From the figure, it can be observed that when $\Gamma \leq 570$ ns, the performance curve is basically identical to that for the non-ISI case. However, as Γ increases, the number of users decreases accordingly. For example, at $\Gamma = 7$ μs, the system capacity reduces from 41 users (non-ISI case) to 12 users at $P_B = 10^{-3}$. This phenomenon is due to the fact that when Γ is high, the subsequent clusters will decay slowly enough to cause the ISI portion of a signal to have a significant amount of power, which can severely interfere with the succeeding symbol.

In Fig. 4.7, the maximum number of users per cell at $P_B \leq 10^{-3}$ is plotted against Γ, with $C = 2$, 3, and 4. The parameters used for this figure are identical to those used for Fig. 4.6. It is observed from the figure that, for $C = 2$, as Γ becomes smaller than 570 ns, the capacity of the system is 41 users, which is the non-ISI capacity shown in Fig. 4.5 and 4.6. On the other hand, as Γ increases to 6.5 μs, the capacity is reduced to 12 users

and remains unchanged as Γ grows larger. Similarly, in the case of $C = 3$, the number of users drops from 22 to the lower bound of 7 as Γ increases from 640 ns to about 6.6 μs. For $C = 4$, the capacity begins to decrease from 15 users as $\Gamma > 680$ ns, and reaches its lowest value at 5 users as $\Gamma \geq 6$ μs. From these observations, it can be noted that the system capacity will not decrease until Γ becomes large enough, and will no longer decrease as Γ grows beyond a certain value.

Fig. 4.8 demonstrates how the number of users in each cell is affected by a change in the cluster arrival rate Λ, with C as a parameter. All the channel parameters (except Λ of course) are fixed and chosen to be: $\Gamma = 2$ μs, $1/\lambda = 5$ ns, and $\eta = 20$ ns. The system parameters are identical to those used for the previous figures. With $C = 2$, as Λ increases from 10^6 to 7×10^6 cluster/s (or equivalently, $1/\Lambda$ decreases from 1 μs to 1/7 μs), the number of users reduces from 34 to 31, and remains at this value as Λ increases further. With $C = 3$, the system capacity is reduced from 19 to 17 users at $\Lambda \geq 4.1 \times 10^6$ cluster/s. Finally, with $C = 4$, the capacity decreases from 13 to 12 users at $\Lambda = 1.4 \times 10^6$ cluster/s. It can be noted from this figure that the system performance is affected by Λ in the same manner as it is by Γ. That is, the capacity decreases from a maximum value to a minimum value within a certain range of the parameter. However, the capacity reduction due to Λ is not as substantial as the reduction due to Γ.

In Fig. 4.9, the number of users at $P_B \leq 10^{-3}$ is plotted against Λ, with Γ taking on values between 300 ns and 3 μs. $1/\lambda$, η, and all the system parameters are the same as those used in Fig. 4.8. The number of cells is chosen to be 2. From the figure, it is observed that, for $\Gamma = 300$ ns, the system capacity decreases from 41 to 40 users. This is equivalent to only a 2.4 percent reduction. However, as Γ becomes larger, the rate of the reduction increases accordingly. For example, at $\Gamma = 2$ μs, the number of users is reduced from 34 to 31, which is an 8.8 percent decrease. Whereas at $\Gamma = 3$ μs, the reduction is as

high as 14.8 percent (from 27 down to 23 users).

Fig. 4.10 shows the maximum number of users at $P_B \leq 10^{-3}$ as a function of the normalized parameter η/Γ. It should be noted that this parameter cannot be larger than unity, since, according to the Saleh-Valenzuela channel model, the rays within a cluster decay faster than the first ray of the next cluster. The system parameters and the other channel parameters are selected as follows: $C = 2$, $\gamma_0 = 25$ dB, $W = 20$ MHz, $R_s = 32$ kbit/s, $1/\Lambda = 300$ ns, and $1/\lambda = 5$ ns. The figure reveals that at a very low value of Γ (for example 100 ns), where the system is still at its maximum capacity (41 users), the increase in η/Γ (or equivalently, the increase in η) does not affect the system capacity. However, as Γ rises, the increase in η will produce a further reduction in the capacity, which has already been reduced by Γ itself. The higher the values of these parameters are, the more severe the reduction becomes.

In Fig. 4.11, the maximum number of users at $P_B \leq 10^{-3}$ is plotted against the ray arrival rate λ, using the same system parameters as in Fig. 4.10. Various combinations of Γ, η, and Λ are used for each curve in the figure. It can be observed that no matter what the values of these parameters are, the variation in λ has only a little or no effect on the system performance.

Finally, in Fig. 4.12 the performance curves of the system operating at $R_s = 16$, 32, and 64 kbit/s are plotted. All the other parameters are fixed and chosen to be: $C = 2$, $\gamma_0 = 25$ dB, $W = 20$ MHz, $\Gamma = 2$ μs, $\eta = 200$ ns, $1/\Lambda = 300$ ns, and $1/\lambda = 5$ ns. It is observed that with $R_s = 16$ kbit/s, the capacity at $P_B \leq 10^{-3}$ is reduced due to the ISI from 83 users to 77 users. This is equivalent to only a 7.2 percent reduction. However, with $R_s = 32$ kbit/s, the decrease is approximately 24 percent. With $R_s = 64$ kbit/s, the reduction is as high as 55 percent. This occurrence is due to the fact that, as R_s increases, the hop duration $T_h = 1/LR_s$ decreases if L is fixed. Under the same multipath

environment (i.e., same channel parameters), the reduction of T_h will result in a longer ISI part, which poses more interference to the succeeding symbol.

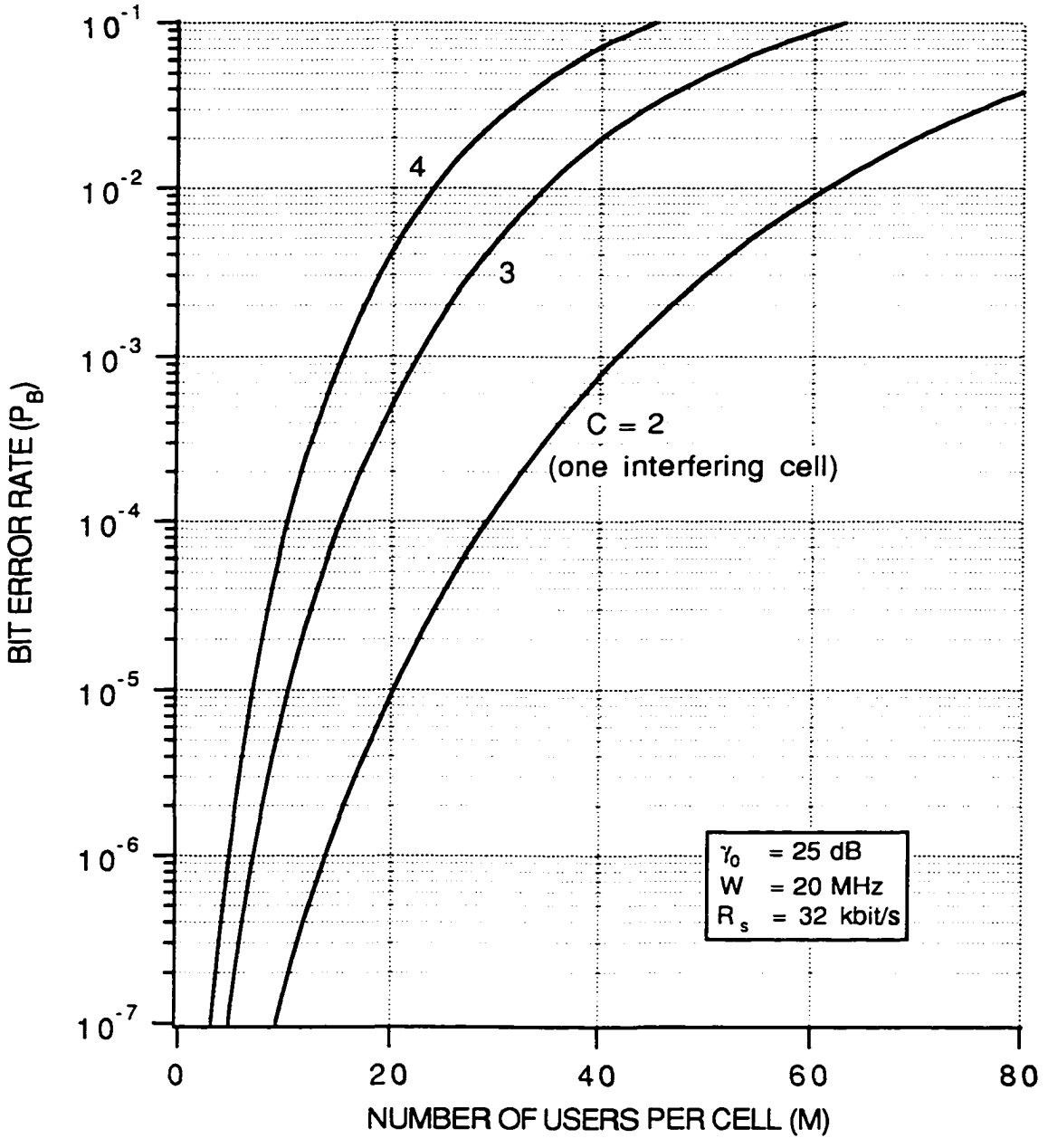

Fig. 4.5. Performance curves of the cellular FH-SSMA system with $C = 2$, 3, and 4. The ISI is ignored. The system parameters are selected as follows: $\gamma_0 = 25$ dB, $W = 20$ MHz, and $R_s = 32$ kbit/s.

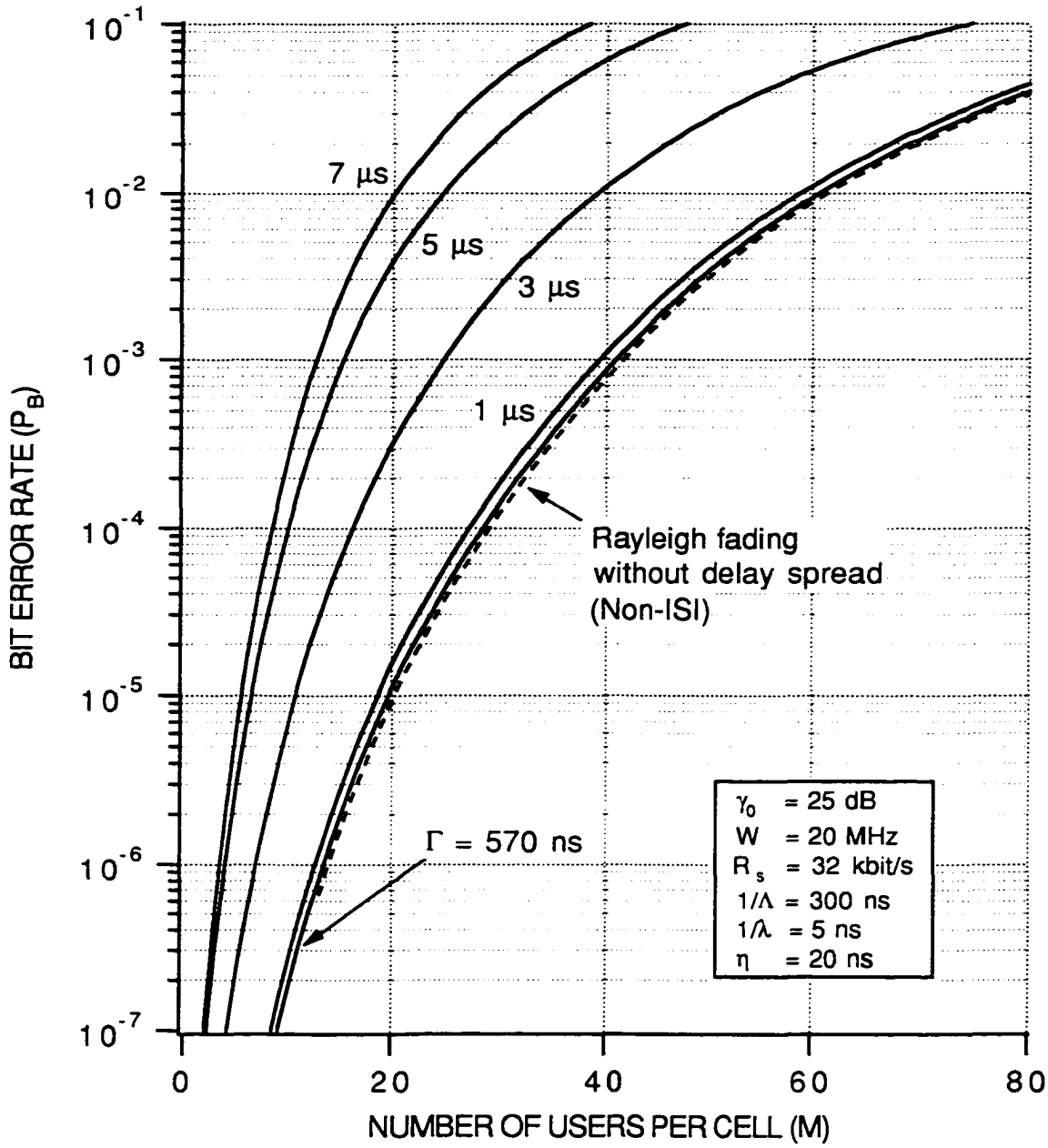

Fig. 4.6. Performance curves of the cellular FH-SSMA system with $C = 2$, and Γ as a parameter. The system and the channel parameters are selected as follows: $\gamma_0 = 25$ dB, $W = 20$ MHz, $R_s = 32$ kbit/s, $1/\Lambda = 300$ ns, $1/\lambda = 5$ ns, and $\eta = 20$ ns.

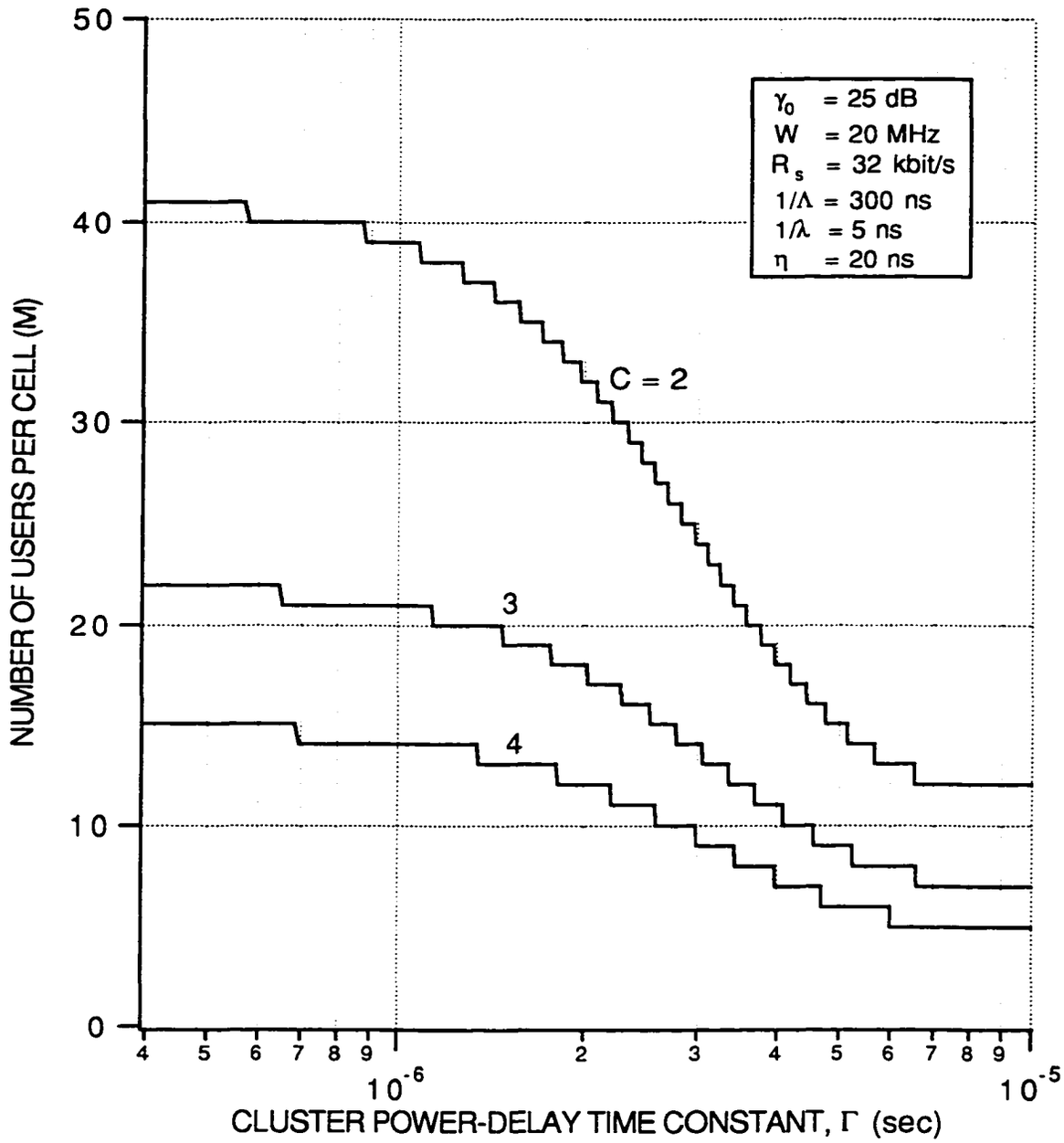

Fig. 4.7. Maximum number of users per cell at $P_B \leq 10^{-3}$ versus the cluster power-delay time constant, Γ. The system and the channel parameters are selected as follows: $\gamma_0 = 25$ dB, $W = 20$ MHz, $R_s = 32$ kbit/s, $1/\Lambda = 300$ ns, $1/\lambda = 5$ ns, and $\eta = 20$ ns.

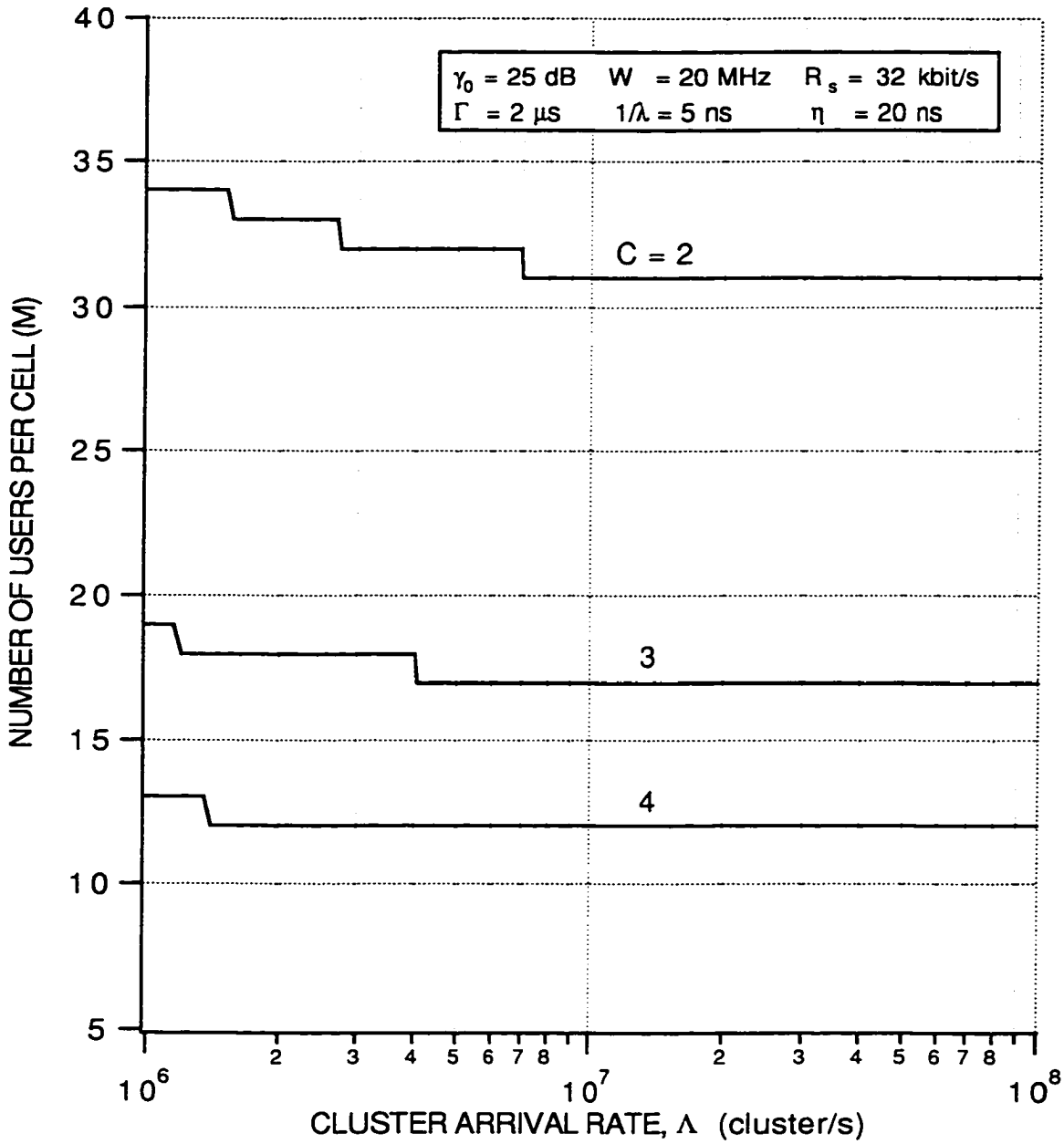

Fig. 4.8. Maximum number of users per cell at $P_B \leq 10^{-3}$ versus the cluster arrival rate, Λ. The system and the channel parameters are selected as follows: $\gamma_0 = 25$ dB, $W = 20$ MHz, $R_s = 32$ kbit/s, $\Gamma = 2$ μs, $1/\lambda = 5$ ns, and $\eta = 20$ ns.

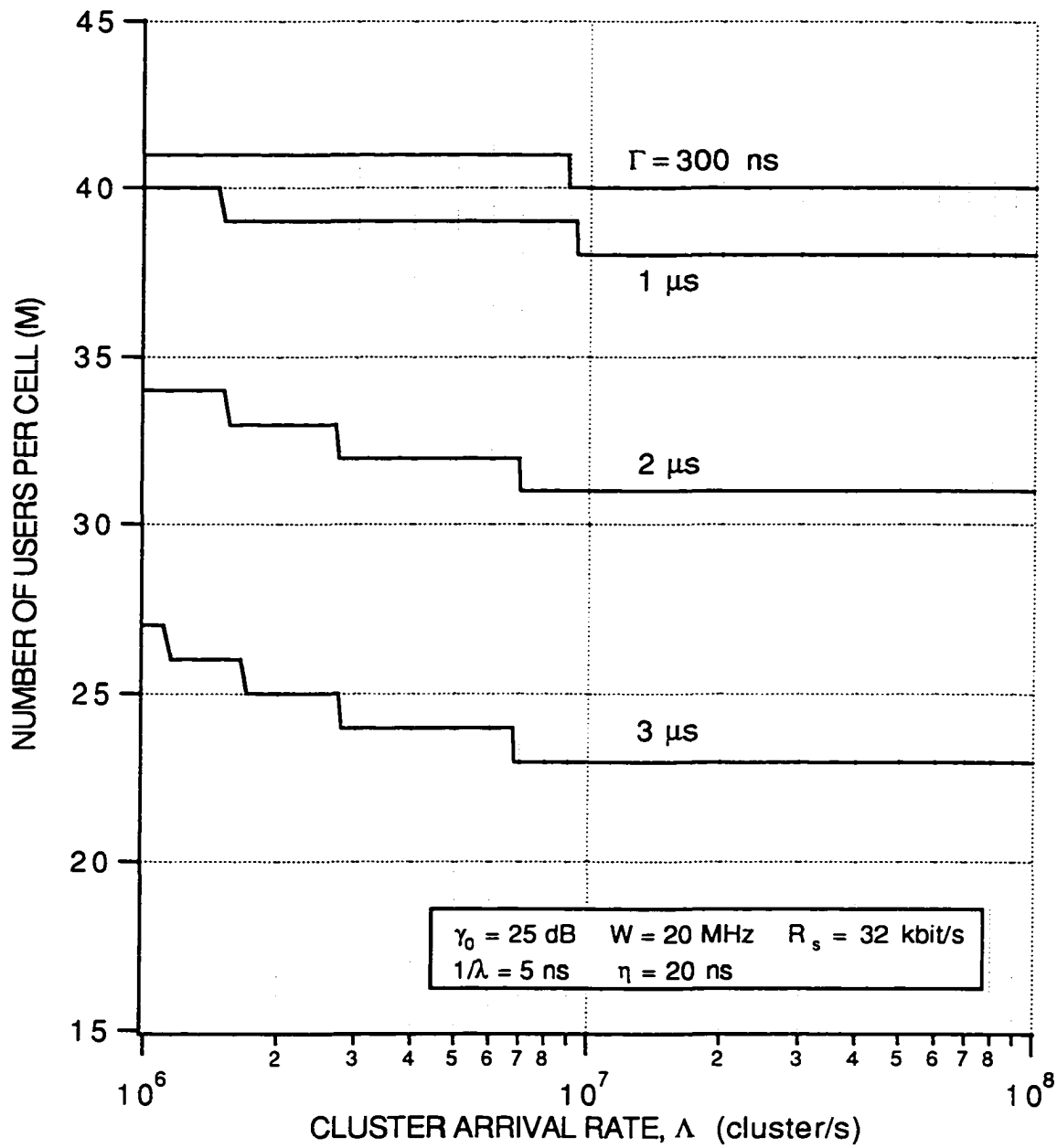

Fig. 4.9. Maximum number of users per cell at $P_B \leq 10^{-3}$ versus the cluster arrival rate, Λ, with Γ =300 ns, 1 μs, 2 μs, and 3 μs. The number of cells is 2. The system and the other channel parameters are selected as follows: $\gamma_0 = 25$ dB, $W = 20$ MHz, $R_s = 32$ kbit/s, $1/\lambda = 5$ ns, and $\eta = 20$ ns.

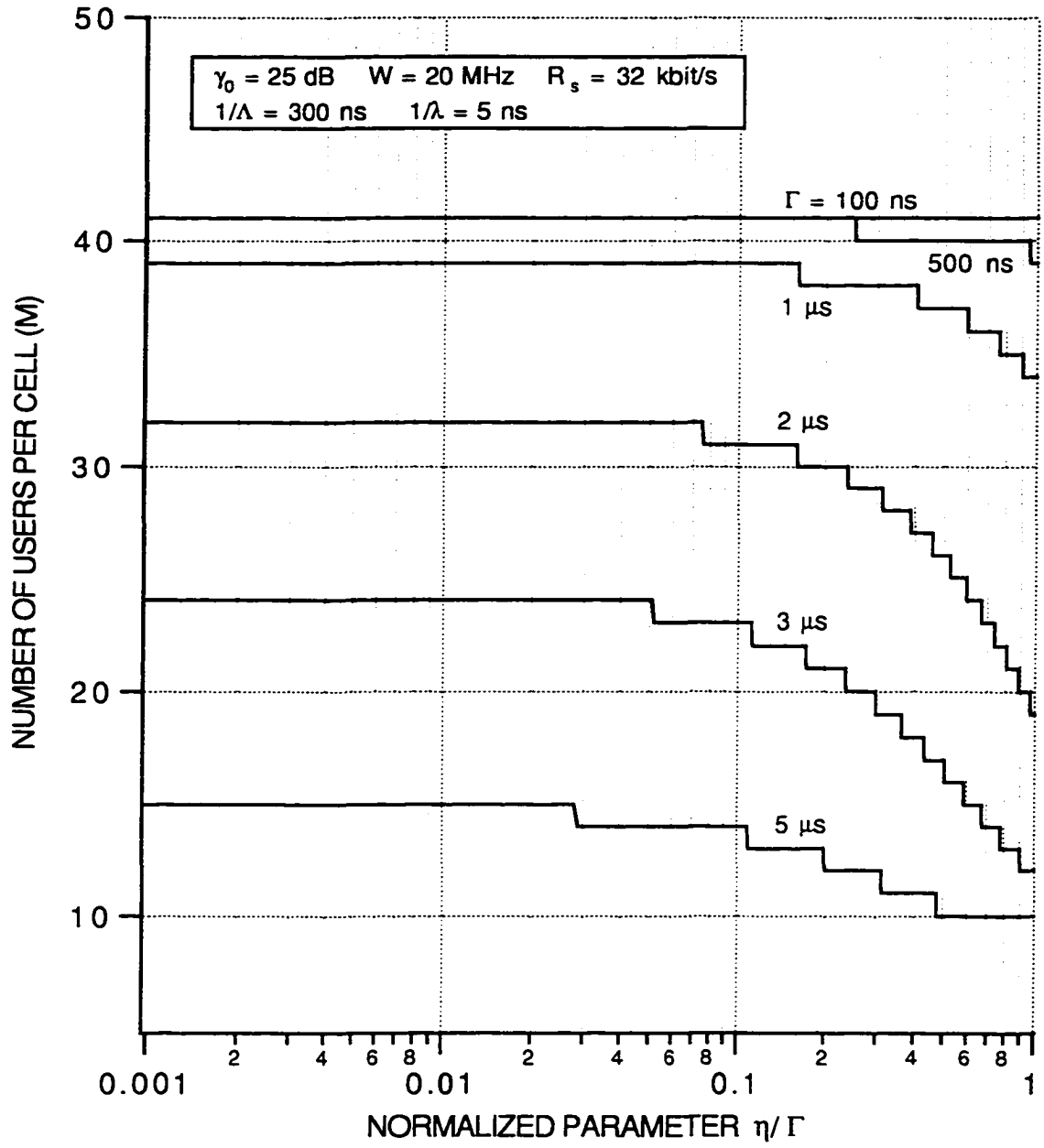

Fig. 4.10. Maximum number of users per cell at $P_B \leq 10^{-3}$ versus the normalized parameter η/Γ, with $\Gamma = 100$ ns, 500 ns, 1 μs, 2 μs, 3 μs, and 5 μs. The number of cells is 2. The system and the other channel parameters are selected as follows: $\gamma_0 = 25$ dB, $W = 20$ MHz, $R_s = 32$ kbit/s, $1/\Lambda = 300$ ns, and $1/\lambda = 5$ ns.

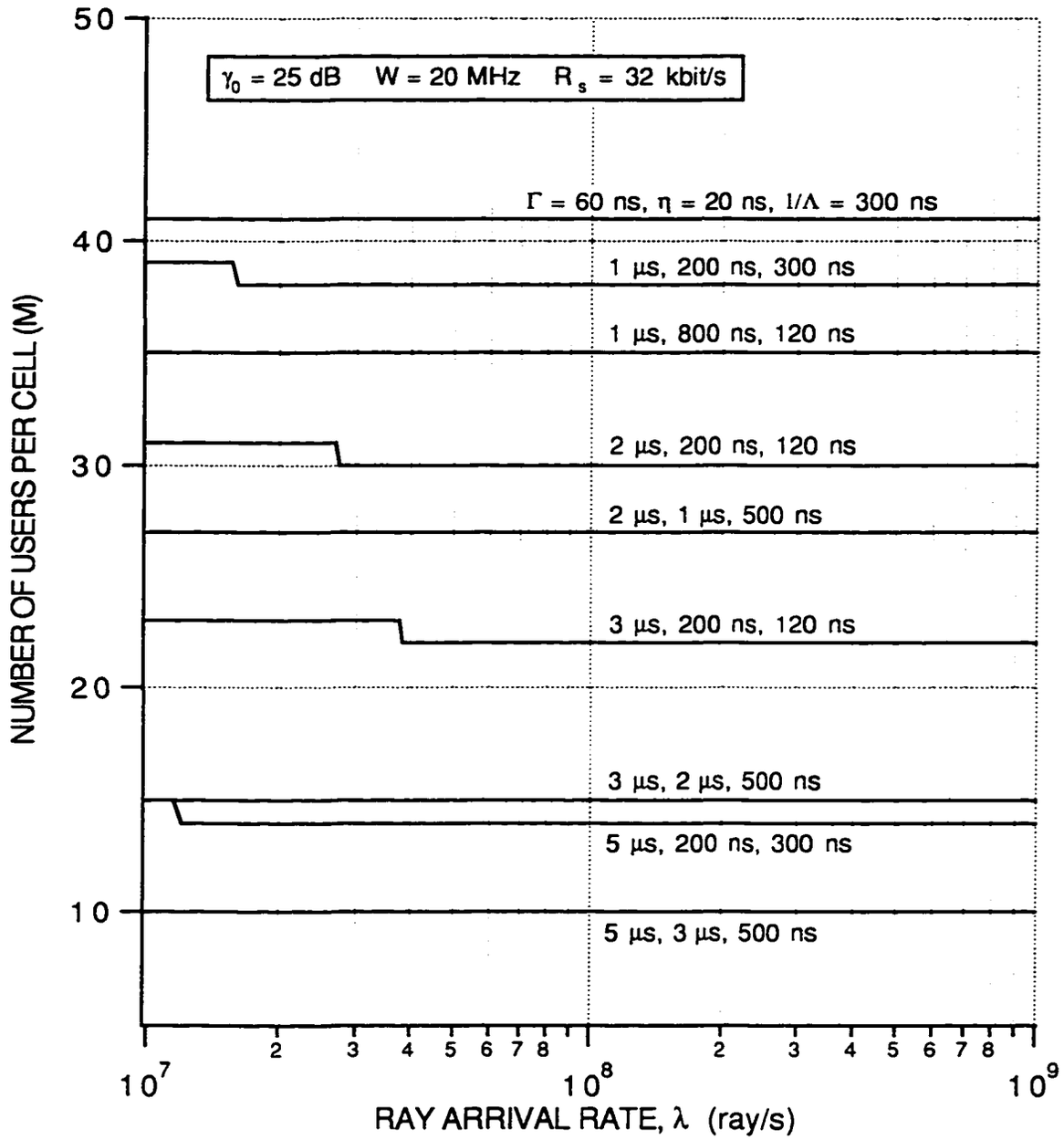

Fig. 4.11. Maximum number of users per cell at $P_B \leq 10^{-3}$ versus the ray arrival rate, λ. The number of cells is 2. The system parameters are selected as follows: $\gamma_0 = 25$ dB, $W = 20$ MHz, and $R_s = 32$ kbit/s.

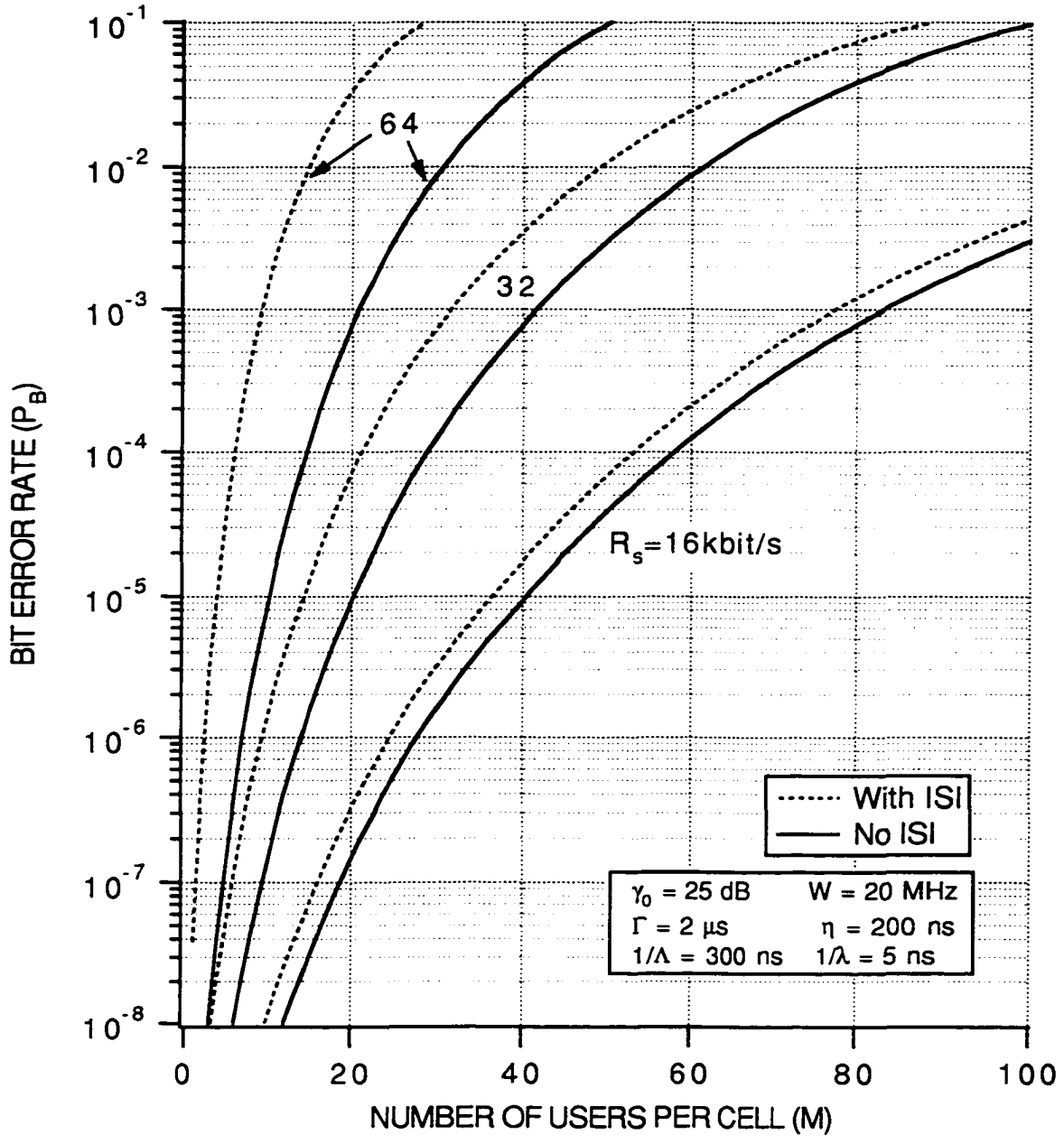

Fig. 4.12. Performance curves of the cellular FH-SSMA system with $C=2$, and R_s as a parameter. The system and the channel parameters are selected as follows: $\gamma_0 = 25$ dB, $W = 20$ MHz, $\Gamma = 2$ μs, $\eta = 200$ ns, $1/\Lambda = 300$ ns, and $1/\lambda = 5$ ns.

4.7 Summary

In this chapter, the effect of time delay spread on the performance of a cellular FH-SSMA system operating in an indoor environment was investigated. Saleh and Valenzuela's channel model which appears to be more realistic than the one suggested by Kavehrad [51] was employed. It was demonstrated that the Saleh-Valenzuela model can well be used in the analysis although it is previously thought to be more convenient for use in simulation.

The influence of the channel parameters on the system performance, which is given in terms of capacity, was illustrated. It was found that the change in the cluster power-delay time constant Γ can greatly affect the number of simultaneous users supported by each cell. The larger Γ gets, the smaller the number of users becomes. However, it was revealed that the capacity will no longer decrease as Γ increases beyond a certain value. The capacity is also affected by the change in the cluster arrival rate Λ in the same manner as it is by Γ. However, the reduction in the number of users is not as substantial.

For η, the results showed that, when Γ is high enough to decrease the capacity, the increase in η will further reduce the capacity significantly. The only parameter that has a little or no effect on the system performance is λ. Finally, it was shown that, with fixed values of the channel parameters, the reduction of the capacity will become more substantial as the transmission rate increases (or equivalently, as the hop interval becomes shorter).

Chapter 5

Conclusions and Future Research

A summary of previous chapters is given in Section 5.1. Suggestions for future research are made in Section 5.2.

5.1 Summary of the Dissertation

In Chapter 2, a brief description of the conventional and Viterbi's frequency-hopped spread-spectrum techniques was provided. It was illustrated that each technique is completely different with respect to the operation. The mathematical models for Rayleigh, Rician, shadowed Rician, and Nakagami fading were also described. Among these models, the Nakagami model appears to be the most versatile, since it represents the entire range of fading, i.e. from one-sided Gaussian to non-fading.

Chapter 3 presented the performance analysis of Viterbi's FH-SSMA system under three different fading scenarios, namely Rician, shadowed Rician, and Nakagami fading. These fading scenarios are found to exist in certain mobile environments. For example, Rician fading can occur in an indoor or an urban microcellular system. Shadowed Rician fading may take place in a land mobile satellite channel. Nakagami fading may be found in an urban mobile environment. The probability of signal deletion for each of

these fading scenarios was derived. The system performance was evaluated in terms of system capacity, using the same parameters considered in a previous work by Goodman *et al.* The results of that work were also compared with the results of Chapter 3.

Throughout the analysis, a data rate of 32 kbit/s and a bandwidth of 20 MHz were used. The number of bits and the number of hops per message symbol were optimized at a required bit error rate of 10^{-3}, and found to be 8 and 19, respectively. For the Rician fading case, a range of the Rician factor (from 2 dB to 10 dB) was considered. It was found that, when the factor is as low as 2 dB, the system capacity is less than the non-fading capacity by only 13 percent, yet 7 percent greater than that for the Rayleigh fading case. However, as the Rician factor increases to 10 dB or more, the system capacity is no longer affected by the fading. Moreover, it was shown that the variation in the capacity due to the change in the SNR will become more substantial as the Rician factor decreases.

In the shadowed Rician fading case, the results for the light, average, and heavy shadowing scenarios were illustrated. The last scenario was shown to have the same effect on the system capacity as the Rayleigh fading case. Whereas the light and the average shadowing scenarios produce only a slight decrease in the capacity (compared to the non-fading case). Finally, for Nakagami fading, the system performance was evaluated with the values of the fading parameter ranging from 0.5 to 2.5. At the worst-case value of 0.5, the system capacity reduces by 37 percent from the Rayleigh fading capacity, and nearly 50 percent from the non-fading capacity. It was also shown that as the SNR drops, the system capacity at a low value of the fading parameter will decrease faster than it would at a higher value of the parameter.

In Chapter 4, a cellular FH-SSMA system in an indoor environment was studied. The channel model developed by Saleh and Valenzuela from their measurement results was used. In this model, the multipath delay spread is characterized by four channel

parameters, namely cluster arrival rate, ray arrival rate, cluster power-delay time constant, and ray power-delay time constant. The performance analysis was exclusively concerned with the worst-case scenario, where the reference user receives all the signals (desired and interfering) with equal power levels. The conventional (fast) FH-SS technique was exploited along with the BFSK modulation. Also, FEC was incorporated into the system. With a symbol rate of 32 kbit/s, a bandwidth of 20 MHz, a signal-to-noise ratio of 25 dB, and the (23, 12) Golay code, the optimum number of hops per symbol was found to be 3.

The performance of the system, given in terms of the number of users per cell, was shown to reduce drastically when the number of adjacent interfering cells increases from one to three. It was also found that the system capacity can substantially decrease due to the increase in the cluster and the ray power-delay time constants. The same is true for the cluster arrival rate except that the reduction in the capacity is not as substantial. The ray arrival rate was found to be the only parameter that has a negligible effect on the system performance.

5.2 Future Research

The performance analysis of Viterbi's FH-SSMA system has completely ignored the Doppler shift. In practice, however, this phenomenon may become evident as a mobile user moves at a relatively high speed. Therefore, further investigation in this subject is recommended.

Multipath delay spread is another issue that has been ignored in the analysis of Viterbi's FH-SSMA system. Since this system can be utilized as well in an environment where multipath delay spread is prominent, a further study in this matter is also suggested.

The analysis of Viterbi's FH-SSMA system was concerned with three fading scenarios, which are found in certain mobile environments. In some cases, experiment data may be best described by a shadowed Nakagami distribution. A study on this fading model is also worth pursuing.

In the analysis of the cellular FH-SSMA system in an indoor environment, the outputs of the envelope detectors are sampled every T_h seconds, which means the detection window has a duration of one chip interval. A further investigation on how a detection window with a different duration would effect the system performance is worth trying.

It is shown in [66] that the performance of a cellular FH-SSMA system employing Viterbi's technique can be enhanced by a downlink power control strategy. It would be interesting to examine how much improvement this strategy can offer to the cellular system considered in this dissertation.

In some indoor environments, the channel conditions can be so poor that more than one succeeding chips are interfered by the ISI. This situation is worth a study as well.

Bibliography

[1] A. J. Viterbi, "A processing satellite transponder for multiple access by low-rate mobile users," in *Proceedings of Fourth International Conference on Digital Satellite Communications*, Montreal, Canada, Oct. 23-25, 1978, pp. 166-174.

[2] G. R. Cooper and R. W. Nettleton, "A spread-spectrum technique for high-capacity mobile communications," *IEEE Transactions on Vehicular Technology*, vol. VT-27, pp. 264-275, Nov. 1978.

[3] K. S. Gilhousen, I. M. Jacobs, R. Padovani, and L. A. Weaver, "Increased capacity using CDMA for mobile satellite communication," *IEEE Journal on Selected Areas in Communications*, vol. 8, pp. 503-514, May 1990.

[4] K. S. Gilhousen, I. M. Jacobs, R. Padovani, A. J. Viterbi, L. A. Weaver, and C. E. Wheatley, "On the capacity of a cellular CDMA system," *IEEE Transactions on Vehicular Technology*, vol. 40, pp. 303-312, May 1991.

[5] B. Sklar, *Digital Communications Fundamentals and Applications*. Englewood Cliffs, New Jersey: Prentice Hall, 1988.

[6] M. K. Simon, J. K. Omura, R. A. Scholtz, and B. K. Levitt, *Spread Spectrum Communications*. Rockville, MA: Computer Science Press, 1985.

[7] D. J. Goodman, P. S. Henry, and V. K. Prabhu, "Frequency-hopped multilevel FSK for mobile radio," *Bell System Technical Journal*, vol. 59, pp. 1257-1275, Sept. 1980.

[8] R. H. Muammar, "Degradation in FH-MFSK mobile radio system capacity due to Rayleigh fading and log-normal shadowing," *IEEE Transactions on Vehicular Technology*, vol. 37, pp. 130-134, Aug. 1988.

[9] P. Beckmann, *Probability in Communication Engineering*. New York, New York: Harcourt, Brace & World, 1967.

[10] A. D. Whalen, *Detection of Signals in Noise*. New York, New York: Academic Press, 1971.

[11] P. J. Crepeau, "Uncoded and coded performance of MFSK and DPSK in Nakagami fading channels," *IEEE Transactions on Communications*, vol. 40, pp. 487-493, Mar. 1992.

[12] C. Loo, "A statistical model for a land mobile satellite link," *IEEE Transactions on Vehicular Technology*, vol. VT-34, pp. 122-127, Aug. 1985.

[13] M. Nakagami, "The *m*-distribution-A general formula of intensity distribution of fading," in *Statistical Methods in Radio Wave Propagation*, W. C. Hoffman, Ed. London, UK: Pergamon, 1960.

[14] H. Suzuki, "A statistical model for urban radio propagation," *IEEE Transactions on Communications*, vol. COM-25, pp. 673-680, July 1977.

[15] Sa. Basu, E. M. MacKenzie, Su. Basu, E. Costa, P. F. Fougere, H. C. Carlson, and H. E. Whitney, "250 MHz/GHz scintillation parameters in the equatorial, polar, and auroral environments," *IEEE Journal on Selected Areas in Communications*, vol. SAC-5, pp. 102-115, Feb. 1987.

[16] G. Einarsson, "Address assignment for a time-frequency-coded, spread-spectrum system," *Bell System Technical Journal*, vol. 59, pp. 1241-1255, Sept. 1980.

[17] U. Timor, "Improved decoding scheme for frequency-hopped multilevel FSK system," *Bell System Technical Journal*, vol. 59, pp. 1839-1855, Dec. 1980.

[18] T. S. Rappaport and C. D. McGillem, "UHF Fading in Factories," *IEEE Journal on Selected Areas in Communications*, vol. 7, pp. 40-48, Jan. 1989.

[19] R. J. C. Bultitude and G. K. Bedal, "Propagation characteristics on microcellular urban mobile radio channels at 910 MHz," *IEEE Journal on Selected Areas in Communications*, vol. 7, pp. 31-39, Jan. 1989.

[20] T. Y. Yan and C. C. Wang, "Mathematical models for cochannel interference in FH/MFSK multiple-access systems," *IEEE Transactions on Communications*, vol. COM-32, pp. 670-678, June 1984.

[21] P. Belezinis and L. F. Turner, "Performance of time-frequency coded spread spectrum systems operating over noisy fading channels," *IEE Proceedings*, vol. 135, pt. F, pp. 513-519, Dec. 1988.

[22] M. Schwartz, W. R. Bennett and S. Stein, *Communications Systems and Techniques*. New York: McGraw-Hill, 1966, chs. 7 and 9.

[23] M. A. Wickert and R. L. Turcotte, "Probability of error analysis for FHSS/CDMA communications in the presence of fading," *IEEE Journal on Selected Areas in Communications*, vol. 10, pp. 523-534, Apr. 1992.

[24] C. Loo, "Digital transmission through a land mobile satellite channel," *IEEE Transactions on Communications*, vol. 38, pp. 693-697, May 1990.

[25] S. Parl, "A new method of calculating the generalized Q function," *IEEE Transactions on Information Theory*, vol. IT-26, pp. 121-124, Jan. 1980.

[26] R. D. J. van Nee, H. S. Misser, and R. Prasad, "Direct-sequence spread spectrum in a shadowed Rician fading land-mobile satellite channel," *IEEE Journal on Selected Areas in Communications*, vol. 10, pp. 350-357, Feb. 1992.

[27] C. Tellambura, Q. Wang, and V. K. Bhargava, "Performance of trellis coded modulation schemes on shadowed mobile satellite communication channels," *IEEE Transactions on Vehicular Technology*, vol. 43, pp. 128-139, Feb. 1994.

[28] R. Esposito, "Error Probabilities for the Nakagami Channel," *IEEE Transactions on Information Theory*, vol. IT-13, pp. 145-148, Jan. 1967.

[29] A. Erdélyi, W. Magnus, F. Oberhettinger, and F. G. Tricomi, *Higher Transcendental Functions, vol. II.* New York, NY: McGraw-Hill, 1953.

[30] L. J. Slater, *Confluent Hypergeometric Functions*. Cambridge, England: University Press, 1960.

[31] D. M. J. Devasirvatham, "The delay spread measurements of wideband radio signals within a building," *Electronics Letters*, vol. 20, pp. 950-951, Nov. 1984.

[32] D. M. J. Devasirvatham, "Time delay spread and signal level measurements of 850 MHz radio waves in building environments," *IEEE Transactions on Antennas and Propagation*, vol. AP-34, pp. 1300-1305, Nov. 1986.

[33] A. A. M. Saleh and R. A. Valenzuela, "A statistical model for indoor multipath propagation," *IEEE Journal on Selected Areas in Communications*, vol. SAC-5, pp. 128-137, Feb. 1987.

[34] D. M. J. Devasirvatham, "A comparison of time delay spread and signal level measurements within two dissimilar office buildings," *IEEE Transactions on Antennas and Propagation*, vol. AP-35, pp. 319-324, Mar. 1987.

[35] D. M. J. Devasirvatham, "Multipath time delay jitter measured at 850 MHz in the portable radio environment," *IEEE Journal on Selected Areas in Communications*, vol. SAC-5, pp. 855-861, June 1987.

[36] R. J. C. Bultitude, "Measurement, characterization and modeling of indoor 800/900 MHz radio channels for digital communications," *IEEE Communications Magazine*, vol. 25, pp. 5-12, June 1987.

[37] T. S. Rappaport and C. D. McGillem, "Characterising the UHF factory radio channel," *Electronics Letters*, vol. 23, pp. 1015-1017, Sept. 1987.

[38] R. J. C. Bultitude, S. A. Mahmoud, and W. A. Sullivan, "A comparison of indoor propagation characteristics at 910 MHz and 1.75 GHz," *IEEE Journal on Selected Areas in Communications*, vol. 7, pp. 20-30, Jan. 1989.

[39] D. M. J. Devasirvatham, R. R. Murray, and C. Banerjee, "Time delay spread measurements at 850 MHz and 1.7 GHz inside a metropolitan office building," *Electronics Letters*, vol. 25, pp. 194-196, Feb. 1989.

[40] K. Pahlavan, R. Ganesh, and T. Hotaling, "Multipath propagation measurements on manufacturing floors at 910 MHz," *Electronics Letters*, vol. 25, pp. 225-227, Feb. 1989.

[41] T. S. Rappaport, "Characterization of UHF multipath radio channels in factory buildings," *IEEE Transactions on Antennas and Propagation*, vol. 37, pp. 1058-1069, Aug. 1989.

[42] D. M. J. Devasirvatham, M. J. Krain, D. A. Rappaport, and C. Banerjee, "Radio propagation measurements at 850 MHz, 1.7 GHz and 4 GHz inside two dissimilar office buildings," *Electronics Letters*, vol. 26, pp. 445-447, Mar. 1990.

[43] T. S. Rappaport, S. Y. Seidel, and K. Takamizawa, "Statistical channel impulse response models for factory and open plan building radio communication system design," *IEEE Transactions on Communications*, vol. 39, pp. 794-807, May 1991.

[44] D. M. J. Devasirvatham, C. Banerjee, R. R. Murray, and D. A. Rappaport, "Four-frequency radiowave propagation measurements of the indoor environment in a large metropolitan commercial building," in *Proceedings of IEEE GLOBECOM*, Dec. 1991.

[45] S. J. Howard and K. Pahlavan, "Autoregressive modeling of wide-band indoor radio propagation," *IEEE Transactions on Communications*, vol. 40, pp. 1540-1552, Sept. 1992.

[46] H. Hashemi, "Impulse response modeling of indoor radio propagation channels," *IEEE Journal on Selected Areas in Communications*, vol. 11, pp. 967-978, Sept. 1993.

[47] S. Y. Seidel and T. S. Rappaport, "Site-specific propagation prediction for wireless in-building personal communication system design," *IEEE Transactions on Vehicular Technology*, vol. 43, pp. 879-891, Nov. 1994.

[48] L. Dossi, G. Tartara, and F. Tallone, "Statistical analysis of measured impulse response functions of 2.0 GHz indoor radio channel," *IEEE Journal on Selected Areas in Communications*, vol. 14, pp. 405-410, Apr. 1996.

[49] L. Talbi and G. Y. Delisle, "Experimental characterization of EHF multipath indoor radio channels," *IEEE Journal on Selected Areas in Communications*, vol. 14, pp. 431-440, Apr. 1996.

[50] T. Manabe, Y. Miura, and T. Ihara, "Effects of antenna directivity and polarization on indoor multipath propagation characteristics at 60 GHz," *IEEE Journal on Selected Areas in Communications*, vol. 14, pp. 441-448, Apr. 1996.

[51] M. Kavehrad, "Performance of nondiversity receivers for spread spectrum in indoor wireless communications," *AT&T Technical Journal*, vol. 64, pp. 1181-1210, July-Aug. 1985.

[52] M. Kavehrad and P. J. McLane, "Performance of low-complexity channel coding and diversity for spread spectrum in indoor, wireless communication," *AT&T Technical Journal*, vol. 64, pp. 1927-1965, Oct. 1985.

[53] M. Kavehrad and B. Ramamurthi, "Direct-sequence spread spectrum with DPSK modulation and diversity for indoor wireless communications," *IEEE Transactions on Communications*, vol. COM-35, pp. 224-236, Feb. 1987.

[54] K. Pahlavan and M. Chase, "Spread-spectrum multiple-access performance of orthogonal codes for indoor radio communications," *IEEE Transactions on Communications*, vol. 38, pp. 574-577, May 1990.

[55] J. Wang, M. Moeneclaey, and L. B. Milstein, "DS-CDMA with predetection diversity for indoor radio communications," *IEEE Transactions on Communications*, vol. 42, pp. 1929-1938, Feb./Mar./Apr. 1994.

[56] J. Wang and M. Moeneclaey, "Hybrid DS/SFH spread-spectrum multiple access with predetection diversity and coding for indoor radio," *IEEE Journal on Selected Areas in Communications*, vol. 10, pp. 705-713, May 1992.

[57] J. Wang and M. Moeneclaey, "Multiple hops/symbol FFH-SSMA with MFSK modulation and Reed-Solomon coding for indoor radio," *IEEE Transactions on Communications*, vol. 41, pp. 793-801, May 1993.

[58] P. Yegani and C. D. McGillem, "FH-MFSK multiple-access communications systems performance in the factory environment," *IEEE Transactions on Vehicular Technology*, vol. 42, pp. 148-155, May. 1993.

[59] J. H. Winters and Y. S. Yeh, "On the performance of wideband digital radio transmission within buildings using diversity," in *Proceedings of IEEE GLOBECOM*, Dec. 1985.

[60] J. A. Roberts and J. M. Bargallo, "DPSK performance for indoor wireless Rician fading channels," *IEEE Transactions on Communications*, vol. 42, pp. 592-596, Feb./Mar./Apr. 1994.

[61] R. A. Valenzuela, "Performance of quadrature amplitude modulation for indoor radio communications," *IEEE Transactions on Communications*, vol. COM-35, pp. 1236-1238, Nov. 1987.

[62] R. A. Valenzuela, "Performance of adaptive equalization for indoor radio communications," *IEEE Transactions on Communications*, vol. 37, pp. 291-293, Mar. 1989.

[63] Z. Al-Etaibi, J. Aldis, and S. Barton, "Co-channel interference in cellular radio systems using frequency hopping code division multiple access (FH-CDMA)," *Wireless Personal Communications*, vol. 1, pp. 291-301, 1994/95.

[64] L. B. Milstein, T. S. Rappaport, and R. Barghouti, "Performance evaluation for cellular CDMA," *IEEE Journal on Selected Areas in Communications*, vol. 10, pp. 680-689, May 1992.

[65] X. D. Wang and M. Lecours, "The effect of delay spread on a FH-FSK spread spectrum mobile radio system over frequency-selective fading channels," *IEEE Transactions on Communications*, vol. 42, pp. 1312-1324, Feb./Mar./Apr. 1994.

[66] R. Viswanathan and S. C. Gupta, "Adjacent cell interference in FH-MFSK cellular mobile radio system," *IEEE Transactions on Vehicular Technology*, vol. VT-32, pp. 191-200, May 1983.

[67] W. H. Beyer, *CRC Standard Mathematical Tables, 27th Edition*. Boca Raton, Florida: CRC Press, 1984.

Appendix A

Derivation of Equation (3.32)

In this appendix, (3.32) is derived, using a procedure similar to that presented in [28]. First, substitute into (3.31) the series expansion [29, p. 5]:

$$I_0(z) = \sum_{k=0}^{\infty} \frac{\left(\frac{z}{2}\right)^{2k}}{k!\Gamma(k+1)}$$

and then rearrange the order of integration to give

$$P_D = \int_0^{b_0} \frac{m^m x}{\Gamma(m)\gamma_0^m} \exp\left[-\frac{x^2}{2}\right] \sum_{k=0}^{\infty} \frac{x^{2k}}{2^k k!\Gamma(k+1)} \int_0^{\infty} \gamma^{k+m-1} \exp\left[-\frac{(m+\gamma_0)\gamma}{\gamma_0}\right] d\gamma dx. \tag{A.1}$$

With a simple change of variable and by using the definition of the gamma function:

$$\Gamma(z) = \int_0^{\infty} e^{-t} t^{z-1} dt,$$

the integral with respect to γ in (A.1) can be written as

$$\int_0^{\infty} \gamma^{k+m-1} \exp\left[-\frac{(m+\gamma_0)\gamma}{\gamma_0}\right] d\gamma = \Gamma(k+m)\left(\frac{\gamma_0}{m+\gamma_0}\right)^{k+m}. \tag{A.2}$$

Substituting (A.2) into (A.1), we obtain

$$P_D = \int_0^{b_0} \left(\frac{m}{m+\gamma_0}\right)^m \frac{x}{\Gamma(m)} \exp\left[-\frac{x^2}{2}\right] \sum_{k=0}^{\infty} \frac{x^{2k}\Gamma(k+m)}{2^k k!\Gamma(k+1)} \left(\frac{\gamma_0}{m+\gamma_0}\right)^k dx. \qquad \text{(A.3)}$$

Utilizing the formulas:

$$\Gamma(k+m) = (m)_k \Gamma(m), \quad \Gamma(k+1) = (1)_k,$$

and the definition of the confluent hypergeometric function given by (3.33), we may express (A.3) as

$$P_D = \left(\frac{m}{m+\gamma_0}\right)^m \int_0^{b_0} x \exp\left[-\frac{x^2}{2}\right] {}_1F_1\left(m;\ 1;\ \frac{x^2\gamma_0}{2(m+\gamma_0)}\right) dx. \qquad \text{(A.4)}$$

Next, apply to (A.4) one of the multiplication theorems for ${}_1F_1(a;\ b;\ z)$ [30, Eqn. 2.3.17]:

$${}_1F_1(a;\ b;\ zw) = w^{-a} \sum_{n=0}^{\infty} \frac{(a)_n (w-1)^n}{n! w^n} {}_1F_1(a+n;\ b;\ z) \qquad \text{(A.5)}$$

and perform a change of variable $y = x^2/2$ to give

$$P_D = \left(\frac{m}{\gamma_0}\right)^m \sum_{k=0}^{\infty} \frac{(m)_k}{k!} \left(1 - \frac{m+\gamma_0}{\gamma_0}\right)^k \int_0^{b_0^2/2} e^{-y} {}_1F_1(k+m;\ 1;\ y) dy. \qquad \text{(A.6)}$$

Finally, using an integral property of the confluent hypergeometric function [30, Eqn. 3.2.5]:

$$\int e^{-z} z^{b-1} {}_1F_1(a;\ b;\ z) dz = \frac{e^{-z} z^b}{b} {}_1F_1(1+a;\ 1+b;\ z),$$

we arrive at (3.32).

Appendix B

Special Case of $m = 1$

It is shown here that for $m = 1$, (3.32) reduces to the P_D expression for the Rayleigh fading case as given by (3.18). By letting $m = 1$ and $k = n - 1$, we can rewrite (3.32) as

$$P_D = \exp\left[-\frac{b_0^2}{2}\right]\sum_{n=1}^{\infty}(-1)^{n-1}\left(\frac{1}{\gamma_0}\right)^n\left(\frac{b_0^2}{2}\right)_1F_1\left(n+1;\ 2;\ \frac{b_0^2}{2}\right). \tag{B.1}$$

We then employ a recurrence relation for ${}_1F_1(a;\ b;\ z)$ [30, Eqn. 2.2.4]:

$$b\,{}_1F_1(a;\ b;\ z) - b\,{}_1F_1(a-1;\ b;\ z) - z\,{}_1F_1(a;\ b+1;\ z) = 0$$

to obtain

$$P_D = \exp\left[-\frac{b_0^2}{2}\right]\left[\sum_{n=1}^{\infty}\left(-\frac{1}{\gamma_0}\right)^n{}_1F_1\left(n;\ 1;\ \frac{b_0^2}{2}\right) - \sum_{n=1}^{\infty}\left(-\frac{1}{\gamma_0}\right)^n{}_1F_1\left(n+1;\ 1;\ \frac{b_0^2}{2}\right)\right]. \tag{B.2}$$

Using the multiplication theorem for ${}_1F_1(a;\ b;\ z)$ given by (A.5), and the fact that

$${}_1F_1(a;\ a;\ z) = e^z,$$

the second summation in the bracket of (B.2) can be written as

$$\sum_{n=1}^{\infty}\left(-\frac{1}{\gamma_0}\right)^n{}_1F_1\left(n+1;\ 1;\ \frac{b_0^2}{2}\right) = \left(\frac{\gamma_0}{1+\gamma_0}\right)\exp\left[\frac{b_0^2\gamma_0}{2(1+\gamma_0)}\right] - \exp\left[\frac{b_0^2}{2}\right]. \tag{B.3}$$

Letting $n = k + 1$ and exploiting the multiplication theorem given by (A.5) again, the first summation in (B.2) becomes

$$\sum_{n=1}^{\infty}\left(-\frac{1}{\gamma_0}\right)^n {}_1F_1\left(n;\ 1;\ \frac{b_0^2}{2}\right)=\left(-\frac{1}{1+\gamma_0}\right)\exp\left[\frac{b_0^2\gamma_0}{2(1+\gamma_0)}\right]. \tag{B.4}$$

Then, substituting (B.3) and (B.4) into (B.2), we obtain (3.18).

Appendix C

Distributions of $\beta_{kj}\cos\phi_{kj}$ and $\beta_{kj}\sin\phi_{kj}$

In this appendix, it is shown that if β_{kj} and ϕ_{kj} are two independent random variables having a Rayleigh and a uniform distribution over $[0,\ 2\pi)$, respectively, then $\beta_{kj}\cos\phi_{kj}$ and $\beta_{kj}\sin\phi_{kj}$ are Gaussian distributed.

The PDF of β_{kj} is given by (4.4), and the PDF of ϕ_{kj} is

$$p(\phi_{kj}) = \frac{1}{2\pi}. \tag{C.1}$$

Combining (4.4) with (C.1), we obtain

$$p_{\beta_{kj}\phi_{kj}}(\beta_{kj},\ \phi_{kj}) = \frac{\beta_{kj}}{\pi\beta_{kj}^2}\exp\left[-\frac{\beta_{kj}^2}{\beta_{kj}^2}\right]. \tag{C.2}$$

Let $x = \beta_{kj}\cos\phi_{kj}$ and $y = \beta_{kj}\sin\phi_{kj}$. Then, it follows that

$$\beta_{kj}(x,\ y) = \sqrt{x^2 + y^2} \quad \text{and} \quad \phi_{kj}(x,\ y) = \arctan y/x$$

Using the relationship [9, Eqn. 2.4-6]:

$$p_{xy}(x,\ y) = p_{\beta_{kj}\phi_{kj}}\left[\beta_{kj}(x,\ y),\ \phi_{kj}(x,\ y)\right]\left|\frac{\partial(\beta_{kj},\ \phi_{kj})}{\partial(x,\ y)}\right|, \tag{C.3}$$

where

$$\frac{\partial(\beta_{kj},\,\phi_{kj})}{\partial(x,\,y)}=\begin{vmatrix}\dfrac{\partial\beta_{kj}}{\partial x} & \dfrac{\partial\beta_{kj}}{\partial y}\\ \dfrac{\partial\phi_{kj}}{\partial x} & \dfrac{\partial\phi_{kj}}{\partial y}\end{vmatrix},$$

we obtain

$$p_{xy}(x,\,y)=\frac{1}{2\pi\sigma^2}\exp\left[-\frac{x^2+y^2}{2\sigma^2}\right], \tag{C.4}$$

where $\sigma^2=\overline{\beta_{kj}^2}/2$. This is a product of a function of x times a function of y, thus the random variables $x=\beta_{kj}\cos\phi_{kj}$ and $y=\beta_{kj}\sin\phi_{kj}$ are independent and Gaussian distributed with density functions

$$p_x(x)=\frac{1}{\sigma\sqrt{2\pi}}\exp\left[-\frac{x^2}{2\sigma^2}\right] \quad\text{and}\quad p_y(y)=\frac{1}{\sigma\sqrt{2\pi}}\exp\left[-\frac{y^2}{2\sigma^2}\right].$$

Appendix D

Derivation of Equation (4.34)

In this appendix, the derivation of (4.34) is conducted. Since $\{\beta_{kj}\}$ are independent of $\{\phi_{kj}\}$, the first expectation in (4.33) can be expressed as

$$E\left\{\sum_{j=0}^{\infty}\sum_{k=0}^{\infty}\left(T_h - T_j - \tau_{kj}\right)^2 \beta_{kj}^2 \cos^2\phi_{kj}\right\} = \sum_{j=0}^{\infty}\sum_{k=0}^{\infty} E\left\{\left(T_h - T_j - \tau_{kj}\right)^2 \beta_{kj}^2\right\} E\left\{\cos^2\phi_{kj}\right\}$$

$$= \sum_{j=0}^{\infty}\sum_{k=0}^{\infty}\frac{1}{2} E\left\{\left(T_h - T_j - \tau_{kj}\right)^2 \beta_{kj}^2\right\}. \qquad \text{(D.1)}$$

To simplify the derivation, let us first assume that there is only one cluster, i.e. the zeroth cluster. Hence, (D.1) may be written as

$$\sum_{k=0}^{\infty}\frac{1}{2} E\left\{\left(T_h - \tau_{k0}\right)^2 \beta_{k0}^2\right\} = \frac{1}{2}\left[E\left\{T_h^2\beta_{00}^2\right\} + E\left\{\left(T_h - \tau_{10}\right)^2\beta_{10}^2\right\} + E\left\{\left(T_h - \tau_{20}\right)^2\beta_{20}^2\right\} + \cdots\right]$$

$$= \frac{1}{2}\left[T_h^2\int_0^{\infty}\beta_{00}^2 p(\beta_{00})d\beta_{00} + \int_0^{T_h}\left(T_h - \tau_{10}\right)^2\int_0^{\infty}\beta_{10}^2 p\left(\beta_{10}\middle|\tau_{10}\right)d\beta_{10}p(\tau_{10})d\tau_{10}\right.$$

$$\left. + \int_0^{T_h}\int_{\tau_{10}}^{T_h}\left(T_h - \tau_{20}\right)^2\int_0^{\infty}\beta_{20}^2 p\left(\beta_{20}\middle|\tau_{20}\right)d\beta_{20}p\left(\tau_{20}\middle|\tau_{10}\right)p(\tau_{10})d\tau_{20}d\tau_{10} + \cdots\right], \qquad \text{(D.2)}$$

where the convention that $T_0 = 0$ has been invoked. The density functions $p\left(\tau_{kj}\middle|\tau_{(k-1)j}\right)$

and $p\left(\beta_{kj}\middle|\tau_{kj}\right)$ are given by (4.3) and (4.4), respectively. Moreover, it can easily be shown that

$$\int_0^\infty \beta_{kj}^2 p\left(\beta_{kj}\middle|\tau_{kj}\right)d\beta_{kj} = \overline{\beta_{kj}^2}, \tag{D.3}$$

where $\overline{\beta_{kj}^2}$ is described by (4.5). Substituting (4.3)-(4.5) into (D.2), we obtain

$$\sum_{k=0}^{\infty}\frac{1}{2}E\left\{\left(T_h-\tau_{k0}\right)^2\beta_{k0}^2\right\} = \frac{1}{2}\overline{\beta_{00}^2}\left\{T_h^2+\lambda\int_0^{T_h}\left(T_h-\tau_{10}\right)^2\exp\left[-\tau_{10}\left(\lambda+\frac{1}{\eta}\right)\right]d\tau_{10}\right.$$
$$\left.+\lambda^2\int_0^{T_h}\int_{\tau_{10}}^{T_h}\left(T_h-\tau_{20}\right)^2\exp\left[-\tau_{20}\left(\lambda+\frac{1}{\eta}\right)\right]d\tau_{20}d\tau_{10}+\cdots\right\} \tag{D.4a}$$

$$= \frac{1}{2}\overline{\beta_{00}^2}\left\{T_h^2\underbrace{\left[1+\lambda\int_0^{T_h}e^{-\tau_{10}\left(\lambda+1/\eta\right)}d\tau_{10}+\lambda^2\int_0^{T_h}\int_{\tau_{10}}^{T_h}e^{-\tau_{20}\left(\lambda+1/\eta\right)}d\tau_{20}d\tau_{10}+\cdots\right]}_{A}\right.$$
$$-2T_h\underbrace{\left[\lambda\int_0^{T_h}\tau_{10}e^{-\tau_{10}\left(\lambda+1/\eta\right)}d\tau_{10}+\lambda^2\int_0^{T_h}\int_{\tau_{10}}^{T_h}\tau_{20}e^{-\tau_{20}\left(\lambda+1/\eta\right)}d\tau_{20}d\tau_{10}+\cdots\right]}_{B}$$
$$\left.+\underbrace{\left[\lambda\int_0^{T_h}\tau_{10}^2e^{-\tau_{10}\left(\lambda+1/\eta\right)}d\tau_{10}+\lambda^2\int_0^{T_h}\int_{\tau_{10}}^{T_h}\tau_{20}^2e^{-\tau_{20}\left(\lambda+1/\eta\right)}d\tau_{20}d\tau_{10}+\cdots\right]}_{C}\right\}. \tag{D.4b}$$

As mentioned earlier, each channel parameter is assumed to be within a certain range where the delay spread is no larger than one hop period. This implies that the subsequent rays (and clusters) will dissipate as τ_{kj} (and T_j) approaches T_h. Therefore, the integrals with respect to τ_{kj} in (D.4b) will produce zeros when evaluated at the upper limits. Following this discussion, A in (D.4b) can be evaluated to give

$$A = 1 + \frac{\eta\lambda}{\eta\lambda + 1} + \left(\frac{\eta\lambda}{\eta\lambda + 1}\right)^2 + \left(\frac{\eta\lambda}{\eta\lambda + 1}\right)^3 + \cdots. \tag{D.5}$$

Using one of the definitions of the binomial series expansion available from [67, p. 295], we finally obtain

$$A = 1 + \eta\lambda. \tag{D.6}$$

Under the same assumption, B in (D.4b) can be evaluated to produce

$$\begin{aligned} B &= \frac{\lambda}{\left(\lambda + 1/\eta\right)^2} + \frac{2\lambda^2}{\left(\lambda + 1/\eta\right)^3} + \frac{3\lambda^3}{\left(\lambda + 1/\eta\right)^4} + \cdots \\ &= \frac{\lambda}{\left(\lambda + 1/\eta\right)^2}\left[1 + 2\left(\frac{\eta\lambda}{\eta\lambda + 1}\right) + 3\left(\frac{\eta\lambda}{\eta\lambda + 1}\right)^2 + \cdots\right]. \end{aligned} \tag{D.7}$$

Again, exploiting a definition of the binomial series expansion given in [67], we have

$$B = \eta^2\lambda. \tag{D.8}$$

Finally, C in (D.4b) may be expressed as

$$\begin{aligned} C &= \lambda\frac{2}{\left(\lambda + 1/\eta\right)^3} + \lambda^2\int_0^{T_h}\left[\frac{\tau_{10}^2}{\left(\lambda + 1/\eta\right)} + \frac{2\tau_{10}}{\left(\lambda + 1/\eta\right)^2} + \frac{2}{\left(\lambda + 1/\eta\right)^3}\right]e^{-\tau_{10}\left(\lambda + 1/\eta\right)}d\tau_{10} \\ &\quad + \lambda^3\int_0^{T_h}\int_{\tau_{10}}^{T_h}\left[\frac{\tau_{20}^2}{\left(\lambda + 1/\eta\right)} + \frac{2\tau_{20}}{\left(\lambda + 1/\eta\right)^2} + \frac{2}{\left(\lambda + 1/\eta\right)^3}\right]e^{-\tau_{20}\left(\lambda + 1/\eta\right)}d\tau_{20}d\tau_{10} + \cdots \\ &= \lambda\frac{2}{\left(\lambda + 1/\eta\right)^3} + \lambda^2\frac{6}{\left(\lambda + 1/\eta\right)^4} + \lambda^3\frac{12}{\left(\lambda + 1/\eta\right)^5} + \cdots \end{aligned}$$

$$= \frac{2\lambda}{\left(\lambda + 1/\eta\right)^3}\left[1 + 3\left(\frac{\eta\lambda}{\eta\lambda+1}\right) + \frac{3(3+1)}{2!}\left(\frac{\eta\lambda}{\eta\lambda+1}\right)^2 + \cdots\right]. \tag{D.9}$$

Utilizing another definition of the binomial series expansion in [67], we obtain

$$C = 2\eta^3\lambda. \tag{D.10}$$

Substituting (D.6), (D.8) and (D.10) into (D.4b) results in

$$\sum_{k=0}^{\infty}\frac{1}{2}E\left\{\left(T_h - \tau_{k0}\right)^2\beta_{k0}^2\right\} = \frac{1}{2}\overline{\beta_{00}^2}\left[T_h^2(1+\eta\lambda) - 2T_h\eta^2\lambda + 2\eta^3\lambda\right]. \tag{D.11}$$

Now, let us go back to (D.1) where we have accounted for more than one clusters. We expand the summation on its right hand side to produce

$$E\left\{\sum_{j=0}^{\infty}\sum_{k=0}^{\infty}\left(T_h - T_j - \tau_{kj}\right)^2\beta_{kj}^2\cos^2\phi_{kj}\right\}$$

$$= \frac{1}{2}\left\{\left[E\left\{T_h^2\beta_{00}^2\right\} + E\left\{\left(T_h - \tau_{10}\right)^2\beta_{10}^2\right\} + E\left\{\left(T_h - \tau_{20}\right)^2\beta_{20}^2\right\} + \cdots\right]\right.$$

$$+\left[E\left\{\left(T_h - T_1\right)^2\beta_{01}^2\right\} + E\left\{\left(T_h - T_1 - \tau_{11}\right)^2\beta_{11}^2\right\} + E\left\{\left(T_h - T_1 - \tau_{21}\right)^2\beta_{21}^2\right\} + \cdots\right]$$

$$\left.+\left[E\left\{\left(T_h - T_2\right)^2\beta_{02}^2\right\} + E\left\{\left(T_h - T_2 - \tau_{12}\right)^2\beta_{12}^2\right\} + E\left\{\left(T_h - T_2 - \tau_{22}\right)^2\beta_{22}^2\right\} + \cdots\right] + \cdots\right\}$$

$$= \frac{1}{2}\left\{\left[T_h^2\int_0^{\infty}\beta_{00}^2 p(\beta_{00})d\beta_{00} + \int_0^{T_h}\left(T_h - \tau_{10}\right)^2\int_0^{\infty}\beta_{10}^2 p\left(\beta_{10}|\tau_{10}\right)d\beta_{10}p(\tau_{10})d\tau_{10}\right.\right.$$

$$\left.+\int_0^{T_h}\int_{\tau_{10}}^{T_h}\left(T_h - \tau_{20}\right)^2\int_0^{\infty}\beta_{20}^2 p\left(\beta_{20}|\tau_{20}\right)d\beta_{20}p\left(\tau_{20}|\tau_{10}\right)p(\tau_{10})d\tau_{20}d\tau_{10} + \cdots\right]$$

$$+\left[\int_0^{T_h}\left(T_h - T_1\right)^2\int_0^{\infty}\beta_{01}^2 p\left(\beta_{01}|T_1\right)d\beta_{01}p(T_1)dT_1\right.$$

$$\left.+\int_0^{T_h}\int_0^{T_h}\left(T_h - T_1 - \tau_{11}\right)^2\int_0^{\infty}\beta_{11}^2 p\left(\beta_{11}|T_1,\ \tau_{11}\right)d\beta_{11}p(\tau_{11})p(T_1)d\tau_{11}dT_1\right.$$

$$+\int_0^{T_h}\int_0^{T_h}\int_{\tau_{11}}^{T_h}\left(T_h-T_1-\tau_{21}\right)^2\int_0^{\infty}\beta_{21}^2 p\left(\beta_{21}|T_1,\ \tau_{21}\right)d\beta_{21}$$

$$\cdot p\left(\tau_{21}|\tau_{11}\right)p\left(\tau_{11}\right)p\left(T_1\right)d\tau_{21}d\tau_{11}dT_1+\cdots\Big]$$

$$+\Bigg[\int_0^{T_h}\int_{T_1}^{T_h}\left(T_h-T_2\right)^2\int_0^{\infty}\beta_{02}^2 p\left(\beta_{02}|T_2\right)d\beta_{02}p\left(T_2|T_1\right)p\left(T_1\right)dT_2dT_1$$

$$+\int_0^{T_h}\int_{T_1}^{T_h}\int_0^{T_h}\left(T_h-T_2-\tau_{12}\right)^2\int_0^{\infty}\beta_{12}^2 p\left(\beta_{12}|T_2,\ \tau_{12}\right)d\beta_{12}p\left(\tau_{12}\right)p\left(T_2|T_1\right)p\left(T_1\right)d\tau_{12}dT_2dT_1$$

$$+\int_0^{T_h}\int_{T_1}^{T_h}\int_0^{T_h}\int_{\tau_{12}}^{T_h}\left(T_h-T_2-\tau_{22}\right)^2\int_0^{\infty}\beta_{22}^2 p\left(\beta_{22}|T_2,\ \tau_{22}\right)d\beta_{22}$$

$$\cdot p\left(\tau_{22}|\tau_{12}\right)p\left(\tau_{12}\right)p\left(T_2|T_1\right)p\left(T_1\right)d\tau_{22}d\tau_{12}dT_2dT_1+\cdots\Big]+\cdots\Bigg\}. \tag{D.12}$$

Then, we substitute (4.2)-(4.5) into (D.12) to obtain

$$E\left\{\sum_{j=0}^{\infty}\sum_{k=0}^{\infty}\left(T_h-T_j-\tau_{kj}\right)^2\beta_{kj}^2\cos^2\phi_{kj}\right\}=\frac{1}{2}\overline{\beta_{00}^2}\Bigg\{\Bigg[T_h^2+\lambda\int_0^{T_h}\left(T_h-\tau_{10}\right)^2 e^{-\tau_{10}\left(\lambda+1/\eta\right)}d\tau_{10}$$

$$+\lambda^2\int_0^{T_h}\int_{\tau_{10}}^{T_h}\left(T_h-\tau_{20}\right)^2 e^{-\tau_{20}\left(\lambda+1/\eta\right)}d\tau_{20}d\tau_{10}+\cdots\Bigg]$$

$$+\Bigg[\Lambda\int_0^{T_h}\left(T_h-T_1\right)^2 e^{-T_1\left(\Lambda+1/\Gamma\right)}dT_1+\Lambda\lambda\int_0^{T_h}\int_0^{T_h}\left(T_h-T_1-\tau_{11}\right)^2 e^{-T_1\left(\Lambda+1/\Gamma\right)}e^{-\tau_{11}\left(\lambda+1/\eta\right)}d\tau_{11}dT_1$$

$$+\Lambda\lambda^2\int_0^{T_h}\int_0^{T_h}\int_{\tau_{11}}^{T_h}\left(T_h-T_1-\tau_{21}\right)^2 e^{-T_1\left(\Lambda+1/\Gamma\right)}e^{-\tau_{21}\left(\lambda+1/\eta\right)}d\tau_{21}d\tau_{11}dT_1+\cdots\Bigg]$$

$$+\Bigg[\Lambda^2\int_0^{T_h}\int_{T_1}^{T_h}\left(T_h-T_2\right)^2 e^{-T_2\left(\Lambda+1/\Gamma\right)}dT_2dT_1+\Lambda^2\lambda\int_0^{T_h}\int_{T_1}^{T_h}\int_0^{T_h}\left(T_h-T_2-\tau_{12}\right)^2 e^{-T_2\left(\Lambda+1/\Gamma\right)}$$

$$\cdot e^{-\tau_{12}\left(\lambda+1/\eta\right)}d\tau_{12}dT_2dT_1+\Lambda^2\lambda^2\int_0^{T_h}\int_{T_1}^{T_h}\int_0^{T_h}\int_{\tau_{12}}^{T_h}\left(T_h-T_2-\tau_{22}\right)^2 e^{-T_2\left(\Lambda+1/\Gamma\right)}$$

$$\cdot e^{-\tau_{22}\left(\lambda+1/\eta\right)} d\tau_{22} d\tau_{12} dT_2 dT_1 + \cdots \Big] + \cdots \Big\} \tag{D.13a}$$

$$= \frac{1}{2}\overline{\beta_{00}^2} \Big\{ \Big[T_h^2 + \lambda \int_0^{T_h} (T_h - \tau_{10})^2 e^{-\tau_{10}\left(\lambda+1/\eta\right)} d\tau_{10} + \lambda^2 \int_0^{T_h} \int_{\tau_{10}}^{T_h} (T_h - \tau_{20})^2 \cdot e^{-\tau_{20}\left(\lambda+1/\eta\right)} d\tau_{20} d\tau_{10} + \cdots \Big]$$

$$+ \Big[\Lambda \int_0^{T_h} e^{-T_1(\Lambda+1/\Gamma)} \Big((T_h - T_1)^2 + \lambda \int_0^{T_h} (T_h - T_1 - \tau_{11})^2 e^{-\tau_{11}\left(\lambda+1/\eta\right)} d\tau_{11} + \lambda^2 \int_0^{T_h} \int_{\tau_{11}}^{T_h} (T_h - T_1 - \tau_{21})^2 e^{-\tau_{21}\left(\lambda+1/\eta\right)} d\tau_{21} d\tau_{11} + \cdots \Big) dT_1 \Big]$$

$$+ \Big[\Lambda^2 \int_0^{T_h} \int_{T_1}^{T_h} e^{-T_2(\Lambda+1/\Gamma)} \Big((T_h - T_2)^2 + \lambda \int_0^{T_h} (T_h - T_2 - \tau_{12})^2 e^{-\tau_{12}\left(\lambda+1/\eta\right)} d\tau_{12} + \lambda^2 \int_0^{T_h} \int_{\tau_{12}}^{T_h} (T_h - T_2 - \tau_{22})^2 e^{-\tau_{22}\left(\lambda+1/\eta\right)} d\tau_{22} d\tau_{12} + \cdots \Big) dT_2 dT_1 \Big] + \cdots \Big\}. \tag{D.13b}$$

The series in the first bracket of (D.13b) is identical to that on the right hand side of (D.4a). Thus, from (D.11), the series can be expressed as

$$S_1 = T_h^2(1 + \eta\lambda) - 2T_h\eta^2\lambda + 2\eta^3\lambda. \tag{D.14}$$

The series in the second and the third brackets of (D.13b) are written in the same format as the series in (D.4a), and hence can be easily evaluated to give

$$S_2 = (T_h - T_1)^2(1 + \eta\lambda) - 2(T_h - T_1)\eta^2\lambda + 2\eta^3\lambda, \tag{D.15}$$

and

$$S_3 = (T_h - T_2)^2(1+\eta\lambda) - 2(T_h - T_2)\eta^2\lambda + 2\eta^3\lambda, \tag{D.16}$$

respectively. Substituting (D.14)-(D.16) into (D.13b), we obtain

$$E\left\{\sum_{j=0}^{\infty}\sum_{k=0}^{\infty}(T_h - T_j - \tau_{kj})^2\beta_{kj}^2\cos^2\phi_{kj}\right\} = \frac{1}{2}\overline{\beta_{00}^2}\Big\{(1+\eta\lambda)\Big[T_h^2 + \Lambda\int_0^{T_h}(T_h - T_1)^2 \cdot e^{-T_1(\Lambda+1/\Gamma)}dT_1 + \Lambda^2\int_0^{T_h}\int_{T_1}^{T_h}(T_h - T_2)^2 e^{-T_2(\Lambda+1/\Gamma)}dT_2dT_1 + \cdots\Big]$$
$$+ (2\eta^3\lambda - 2T_h\eta^2\lambda)\Big[1 + \Lambda\int_0^{T_h}e^{-T_1(\Lambda+1/\Gamma)}dT_1 + \Lambda^2\int_0^{T_h}\int_{T_1}^{T_h}e^{-T_2(\Lambda+1/\Gamma)}dT_2dT_1 + \cdots\Big]$$
$$+ 2\eta^2\lambda\Big[\Lambda\int_0^{T_h}T_1e^{-T_1(\Lambda+1/\Gamma)}dT_1 + \Lambda^2\int_0^{T_h}\int_{T_1}^{T_h}T_2e^{-T_2(\Lambda+1/\Gamma)}dT_2dT_1 + \cdots\Big]\Big\}. \tag{D.17}$$

Again, the series in the first bracket of (D.17) is expressed in the same format as the series in (D.4a), whereas the series in the second and the third brackets are similar to those in brackets *A* and *B* of (D.4b), respectively. Thus, using the results given by (D.6), (D.8), and (D.11), we arrive at (4.34).

Appendix E

Derivation of Equation (4.35)

To begin with, let us expand the second expectation in (4.33) as follows:

$$E\left\{\sum_{j=0}^{\infty}\sum_{k=0}^{\infty}\left(T_j+\tau_{kj}\right)^2\beta_{kj}^2\cos^2\phi_{kj}\right\}=\frac{1}{2}\left\{\left[E\left\{\tau_{10}^2\beta_{10}^2\right\}+E\left\{\tau_{20}^2\beta_{20}^2\right\}+\cdots\right]\right.$$

$$+\left[E\left\{T_1^2\beta_{01}^2\right\}+E\left\{\left(T_1+\tau_{11}\right)^2\beta_{11}^2\right\}+E\left\{\left(T_1+\tau_{21}\right)^2\beta_{21}^2\right\}+\cdots\right]$$

$$\left.+\left[E\left\{T_2^2\beta_{02}^2\right\}+E\left\{\left(T_2+\tau_{12}\right)^2\beta_{12}^2\right\}+E\left\{\left(T_2+\tau_{22}\right)^2\beta_{22}^2\right\}+\cdots\right]+\cdots\right\} \tag{E.1a}$$

$$=\frac{1}{2}\overline{\beta_{00}^2}\left\{\left[\lambda\int_0^{T_h}\tau_{10}^2e^{-\tau_{10}\left(\lambda+1/\eta\right)}d\tau_{10}+\lambda^2\int_0^{T_h}\int_{\tau_{10}}^{T_h}\tau_{20}^2e^{-\tau_{20}\left(\lambda+1/\eta\right)}d\tau_{20}d\tau_{10}+\cdots\right]\right.$$

$$+\left[\Lambda\int_0^{T_h}e^{-T_1\left(\Lambda+1/\Gamma\right)}\left(T_1^2+\lambda\int_0^{T_h}\left(T_1+\tau_{11}\right)^2e^{-\tau_{11}\left(\lambda+1/\eta\right)}d\tau_{11}\right.\right.$$

$$\left.\left.+\lambda^2\int_0^{T_h}\int_{\tau_{11}}^{T_h}\left(T_1+\tau_{21}\right)^2e^{-\tau_{21}\left(\lambda+1/\eta\right)}d\tau_{21}d\tau_{11}+\cdots\right)dT_1\right]$$

$$\left.+\left[\Lambda^2\int_0^{T_h}\int_{T_1}^{T_h}e^{-T_2\left(\Lambda+1/\Gamma\right)}\left(T_2^2+\lambda\int_0^{T_h}\left(T_2+\tau_{12}\right)^2e^{-\tau_{12}\left(\lambda+1/\eta\right)}d\tau_{12}\right.\right.\right.$$

$$+\lambda^2\int_0^{T_h}\int_{\tau_{12}}^{T_h}\left(T_2+\tau_{22}\right)^2 e^{-\tau_{22}\left(\lambda+1/\eta\right)}d\tau_{22}d\tau_{12}+\cdots\Big)dT_2dT_1\Big]+\cdots\Big\}. \tag{E.1b}$$

Notice that the series in the first bracket of (E.1b) is identical to that in bracket *C* of (D.4b), while the series in the second and the third brackets are both similar to that in (D.4a). Hence, using the results given by (D.10) and (D.11), we obtain

$$E\left\{\sum_{j=0}^{\infty}\sum_{k=0}^{\infty}\left(T_j+\tau_{kj}\right)^2\beta_{kj}^2\cos^2\phi_{kj}\right\}=\frac{1}{2}\overline{\beta_{00}^2}\Big\{\Big[2\eta^3\lambda\Big]+\Big[\Lambda\int_0^{T_h}e^{-T_1\left(\Lambda+1/\Gamma\right)}\left(T_1^2(1+\eta\lambda)\right.$$

$$\left.+2T_1\eta^2\lambda+2\eta^3\lambda\right)dT_1\Big]+\Big[\Lambda^2\int_0^{T_h}\int_{T_1}^{T_h}e^{-T_2\left(\Lambda+1/\Gamma\right)}$$

$$\cdot\left(T_2^2(1+\eta\lambda)+2T_1\eta^2\lambda+2\eta^3\lambda\right)dT_2dT_1\Big]+\cdots\Big\}. \tag{E.2}$$

The terms on the right hand side of (E.2) can be rearranged to give

$$E\left\{\sum_{j=0}^{\infty}\sum_{k=0}^{\infty}\left(T_j+\tau_{kj}\right)^2\beta_{kj}^2\cos^2\phi_{kj}\right\}=\frac{1}{2}\overline{\beta_{00}^2}\Big\{\Big[2\eta^3\lambda\Big]$$

$$+(1+\eta\lambda)\Big[\Lambda\int_0^{T_h}T_1^2e^{-T_1\left(\Lambda+1/\Gamma\right)}dT_1+\Lambda^2\int_0^{T_h}\int_{T_1}^{T_h}T_2^2e^{-T_2\left(\Lambda+1/\Gamma\right)}dT_2dT_1+\cdots\Big]$$

$$+2\eta^2\lambda\Big[\Lambda\int_0^{T_h}T_1e^{-T_1\left(\Lambda+1/\Gamma\right)}dT_1+\Lambda^2\int_0^{T_h}\int_{T_1}^{T_h}T_2e^{-T_2\left(\Lambda+1/\Gamma\right)}dT_2dT_1+\cdots\Big]$$

$$+2\eta^3\lambda\Big[\Lambda\int_0^{T_h}e^{-T_1\left(\Lambda+1/\Gamma\right)}dT_1+\Lambda^2\int_0^{T_h}\int_{T_1}^{T_h}e^{-T_2\left(\Lambda+1/\Gamma\right)}dT_2dT_1+\cdots\Big]\Big\}. \tag{E.3}$$

Again, notice that the series in (E.3) are similar to those contained in brackets *A*,

B, and C of (D.4b). Therefore, utilizing the results given in Appendix D, we finally obtain (4.35).

Appendix F

Derivation of Equation (4.36)

This appendix derives the expression for $\overline{\beta_{00}^2}$ as given by (4.36). The total variance S of a received signal can be expressed as

$$S = E\left\{\sum_{j=0}^{\infty}\sum_{k=0}^{\infty}\frac{1}{4}T_h^2\beta_{kj}^2\cos^2\phi_{kj}\right\}$$

$$= \frac{T_h^2}{8}\sum_{j=0}^{\infty}\sum_{k=0}^{\infty}E\left\{\beta_{kj}^2\right\}. \qquad \text{(F.1)}$$

Expanding the summation in (F.1) and utilizing (4.2)-(4.5), we have

$$S = \frac{1}{8}T_h^2\overline{\beta_{00}^2}\left\{\left[1+\lambda\int_0^{T_h}e^{-\tau_{10}\left(\lambda+1/\eta\right)}d\tau_{10}+\lambda^2\int_0^{T_h}\int_{\tau_{10}}^{T_h}e^{-\tau_{20}\left(\lambda+1/\eta\right)}d\tau_{20}d\tau_{10}+\cdots\right]\right.$$

$$+\left[\Lambda\int_0^{T_h}e^{-T_1\left(\Lambda+1/\Gamma\right)}dT_1+\Lambda\lambda\int_0^{T_h}\int_0^{T_h}e^{-T_1\left(\Lambda+1/\Gamma\right)}e^{-\tau_{11}\left(\lambda+1/\eta\right)}d\tau_{11}dT_1\right.$$

$$\left.\left.+\Lambda\lambda^2\int_0^{T_h}\int_0^{T_h}\int_{\tau_{11}}^{T_h}e^{-T_1\left(\Lambda+1/\Gamma\right)}e^{-\tau_{21}\left(\lambda+1/\eta\right)}d\tau_{21}d\tau_{11}dT_1+\cdots\right]\right.$$

$$\left.+\left[\Lambda^2\int_0^{T_h}\int_{T_1}^{T_h}e^{-T_2\left(\Lambda+1/\Gamma\right)}dT_2dT_1+\Lambda^2\lambda\int_0^{T_h}\int_{T_1}^{T_h}\int_0^{T_h}e^{-T_2\left(\Lambda+1/\Gamma\right)}e^{-\tau_{12}\left(\lambda+1/\eta\right)}d\tau_{12}dT_2dT_1\right.\right.$$

$$+\Lambda^2\lambda^2\int_0^{T_h}\int_{T_1}^{T_h}\int_0^{T_h}\int_{\tau_{12}}^{T_h} e^{-T_2\left(\Lambda+1/\Gamma\right)}e^{-\tau_{22}\left(\lambda+1/\eta\right)}d\tau_{22}d\tau_{12}dT_2dT_1+\cdots\Bigg]+\cdots\Bigg\}$$

(F.2a)

$$=\frac{1}{8}T_h^2\overline{\beta_{00}^2}\Bigg\{\Bigg[1+\lambda\int_0^{T_h}e^{-\tau_{10}\left(\lambda+1/\eta\right)}d\tau_{10}+\lambda^2\int_0^{T_h}\int_{\tau_{10}}^{T_h}e^{-\tau_{20}\left(\lambda+1/\eta\right)}d\tau_{20}d\tau_{10}+\cdots\Bigg]$$

$$+\Bigg[\Lambda\int_0^{T_h}e^{-T_1\left(\Lambda+1/\Gamma\right)}\Bigg(1+\lambda\int_0^{T_h}e^{-\tau_{11}\left(\lambda+1/\eta\right)}d\tau_{11}+\lambda^2\int_0^{T_h}\int_{\tau_{11}}^{T_h}e^{-\tau_{21}\left(\lambda+1/\eta\right)}$$

$$\cdot d\tau_{21}d\tau_{11}+\cdots\Bigg)dT_1\Bigg]$$

$$+\Bigg[\Lambda^2\int_0^{T_h}\int_{T_1}^{T_h}e^{-T_2\left(\Lambda+1/\Gamma\right)}\Bigg(1+\lambda\int_0^{T_h}e^{-\tau_{12}\left(\lambda+1/\eta\right)}d\tau_{12}+$$

$$+\lambda^2\int_0^{T_h}\int_{\tau_{12}}^{T_h}e^{-\tau_{22}\left(\lambda+1/\eta\right)}d\tau_{22}d\tau_{12}+\cdots\Bigg)dT_2dT_1\Bigg]+\cdots\Bigg\}.$$

(F.2b)

Notice that all the series in (F.2b) are expressed in the same format as the series in bracket *A* of (D.4b). Thus, utilizing (D.6), we can obtain

$$S=\frac{1}{8}T_h^2\overline{\beta_{00}^2}(1+\eta\lambda)(1+\Gamma\Lambda), \tag{F.3}$$

and consequently

$$\overline{\beta_{00}^2}=S\left[\frac{1}{8}T_h^2(1+\eta\lambda)(1+\Gamma\Lambda)\right]^{-1}. \tag{4.36}$$

Appendix G

List of Symbols

b	actual threshold level of detector
b_0	normalized threshold level of detector
C	total number of cells in the system
d_0	variance of lognormally distributed specular component of Rician fading signal
K	number of bits per message and number of bits per address code word
L	number of hops per message symbol
M	number of simultaneous users
m	Nakagami fading parameter
N	average noise power
N_h	number of hopping channels
P_B	probability of bit error
P_D	probability of deletion
P_e	probability of chip error
P_F	probability of false alarm
P_S	probability of symbol error
R	data bit rate
R_c	coded bit rate
R_s	symbol rate
r	code rate

S	variance of signal
T	signalling period
T_h	hop or chip interval
T_j	arrival time of the jth cluster
T_s	symbol period
u	amplitude of signal
v	envelope of signal
W	spread-spectrum bandwidth
w	number of ISI hits bearing same signal as reference user
X	message of user
x	number of ISI hits
Y	address sequence of user
y	number of symbol hits
Z	modulated message sequence of user
z	number of symbol hits bearing same signal as reference user
α	average power of multipath component
β_k	positive gain of kth path
β_{kj}	positive gain of kth path of jth cluster
Γ	cluster power-delay time constant
γ	signal-to-noise ratio
γ_0	average signal-to-noise ratio
η	ray power-delay time constant
θ_k	phase shift of kth path
θ_{kj}	phase shift of kth path of jth cluster
Λ	cluster arrival rate
λ	ray arrival rate
μ	mean value of lognormally distributed specular component of Rician fading signal

ρ	Rician factor
τ	code word duration
τ_k	propagation delay of the kth path
τ_{kj}	arrival time of the kth ray of the jth cluster
φ	phase angle introduced by frequency synthesizer
Ω	mean-square value of amplitude of Nakagami fading signal

Appendix H

List of Acronyms

AWGN	additive white Gaussian noise
BFSK	binary frequency shift keying
FEC	forward error correction
FH-SS	frequency-hopped spread-spectrum
FH-SSMA	frequency-hopped spread-spectrum multiple access
FSK	frequency shift keying
ISI	intersymbol interference
LOS	line of sight
PDF	probability density function
SNR	signal-to-noise ratio